

LIBRARY
Michigan State
University

This is to certify that the

dissertation entitled

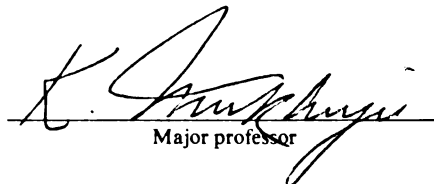
**PHASE TRANSITIONS IN HIGH TEMPERATURE ORDERED
INTERMETALLIC TITANIUM ALUMINUM ALLOYS**

presented by

Subhasish Sircar

has been accepted towards fulfillment
of the requirements for

Ph.D. degree in Materials Science


Major professor

Date May 23, 1987



RETURNING MATERIALS:

Place in book drop to
remove this checkout from
your record. FINES will
be charged if book is
returned after the date
stamped below.

--	--	--

**PHASE TRANSITIONS IN HIGH TEMPERATURE ORDERED
INTERMETALLIC TITANIUM ALUMINUM ALLOYS**

By

Subhasish Sircar

A DISSERTATION

Submitted to
Michigan State University
in partial fulfillment of the requirements
for the degree of

DOCTOR OF PHILOSOPHY

Department of Metallurgy, Mechanics and Materials Science

1987

This is to certify that the
dissertation entitled

**PHASE TRANSITIONS IN HIGH TEMPERATURE ORDERED
INTERMETALLIC TITANIUM ALUMINUM ALLOYS**

presented by

Subhasish Sircar

Subhasish Sircar

Subhasish Sircar
Doctor of Philosophy Candidate

5/20/87.
Date

has been accepted towards fulfillment
of the requirements for

Doctor of Philosophy Degree in Metallurgy,
Mechanics and Materials Science

Michigan State University

by

K. Mukherjee

K. Mukherjee
Professor and Chairman
Dissertation Advisor
Department of Metallurgy,
Mechanics and Materials Science

5/20/87
Date

S. D. Mahanti

S. D. Mahanti
Professor
Department of Physics and Astronomy

5/20/87
Date

Gay Lee Cloud

G. L. Cloud
Professor
Department of Metallurgy,
Mechanics and Materials Science

20 May 1987
Date

C. M. Hwang

C. M. Hwang
Assistant Professor
Department of Metallurgy,
Mechanics and Materials Science

5/20/87
Date

DEDICATED TO MY DAUGHTER, SURAVI

ACKNOWLEDGEMENTS

First and foremost, I would like to express my deep sense of gratitude to my advisor, Professor K. Mukherjee for his constant guidance and encouragement during the course of this research. I would also like to thank Professor S. D. Mahanti for taking time out whenever I needed it, to provide his patient guidance and beneficial discussions in making this project a success. I am also grateful to my parents and family for their boundless love and full support. The considerateness, understanding and encouragement coming from my wife, Hena, made everything go smoothly.

I would also like to thank my friends and colleagues for their help and support throughout my entire stay at Michigan State University.

Last, but not the least, I would like to take this opportunity and thank Leo Szafranski, our laboratory technician, for his help, and the U.S. Office of Naval Research for providing partial support for this research.

ABSTRACT

PHASE TRANSITIONS IN HIGH TEMPERATURE ORDERED INTERMETALLIC TITANIUM ALUMINUM ALLOYS

by

Subhasish Sircar

This study is aimed at understanding the Ti-rich end of the Ti-Al phase diagram and also to determine the nature of the order disorder transformation in this system. Investigations on the Ti-Al binary phase diagram are full of controversy, specifically about the $\alpha/\alpha + \alpha_2$ phase boundary and the existence of the α_2 phase. These discrepancies may be caused by the difference in the oxygen content and/or by the difficulty in the confirmation of the existence of a small amount of α_2 phase. Calorimetric experiments were performed at different heating rates, on Ti-Al Alloys containing various percentages of aluminum. A modified Ti-Al phase diagram (Ti-rich end) is proposed. X-ray diffraction and electron microscopy have also been performed on some alloys to investigate the nature of the phase transitions in these alloys and more specifically the order-disorder transition: α (disordered h.c.p) $\rightarrow \alpha_2$ (ordered h.c.p., DO₁₉). A theoretical approach, using the Bragg William mean field theory has also been attempted in order to understand the nature of this order-disorder transformation.

TABLE OF CONTENTS

<u>Chapter</u>		<u>Page#</u>
	LIST OF FIGURES	vii
	LIST OF TABLES	x
1.	INTRODUCTION	1
2.	LITERATURE SURVEY	3
2.1	Ti-Al Phase Diagram	3
2.1.1	Differential Thermal Analysis of Ti Alloys	10
2.2	Order-Disorder Transformations	14
2.3	Common Types of Superlattices	19
2.3.1	The $L1_2$ Superlattice	22
2.3.2	The B2 Superlattice	24
2.3.3	The $L1_0$ Superlattice	24
2.3.4	The DO_3 Superlattice	26
2.3.5	The DO_{19} Superlattice	26
2.4	Ordering Transformations	28
2.4.1	Ordered Domains	33
2.5	Ordered Alloys for High Temperature Applications	43
2.5.1	Characteristics of Ordered Alloys	44
2.5.2	Dislocations in Ordered Structures	45
2.6	Titanium Aluminides	48
2.6.1	Deformation Studies on Titanium Aluminides	48
2.7	The Quasi-Chemical Model of Solid Solutions	52
3.	EXPERIMENTAL PROCEDURES AND TECHNIQUES	56

3.1	Selection of Heat Treatment Conditions	56
3.2	Heat Treatment Procedure	56
3.3	Analysis of Heat Treated Samples	57
3.3.1	Differential Thermal Analysis	57
3.3.2	X-ray Diffractometry	60
3.3.3	Electron Microscopy	61
4.	RESULTS AND DISCUSSION	62
4.1	Scope of the Present Study	62
4.2	DTA Results	63
4.3	TEM Results	73
4.3.1	Structure Factor Determination for the DO ₁₉ Crystal Structure	73
4.3.2	Domain Growth Studies	80
4.4	Microhardness Response	94
4.5	Bragg-William Approximation of the Order-Disorder Transformation for DO ₁₉ Crystal Structure	96
5.	CONCLUSIONS	110
	REFERENCES	112

LIST OF FIGURES

Fig. #	Description	Page #
1.	DO ₁₉ crystal structure showing the atom positions.	5
2.	Phase diagram as proposed by Bumps and Kessler.	6
3.	Phase diagram as proposed by Ence and Margolin.	7
4.	Phase diagram of the Ti-rich end of the Ti-Al system as proposed by Crossley.	9
5.	Phase diagram of the Ti-rich end of the Ti-Al system as proposed by Blackburn.	11
6.	Dilatometry data for Ti-Al binary alloys on cooling from 1125°C as obtained by Crossley.	12
7.	$\alpha \rightarrow \alpha + \text{Ti}_3\text{Al}$ continuous cooling transformation temperature vs. aluminum content of binary Ti alloys from dilatometry data.	13
8.	DSC/DTA data obtained on aged Ti-15 at.%Al and as-received Ti-6211 alloy samples.	15
9.	The five common ordered lattices, (a)L2 ₀ , (b)L1 ₂ , (c)L1 ₀ , (d)DO ₃ and (e)DO ₁₉ .	17
10.	Part of the Cu-Au phase diagram showing the region where the Cu ₃ Au and CuAu superlattices are stable.	18
11.	Part of the Cu-Zn phase diagram showing the order disorder transformation ($\beta \rightarrow \beta'$).	21
12.	The superlattice of Cu ₃ Au.	23
13.	The superlattice of β -brass	23
14.	The tetragonal superlattice CuAu.	23
15.	The superlattice of the DO ₃ type structure.	25
16.	The variation of long range order parameter with temperature for (a) CuZn type and (b) Cu ₃ Au type transformations.(Schematic)	31

17.	The formation of of an antiphase boundary (APB) when out-of-phase ordered domains grow together.	34
18.	(a) A thin foil electron micrograph showing APB's in an ordered AlFe alloy. (b) A schematic representation of the atomic configurations comprising structure in (a).	38
19.	(a) A thin foil electron micrograph showing APB's in ordered Cu ₃ Au allo.(b) A schematic representation of atomic configurations comprising structure in (a).	39
20.	Histograms of APD sizes observed at different temperatures and times for Ti ₃ Al alloy.	42
21.	Log-log plot of average domain size vs. time of annealing at different temperatures.	42
22.	Heat treatment schedule for Ti-Al alloys.	58
23.	DTA data obtained from Ti-16Al (≈25 at.%Al) alloy sample quenched from 1200°C.	64
24.	Heating rate dependence of the order-disorder phenomenon in Ti-Al system.	65
25.	Series of DTA data obtained from as quenched (from 1200°C) samples starting from Ti-16Al(≈25 at.%Al) to Ti-6Al(≈10 at.%Al).	67
26.	Series of DTA data obtained from Ti-16Al(≈25 at.%Al) alloy samples which were either quenched or quenched and aged at various temperatures that are indicated in the diagram.	68
27.	Proposed phase diagram (Mukherjee and Sircar) of the titanium rich end of the Ti-Al system. The full circles indicate the experimentally obtained phase boundaries.	69
28.	X-ray diffraction pattern obtained from an ordered sample of Ti-16Al(≈25 at.%Al).	72
29.	Geometrical relationship between the real lattice vector and the reciprocal lattice vector for a DO ₁₉ type crystal structure.	77
30.	The reciprocal lattice plane of DO ₁₉ type crystal structure for l = 0.	78

31.	The reciprocal lattice plane of DO_{19} type crystal structure for $l = 1$.	79
32.	Dark field TEM micrographs of Ti-16Al(≈ 25 at.% Al) alloy sample quenched (from 1200°C) and aged at 700°C for varying lengths of time.	83
33.	(a) Dark field TEM micrograph and SAD of Ti-16Al (≈ 25 at.% Al) alloy sample quenched (from 1200°C) and aged at 700°C for 20 hrs.	85
34.	Dark field TEM micrograph of Ti-16Al(≈ 25 at.% Al) alloy sample quenched (from 1200°C) and aged at 800°C for varying lengths of time.	88
35.	(a) Bright field (b) SAD (c) dark field micrograph of Ti-16Al(≈ 25 at.% Al) sample quenched (from 1200°C) and aged for 40 hrs. at 800°C .	90
36.	Histograms showing the distribution of domain sizes for different aging treatments. (a) 600°C 1hr. (b) 700°C 1hr. (c) 800°C 20 hrs.	92
37.	Logarithmic plot of average domain size versus aging time in mins. for Ti-16Al(≈ 25 at.% Al) at different temperatures indicated.	93
38.	Plot of Vicker's hardness number as a function of aging time in hours for Ti-16Al(≈ 25 at.% Al) at the different temperatures indicated.	95
39.	Three unit cells of the DO_{19} crystal structure.	97
40.	Plot of ordering parameter W versus $(KT)/ V^* $ for the DO_{19} type crystal structures.	102
41.	Plot of ordering parameter W versus $(KT)/ V^* $ for the B2 type crystal structures.	103
42.	Free energy as a function of W with increasing $(KT)/ V^* $ values for the DO_{19} type crystal structures.	104
43.	Free energy as a function of W with increasing $(KT)/ V^* $ values for the DO_{19} type crystal structures.	105
44.	Plot of W as a function of (T/T_c) for both DO_{19} and B2 type crystal structures.	108

LIST OF TABLES

Table #	Description	Page #
I.	Strukterbericht-Structure Reports for symbols of crystal structure types .	20
II	Common superlattice structures.	27
III	Dislocation configurations in various ordered alloys.	47
IV.	Properties of high temperature alloys.	49
V.	Structure factor data for DO_{19} type of crystal structure.	76

CHAPTER 1

INTRODUCTION

The nature of the phase diagram of the titanium rich Ti-Al system has long been a subject of considerable controversy. In Ti-Al alloys, which exhibit an increase in solid solubility with increasing temperature, it is possible to produce a super-saturated solid solution α . This α will subsequently undergo decomposition during aging. Several eutectoid alloys exhibit extensive solid solubility and remain as metastable α from which an intermetallic compound precipitates on aging below the eutectoid temperature. There is a general agreement that in the Ti-Al system, a phase exists at or near the Ti_3Al composition range with an ordered DO_{19} (α_2 , ordered h.c.p.) crystal structure.

Questions related to the Ti-Al phase diagram which are yet to be answered are: Where are the locations of the $\alpha/\alpha+\alpha_2$ and the $\alpha+\alpha_2/\alpha_2$ phase boundaries? Are there phases other than Ti_3Al (α_2) present at the titanium-rich end of the Ti-Al system and what is the extent of α_2 phase field? X-ray diffraction, optical and electron microscopy and differential thermal analysis have been performed in order to establish the phase equilibria of the titanium-rich end of the Ti-Al binary system and also to better understand the order-disorder transformation in this system. Calorimetric studies conducted on titanium-rich Ti-Al binary

alloys at various heating rates have helped establish the $\alpha \rightarrow \beta$ (α is the low temperature disordered h.c.p. phase and β is the b.c.c. high temperature phase), the α/α_2 and the $\alpha+\alpha_2/\alpha_2$ phase boundaries. A phase diagram for the titanium-rich end of the Ti-Al system has been proposed and compared with the existing phase diagrams.

It has also been shown that in the composition range of ≈ 10 at.% Al to ≈ 25 at.% Al, a metastable disordered α phase can be quenched in. This metastable phase then transforms to the ordered α_2 (DO_{19}) phase upon heating and/or isothermal aging. The kinetics of this ordering process is found to be composition-dependent, and is more sluggish for higher Al content alloys. Some electron microscopic work has been performed to understand the kinetics of this ordering process in detail. Ordered domain growth rate as a function of time and temperature is also being studied to the kinetics of this domain growth. This ordering transformation and domain growth have a profound effect on the mechanical properties of the alloys. A theoretical calculation using the Bragg-William mean field theory for the nearest neighbor atoms has been attempted so as to understand the nature of this ordering reaction. The results obtained indicate that the order \rightarrow disorder transition is of the first order type.

CHAPTER 2

LITERATURE SURVEY

2.1 Ti-Al PHASE DIAGRAM

The titanium-rich end of the titanium-aluminum (Ti-Al) system has long been a subject of considerable controversy. The earliest investigation of the Ti-Al system was by Ogden et. al. [Ref.1] and Bumps et. al. [Ref.2] in the late 40's. They both reported wide solubility of the aluminum in the primary solid solution α (hcp). Aluminum was reported soluble in the low temperature allotroph (α) to the extent of 37 at.% (25 wt.%), and the first intermediate phase was reportedly TiAl. Somewhat later, Kornilov et. al [Ref. 3] reported a similar diagram which had the phase boundaries displaced towards lower aluminum contents and also towards higher temperatures. Beginning about this time (1956) reports in the literature made it very clear that one or more intermediate phases occurred at lower aluminum contents than TiAl [Ref. 4-17].

Not only is there a controversy regarding the presence or absence of a certain phase, but also the extent of the existence of the phase (composition and temperature range) in the phase diagram is controversial.

Before 1966, reports and literature included five major investigations of the titanium-rich end of the Ti-Al diagram [Ref. 4,12,14,16,17]. Three of these diagrams showed two two-phase fields

below 37 at.% (25 wt.%) Al, while two of them showed a single two-phase field. The existence of the phase Ti_3Al was firmly established and was included in each of the diagrams, except those of Sato and Huang and Bumps, Kessler and Hansen [Ref. 12, 2]. Although, it was generally agreed that Ti_3Al is an ordered phase, there was a general disagreement regarding the cell dimension of the Ti_3Al (hereto referred to as the α_2 phase). The "a" parameter was supposed to be approximately one [Ref. 4,12,15], two [Ref. 6-10,13,14] or four [Ref. 14] times that for primary α . Beyond this, however, the diagrams were remarkable for their lack of agreement. It should be mentioned at this point that, although Ti_3Al was an established phase, a Ti_2Al phase was also reported by some authors [Ref. 5,6,9,10,14] in the titanium-rich end of the Ti-Al system within the 25 at.% Al range.

Crossley [Ref. 18] has reviewed the phase diagrams that have been advanced for the system and in his turn proposed yet another one. There seems to be a general agreement that a phase exists at a composition at or near Ti_3Al with an ordered DO_{19} type structure. A DO_{19} unit cell with the Ti and Al atom positions is shown in Figure 1.

As mentioned earlier, the positions of the proposed phase boundaries vary over a considerable compositional and temperature range. To illustrate this point graphically, Figures 2,3 and 4 are presented.

Figure 2 is the phase diagram of the Ti-rich end of Ti-Al system as proposed by Bumps, Kessler and Hansen [Ref.2]. In this figure there is no mention of the Ti_3Al or the Ti_2Al phase.

Figure 3 is the proposed phase diagram of the Ti-rich end of the Ti-Al system according to Ence and Margolin [Ref. 14]. It is important

ATOM POSITIONS:

Ti (White): $(1/2, 1/2, 0)$; $(0, 1/2, 0)$; $(1/2, 1/2, 0)$
 $(1/3, 1/6, 1/2)$; $(5/6, 1/6)$; $(5/6, 2/3, 1/2)$

Al (Black): $(0, 0, 0)$; $(1/3, 2/3, 1/2)$

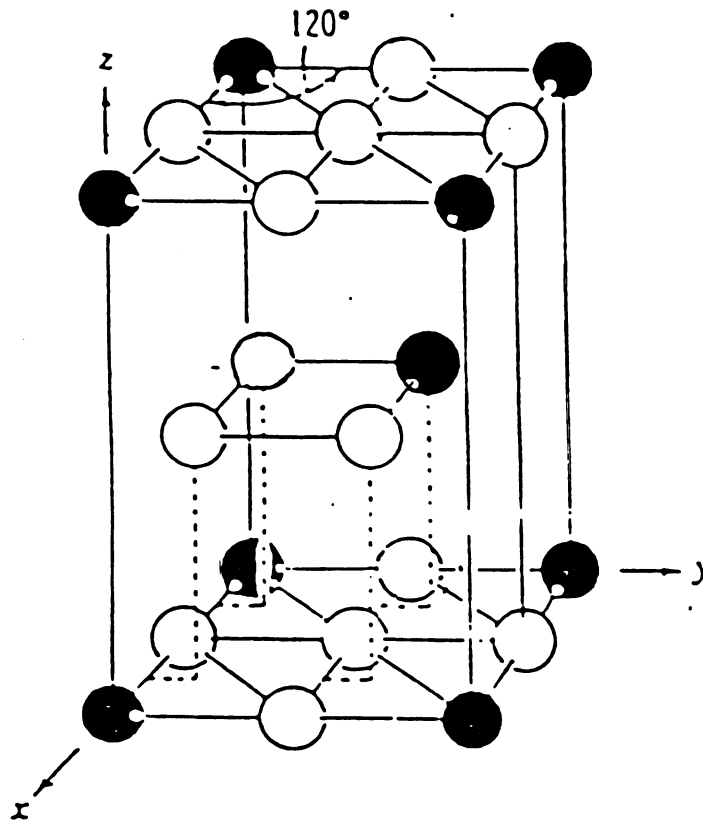


Figure 1. D0₁₉ crystal structure showing the atom positions.

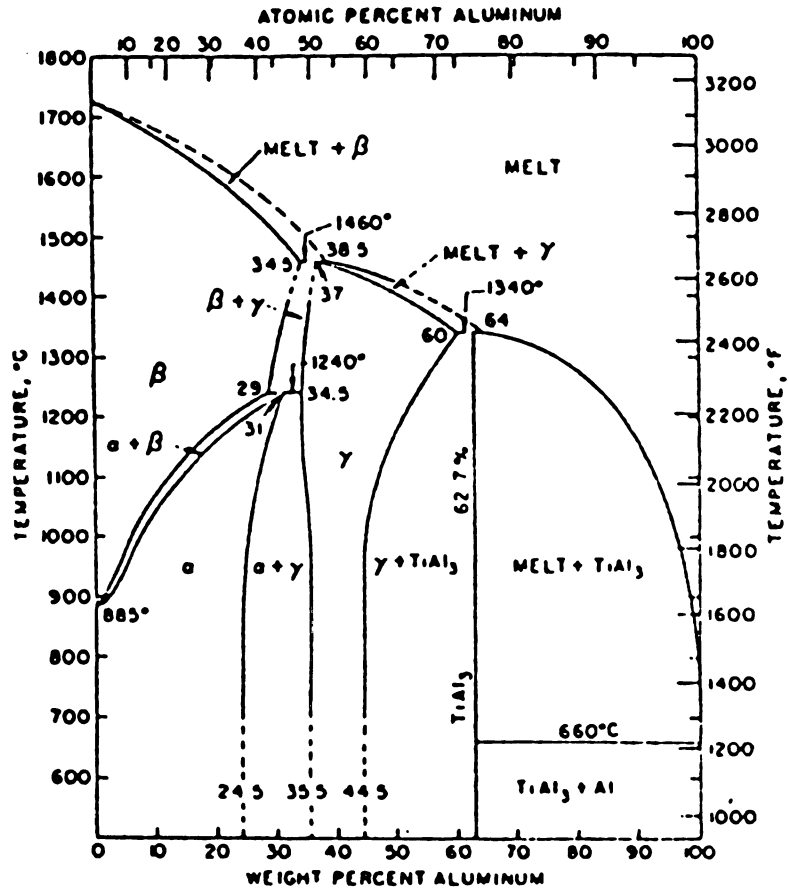


Figure 2. Phase diagram as proposed by Bumps and Kesler.
[Ref. 2]

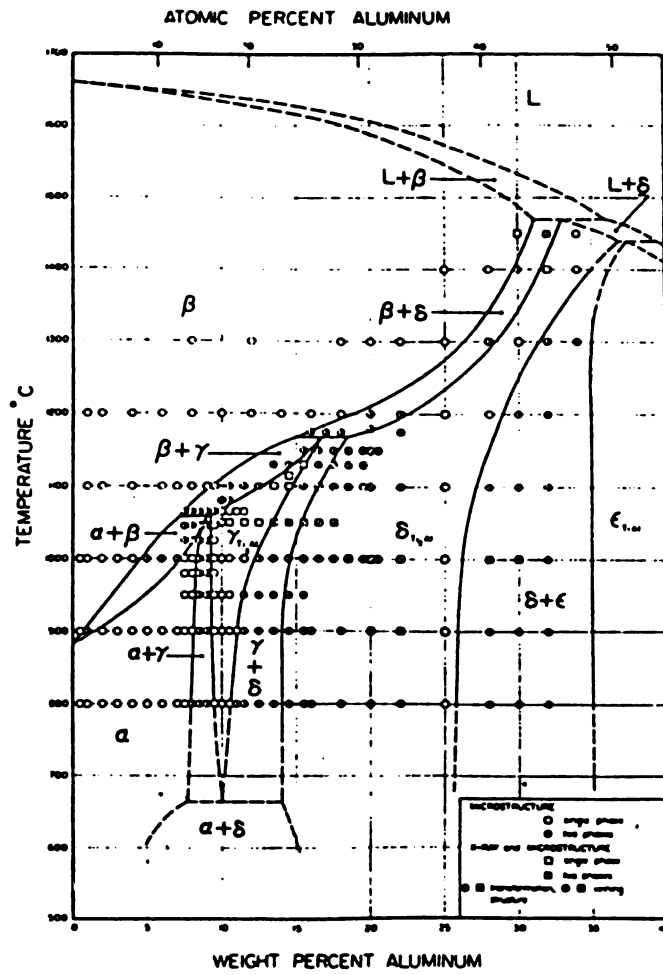


Figure 3. Phase diagram as proposed by Ence and Margolin.
 [Ref. 14]

to note the vast differences in the two phase diagrams, especially the existence of the phases missing above.

Figure 4 is the phase diagram proposed by Crossley [Ref. 18]. In his diagram, the Ti_3Al phase exists only as a stoichiometric line compound instead of a single phase extending over a wide range of composition, as suggested by various authors [Ref. 14,19,20,21].

There are various factors which contribute to these discrepancies. At this point it is perhaps important to briefly examine the techniques used by other workers in the establishment of the phase diagrams. These basically fall into three categories, namely: (1) X-ray diffraction, the only limitation of which is the rather low intensity of the superlattice reflections in this system [Ref. 13,19]. Thus, superlattice reflections become increasingly difficult to detect in more dilute aluminum alloys. (2) A considerable amount of optical microscopy has been performed [Ref. 14,16,18], and many obscure microstructures that have been observed have been attributed to hydrogen contamination [Ref. 19]. (3) The variation of some physical property with aluminum content is another method utilized by other investigators [Ref. 4,22,23]. The methods such as electrical resistivity measurements etc. are extremely good tools to indicate the existence of a transformation, but is not sensitive enough to identify the transformation.

Considerable amount of electron microscopy work has been performed in the Ti-rich end of the Ti-Al system by Blackburn [Ref. 19]. A lot of work has been / is being performed by other authors also [Ref. 21,24,25,26] on on this system, both in the past and now. Blackburn's results appear to stand out as accurate and in general agreement with much of the work done later on by other workers [Ref. 21,24,26,27,28].

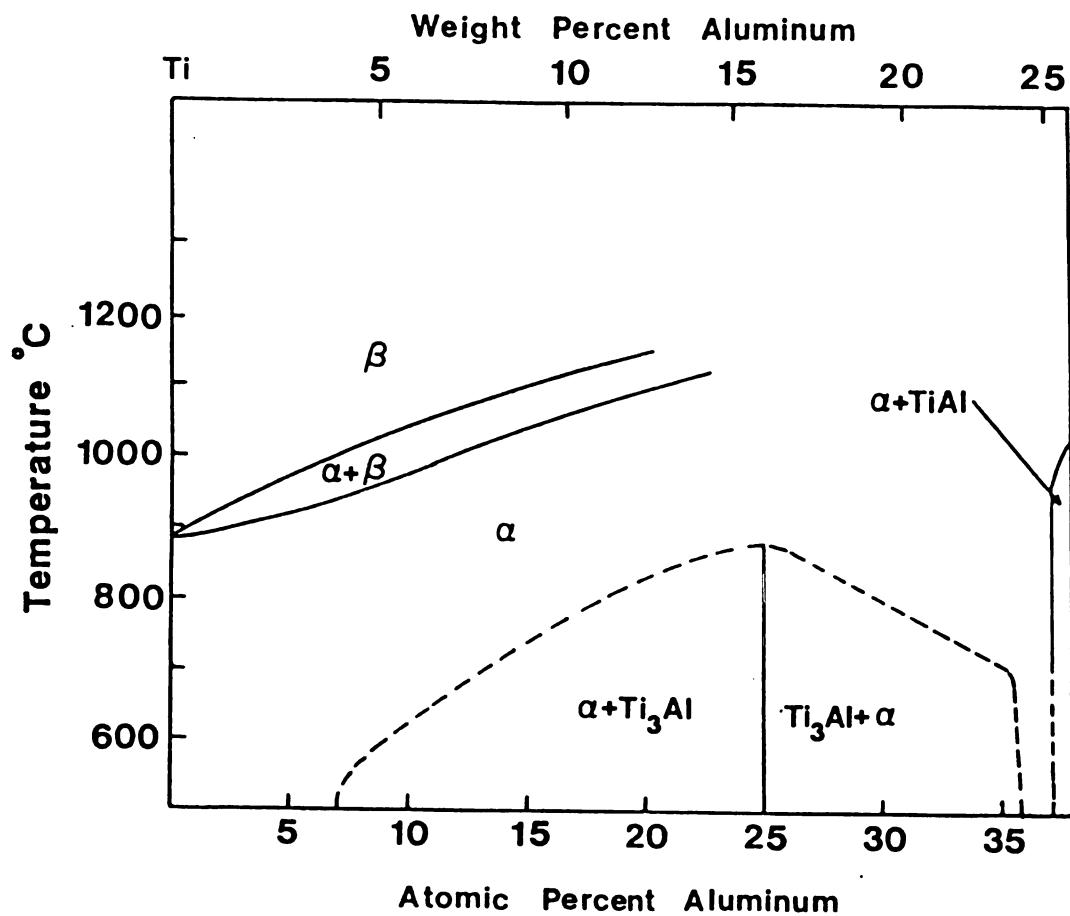


Figure 4. Phase diagram of the Ti-rich end of the Ti-Al system as proposed by Crossley [Ref. 18].

The diagram proposed by Blackburn is shown in Figure 5. This diagram is based on the electron microscopic studies conducted by Blackburn on a series of Ti-Al binary alloys. The boundary between $\alpha:\alpha+\alpha_2$ phase fields has been taken as the limit of resolvable α_2 particles by the dark-field techniques. The resolvable thickness of disordered material between ordered domains has been taken as the $\alpha_2:\alpha+\alpha_2$ phase boundaries. However, Blackburn has also indicated in the phase diagram proposed by him the limits of the phase diagram where an ambiguous phase contrast is noticeable. This reduces the phase stability range of the α_2 phase.

2.1.1 Differential Thermal Analysis of Titanium Alloys

Crossley [Ref. 18] was among the first few workers who applied dilatometry to study order-disorder transformation in Ti-Al alloys. He studied the change in length/original length for a series of Ti-Al alloys containing 10, 12, 14, 16 and 18 at.% Al, when the samples were cooled from 1125°C. The next two figures (Figures 6 and 7), show some of the results from Crossley's work. Figure 6 shows the change in length/original length plotted vs. temperature for various percentages of aluminum. Data for each of the alloys showed a linear relationship between room temperature and some temperature between 600 and 800°C and a linear relationship of a greater slope for the next 150°C or more. Crossley analysed these two linear segments by the method of averages and solved the resulting equations simultaneously for the temperature of transformation. Figure 7 indicates the $\alpha \rightarrow \alpha + \text{Ti}_3\text{Al}$ continuous cooling transformation temperature vs. aluminum content of binary titanium alloys from dilatometry data as obtained by Crossley.

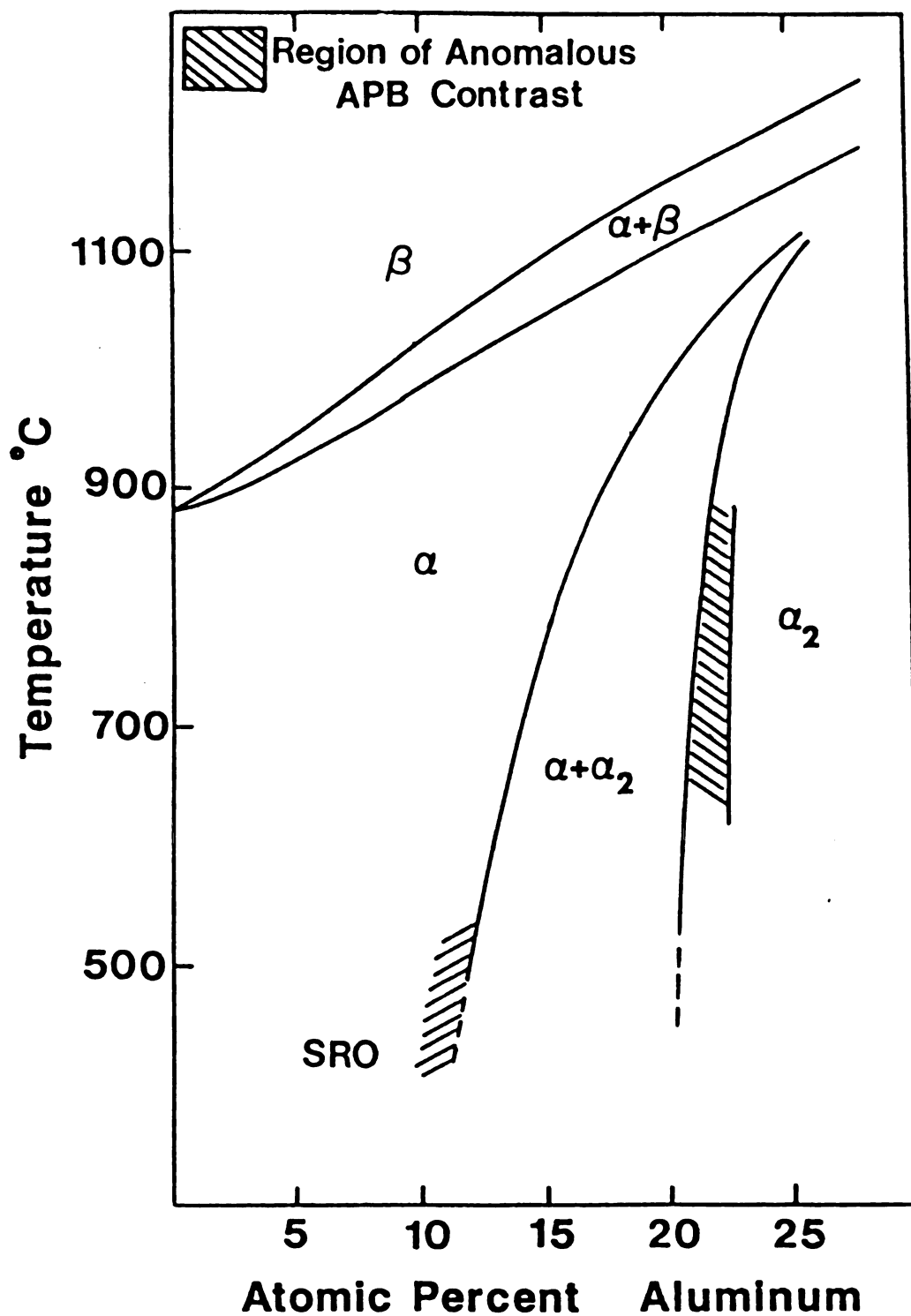


Figure 5. Phase diagram of the Ti-rich end of the Ti-Al system as proposed by Blackburn [Ref. 19].

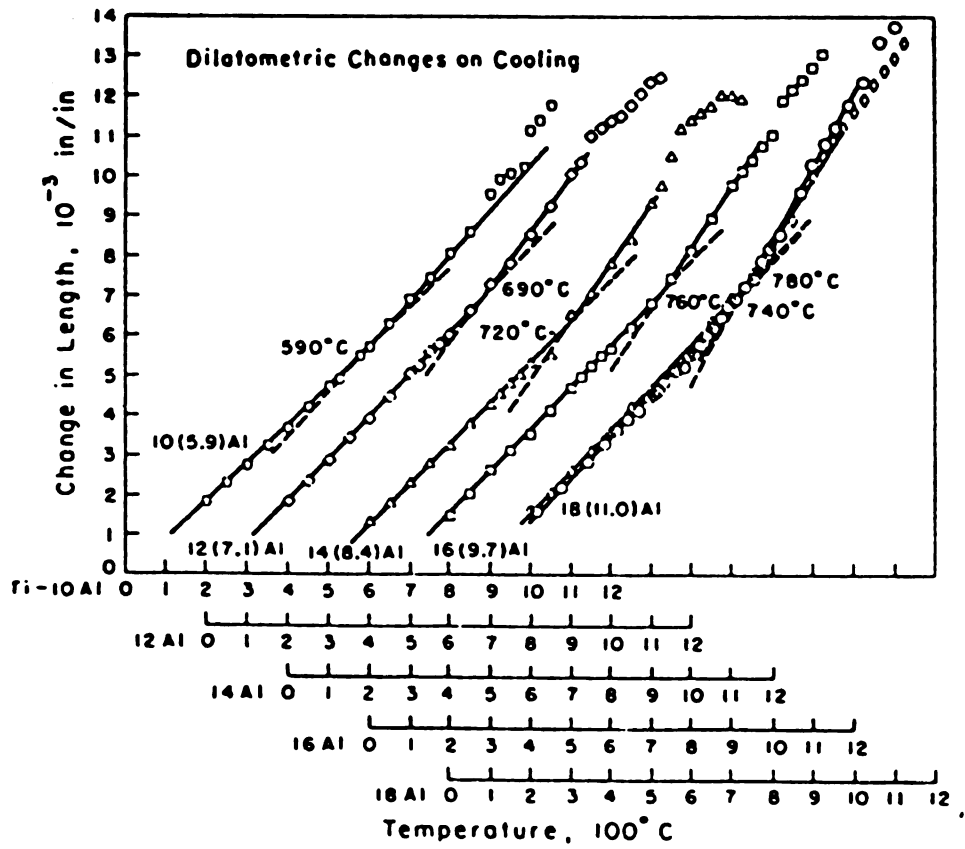


Figure 6. Dilatometry data for Ti-Al binary alloys on cooling from 1125° C as obtained by Crossley [Ref. 18].

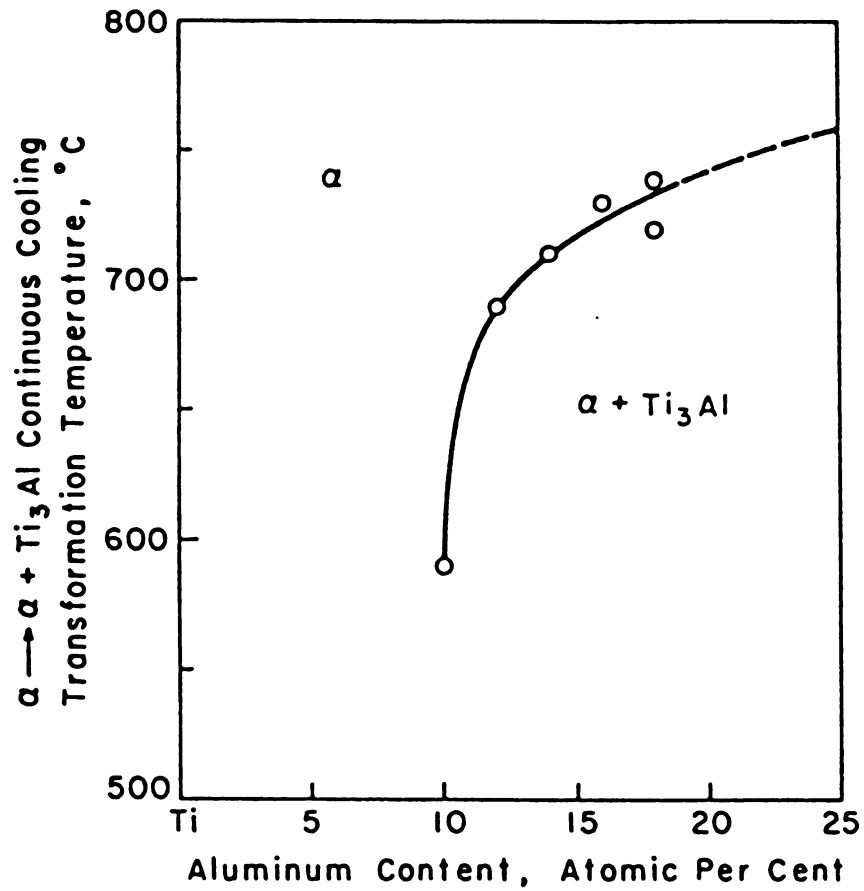


Figure 7. $\alpha \rightarrow \alpha + \text{Ti}_3\text{Al}$ continuous cooling transformation temperature vs. aluminum content of binary Ti-Al alloys from dilatometry data, after Crossley [Ref. 18].

Some differential thermal analysis has also been done on Ti-Al alloys by Chen and Sparks [Ref. 29]. They used a high temperature differential thermal analyzer (DuPont Model 990) with a high temperature furnace attachment with programmable heating rate control circuitry. They obtained phase change temperatures in various Ti alloys. But they did not perform any work on the order-disorder transformation in Ti-Al alloys.

Very recently Shull et. al. [Ref. 24,30] has performed some Differential Scanning Calorimetry (DSC)/ Differential Thermal Analysis (DTA) to study the ordering phenomenon in Ti-6Al-2Nb-1Ta-0.8Mo (Ti-6211) alloy and Ti-15 at% Al alloy. A detailed discussion on DTA system and its operation principles is given in the "experimental techniques" section of this thesis.

The results obtained by Shull et. al. are shown in the graphs plotted in Figure 8. Both the samples were initially equilibrated at 625°C for 378 hrs. and hence the two DSC/DTA profiles indicate two endothermic responses on heating - one centered around 825°C corresponding to the $\alpha_2 \rightarrow \alpha$ reaction and the other centered around 1140°C which corresponds to $\alpha \rightarrow \beta$ transition. They have also determined the transformation enthalpies for these two transformations [Ref. 30]

2.2 ORDER-DISORDER TRANSFORMATIONS.

In most substitutional solid solutions, the two kinds of atoms A and B are arranged more or less at random on the atomic sites of the lattice. In solutions of this kind, the only major effect of a change

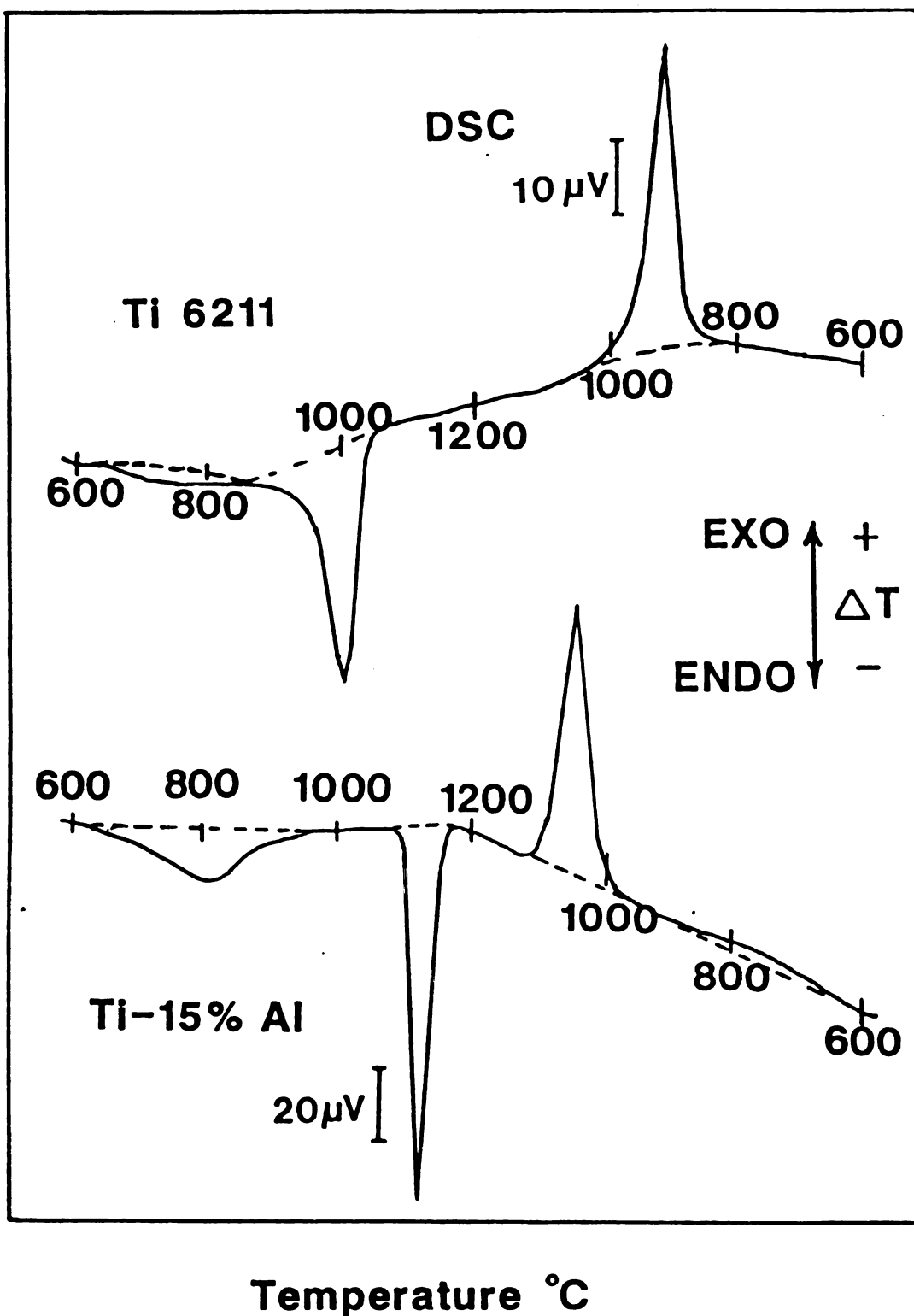


Figure 8. DSC/DTA data obtained on aged Ti-15 at.%Al and as received Ti-6211 alloy samples. Heating and cooling rates are 30°C/min., after Shull et. al. [Ref. 30].

in temperature is to increase or decrease the amplitude of thermal vibration. But there are some solutions which have a negative enthalpy of mixing ($\Omega < 0$, to be discussed in detail later on), prefer unlike nearest neighbors and therefore show random atomic arrangements only at elevated temperatures. When these solutions are cooled below a certain critical temperature, T_c , the A atoms arrange themselves in an orderly, periodic manner on one set of atomic sites, and the B atoms do likewise on another set. The solution is then known as an ordered solid solution or is said to possess a superlattice. When this periodic arrangement of A and B atoms persists in the limit of infinite distance (for an infinite sample) in the crystal, it is known as long-range order. If the ordered solution is heated above T_c , the atomic arrangement becomes more or less random again and the solution is said to be disordered and the long range order is lost.

The five main types of ordered solutions are shown in the next Figure 9. They are discussed in detail later in this section.

An example of a phase diagram containing low temperature ordering reactions is the Au-Cu diagram shown in the next Figure 10. Another example is the ordering of b.c.c β -brass below $\approx 460^\circ\text{C}$ to the so called $L2_0$ (or $B2$) superlattice. The b.c.c (or so called $A2$) lattice can be considered as two interpenetrating simple cubic lattices: one containing the corners of the b.c.c unit cell and the other containing the body centered sites. If these two sublattices are denoted as I and II, the formation of a perfectly ordered β' superlattice involves segregation of all Cu (A) atoms to the I sublattice, say, and Zn (B) to the II sublattice. This perfect segregation is not feasible in practice, however, as the β' does not have the ideal CuZn composition. There are two ways of

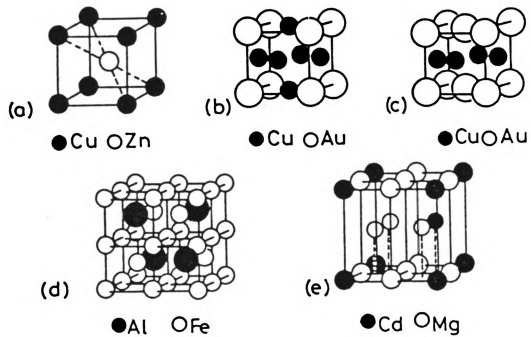


Figure 9. The five common ordered lattices, (a) $L2_0$, (b) $L1_2$, (c) $L1_0$, (d) $D0_3$ and (e) $D0_{19}$. (After R. E. Smallman, *Modern Physical Metallurgy*, 3rd. Edition, Butterworths, London, 1970.)

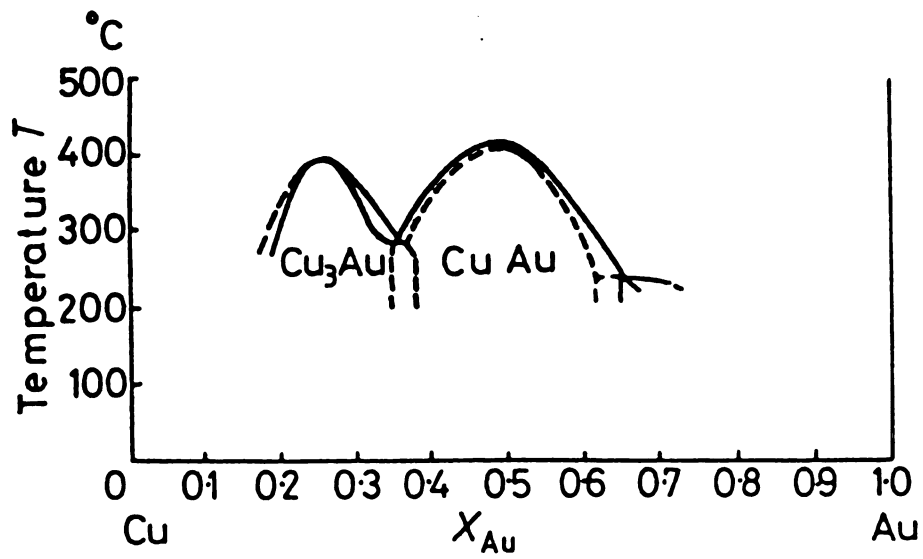


Figure 10. Part of the Cu-Au phase diagram showing the region where the Cu_3Au and CuAu superlattices are stable.

forming ordered structures in non-stoichiometric phases: either some sites can be left vacant or some atoms can be located on wrong sites. In the case of β (CuZn) the excess Cu atoms are located on some of the Zn sites.

In a disordered solid solution, crystallographically equivalent planes (as referred to the disordered lattice structure) of atoms are identical (statistically) with one another, but in an ordered superlattice this may not be true. For example, alternate planes of a set may become A rich and B rich planes respectively, and the distance between identical planes may be twice the distance between identical planes of the disordered alloy (or some multiple distance). Hence, the structures of ordered alloys usually produce diffraction patterns that have additional Bragg reflections, the superlattice reflections associated with the new and largest spacings which are not present in patterns of the disordered alloys. Bain [Ref. 31] in 1923 and Johansson and Linde [Ref. 32] in 1925 were the first to observe these lines with x-ray diffraction, though the possibility of ordering had been by considered some years earlier by Tammann [Ref. 33].

2.3 COMMON TYPES OF SUPERLATTICES.

The majority of typical superlattices are related to the three principal metallic structures, the f.c.c. (A1), the b.c.c (A2) and the h.c.p. (A3). It is becoming a generally accepted practice to refer to specific superlattice types by their Strukturbericht designations, although these are in general available only for the more commonly occurring types. The Strukturbericht-Structure Reports symbols for crystal structure types are given in the following table (Table I).

TABLE I
STRUKTURBERICHT-STRUCTURE REPORTS CRYSTAL STRUCTURE TYPES SYMBOLS.

A types	Elements
B types	AB compounds
C types	AB ₂ compounds
D types	A _m B _n compounds
E...K types	More complex compounds
L types	Alloys
O types	Organic compounds
S types	Silicates

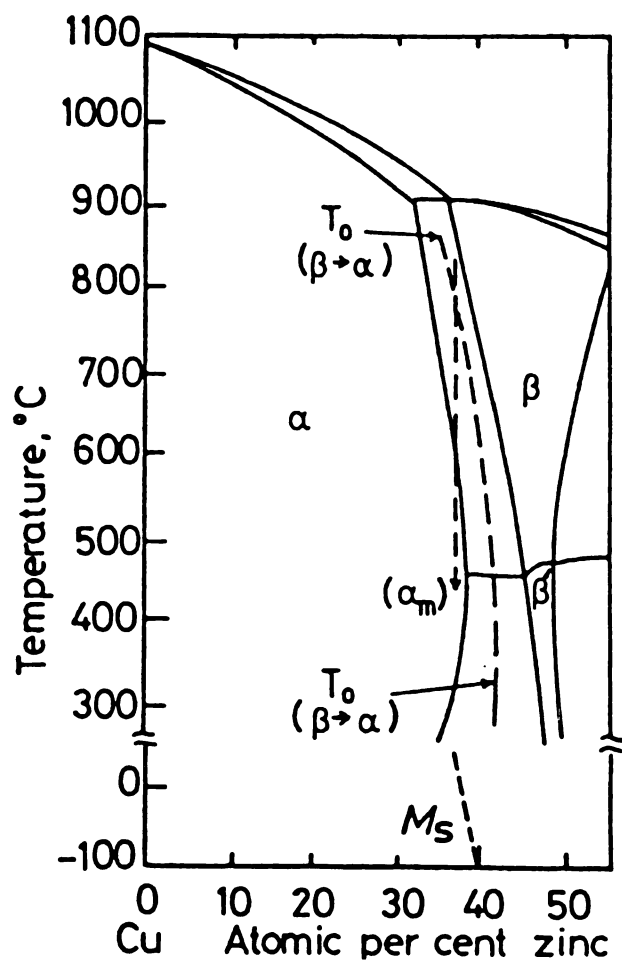
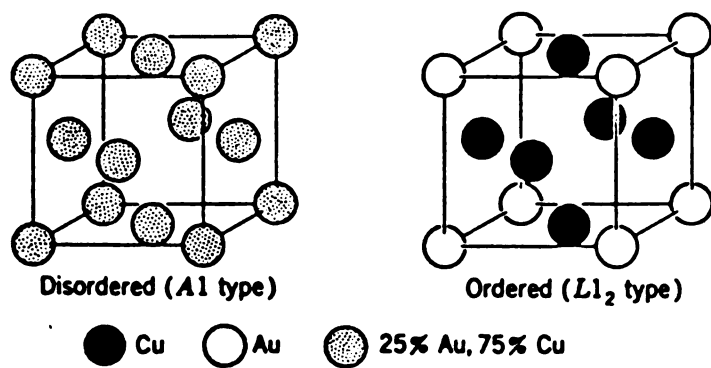
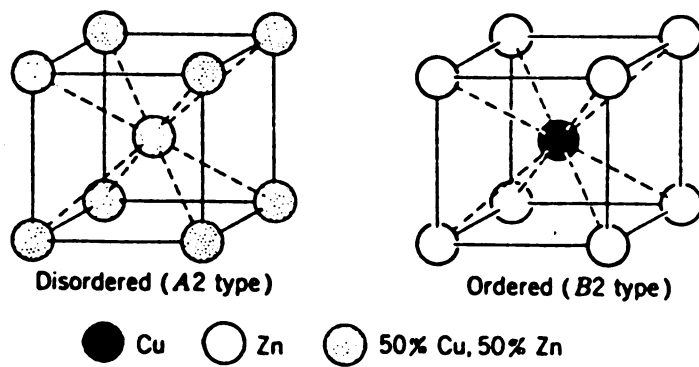
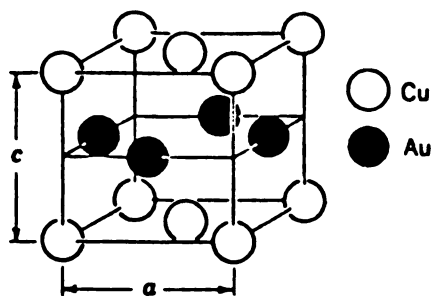


Figure 11. Part of the Cu-Zn phase diagram showing the order disorder transformation ($\beta \rightarrow \beta'$).

Thus, for example closely related superlattices based upon the disordered A2 structures are the B2, DO₃ and L2₁ types of which typical examples are the ordered β -brass (CuZn), the ordered Fe₃Al alloy and the Heusler alloy (Cu₂MnAl), respectively. Superlattices A1 and A3 are frequently of the L1₂, DO₁₉, and L1₀ types, characterized, for example, by the ordered structures AuCu₃, Mg₃Cd and CuAu-I, respectively. Examples of these structures will be considered in short below.

2.3.1 The L1₂- or Cu₃Au-I Type Superlattice

Historically, Cu-Au alloys containing about 25 at.% Au were among the first investigated. In the disordered state, which exists at high temperatures, Cu₃Au-I has nearly a random array of Au and Cu atoms on a f.c.c. lattice (Figure 12). If the alloy is annealed below a critical temperature, about 390°C (Figure 10), the atoms segregate as shown in the drawing of the ordered Cu₃AuI structure, the Au atoms going to the cube corners and Cu atoms to the face centers. The unit cell shown in Figure 12 can thus be thought of having Au atoms at (0,0,0) positions and Cu atoms at (1/2,0,1/2), (1/2,1/2,0) and (0,1/2,1/2) positions, and is a prototype of four interpenetrating simple cubic sublattices, each occupied by atoms of only one kind. This represents the condition when ordering is complete, the equilibrium condition at low temperatures. the L1₂ structure has been observed in some sixty alloy systems. Typical examples are Cu₃Au-I, α'' -Au₃Cd, α' -AlCo₃, Pt₃Sn, Al₃U, AlZr₃, Co₃V, FeNi₃, FePd₃, MnNi₃, Si₃U, TiZn₃, Tl₃U etc.

Figure 12. The superlattice of Cu_3Au .Figure 13. The superlattice of β -brass.Figure 14. The tetragonal superlattice CuAu .

2.3.2 The B2-, or β -brass Type Superlattices

The superlattice in β -brass is illustrated in Figure 13. It was first established by Jones and Sykes [Ref. 34], who used x-ray techniques. The unit cell can be represented in terms of two interpenetrating simple cubic sublattices. The disordered crystal is b.c.c. (A2) with equal probabilities of having copper and zinc atoms at each lattice point; the ordered structure has copper atoms and zinc atoms segregated to cube corners and centers, respectively, in a structure of the CsCl type. This type of superlattice is very frequently encountered in alloy systems. B2 structure has been observed in some seventy systems. Typical examples are β' -CuZn, β -AuCd, β -AlNi, β -NiZn, LiTl etc.

2.3.3 The L1₀-, or CuAu-I Type Superlattice

In Cu-Au system (Figure 10) from 47 to 63 at.%, a superlattice forms in which alternate (001) planes contain only Cu or Au atoms. Hence, each atom has eight nearest neighbors of opposite kind in the adjacent (001) planes and four of the same kind in its own (001) plane. This is illustrated in Figure 14. The resulting structure is tetragonal with axial ratio approximately $c/a = 0.93$, which is a deviation of about 7% from unity. At the stoichiometric composition, CuAu, this ordered structure forms below approximately 385°C (Figure 10) and is commonly known as CuAuI. Its Strukturbericht designation is L1₀.

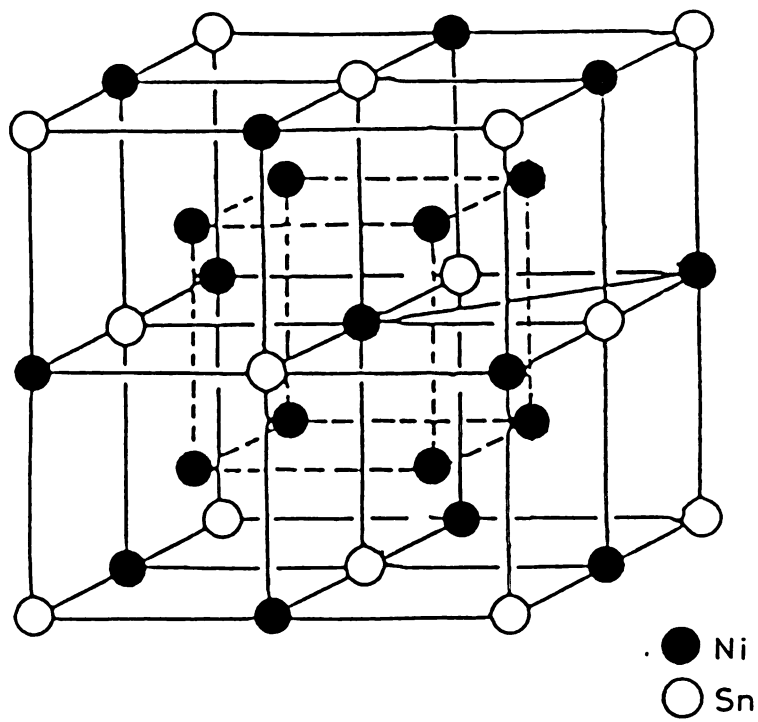


Figure 15. The superlattice of the DO_3 type structure.

2.3.4 The DO₃ Superlattice

This superlattice is derived from the b.c.c. structure, but it is much more complex than the B2 superlattice. This structure has a cubic unit cell formed from eight conventional b.c.c. unit cells, and thus containing sixteen atoms; the ideal composition being A₃B. The corner positions of the small cubic cells are occupied by equal numbers of atoms of each kind, each set being arranged on tetrahedral groups of sites. The body centered positions of the small unit cells are occupied entirely by A atoms. Each B atom has eight unlike nearest neighbors in the superlattice, compared to an average of two like and six unlike nearest neighbors in the substantially disordered solid solution. An illustration showing the DO₃ crystal lattice is shown in the next Figure (Figure 15).

2.3.5 The DO₁₉-or Mg₃Cd Type Superlattice

A superlattice closely related to the L1₂ type of AuCu₃ is the DO₁₉ superlattice with the unit cell shown in Figure 1. Here again the cell can be described in terms of four interpenetrating sublattices, each having one atom per unit cell, and the arrangement of atoms in the close packed planes of both structures is identical. However, unlike the L1₂ type, each sublattice in the DO₁₉ type is c.p.h. with the "a" spacing corresponding to twice the spacing of the disordered structure

TABLE II COMMON SUPERLATTICE STRUCTURES

Disordered structure	Superlattice type	Composition	Atom positions	Examples
f.c.c.	$L1_0$ (tetragonal)	AB	$2A$ in $(000; \frac{1}{2} \frac{1}{2} 0)$ $2B$ in $(\frac{1}{2} 0 \frac{1}{2}; 0 \frac{1}{2} \frac{1}{2})$	AuCu, CoPt, MgIn MnNi, NiPt, FePd, FePt
f.c.c.	$L1_2$ (cubic)	A_3B	$3A$ in $(0 \frac{1}{2} \frac{1}{2}; \frac{1}{2} 0 \frac{1}{2}; \frac{1}{2} \frac{1}{2} 0)$ $1B$ in (000)	Cu ₃ Au, Au ₃ Cu, Pt ₃ Co, Fe ₃ Pt, Pt ₃ Fe, Cu ₃ Pt, Ni ₃ Mn, etc.
b.c.c.	$B2 (L2_0)$ (cubic)	AB	$1A$ in (000) $1B$ in $(\frac{1}{2} \frac{1}{2} \frac{1}{2})$	CuZn, CuPd, AgCd, AgZn, CoFe
b.c.c.	$D0_3$ (cubic, face-centred)	A_3B	$(000; 0 \frac{1}{2} \frac{1}{2}; \frac{1}{2} 0 \frac{1}{2}; \frac{1}{2} \frac{1}{2} 0)$ $+ 4B$ in (XXX) $4A$ in $(\frac{1}{2} \frac{1}{2} \frac{1}{2})$ $8A$ in $(\frac{1}{4} \frac{1}{4} \frac{1}{4}; \frac{3}{4} \frac{3}{4} \frac{3}{4})$	Fe ₃ Al, Fe ₃ Si, Mg ₃ Li, Cu ₃ Al
h.c.p.	$D0_{19}$ (hexagonal)	A_3B	$6A$ in $(\frac{1}{2} 00; 0 \frac{1}{2} 0; \frac{1}{2} \frac{1}{2} 0;$ $\frac{1}{6} \frac{1}{6} \frac{1}{6}; \frac{5}{6} \frac{5}{6} \frac{5}{6}; \frac{2}{3} \frac{2}{3} \frac{2}{3})$ $2B$ in $(000, \frac{2}{3} \frac{2}{3} \frac{2}{3})$	Ag ₃ In, Mn ₃ Ge, Mg ₃ Cd, Cd ₃ Mg, Ni ₃ Sn

and the "c" spacing unchanged. B atoms occupy one of the four sublattices, resulting in the general formula A_3B , for example in the case of Mg_3Cd or $MgCd_3$, which are perhaps the best known examples of DO_{19} superlattices.

Over the last several years a large number of alloy phases have been discovered which possess the c.p.h structure at high temperatures and which undergo ordering on cooling. The known DO_{19} superlattices and their axial ratios are as follows: $Al_3Th(0.712)$, $\beta''-Fe_3Sn(0.799)$, $Cd_3Mg(0.8093)$, $CdMg_3(0.8038)$, $\beta-Ni_3Sn(0.8018)$, $Ti_3Al(0.8062)$ etc. Some common types of superlattices and their compositions and atom positions are given in the following table (Table II) [Ref. 35].

2.4 ORDERING TRANSFORMATIONS

Let us begin the discussion of ordering transformations by considering what happens when a completely ordered single crystal such as $CuZn$ or Cu_3Au is heated from low temperatures to above the disordering temperature. To do this it is useful to quantify the degree of order in a crystal by defining a long range order parameter W such that $W = 1$ for a fully ordered alloy, where all atoms occupy then 'correct' sites and $W = 0$ for a completely random distribution. A suitable definition of W is given by,

$$W = \frac{P_{A.I} - X_A}{1 - X_A}, \quad \text{or,} \quad \frac{P_{B.II} - X_B}{1 - X_B}$$

where X_A and X_B are the mole fractions of elements A and B in the alloy respectively. (Please refer to the opening section on order disorder transformation in this thesis). $P_{A,I}$ is the probability of finding A atom in sublattice I which is the home of A atoms and similarly $P_{B,II}$ is the probability of finding B atoms in sublattice II which is the home of B atoms.

At absolute zero, the crystal will minimize free energy by choosing the most highly ordered arrangement ($W = 1$) which corresponds to the lowest internal energy. The configurational entropy of such an arrangement, however, is zero and at higher temperatures the minimum free energy state will contain some disorder, that is, some atoms will interchange positions by diffusion so that they are located on 'wrong' sites. Entropy effects become increasingly important as temperature increases so that W continuously decreases until above some temperature (T_c), $W = 0$. By choosing a suitable model, such as the quasi-chemical model (which will be discussed in detail in a later section), it is possible to calculate how W varies with temperature with different superlattices. A schematic representation of such a calculation for CuZn and Cu₃Au is shown in the next Figure (Figure 16). It can be seen that the way in which W decreases to zero is different for the different superlattices. In the case of equiatomic CuZn, W decreases continuously with temperature upto T_c , whereas, in the case of Cu₃Au, W decreases only slightly upto T_c and then abruptly drops to zero above T_c . This difference in behavior is a consequence of the different atomic configurations in the two superlattices.

It can be seen from Figure 16 that, the loss of long-range order in the $\beta' \rightarrow \beta$ (CuZn) transformation corresponds to a gradual disordering of the structure over a range of temperatures. There is a change of order at T_c , the long range order parameter decreases to zero continuously as $T \rightarrow T_c$ from below and remains zero above T_c . Consequently, the internal energy and enthalpy will be continuous across T_c . The $\beta' \rightarrow \beta$ transformation is therefore a second order transformation. In the case of Cu_3Au , on the other hand, a substantial change in the order takes place discontinuously at T_c . Since the disordered state will have a higher internal energy (and enthalpy) than the ordered state, on account of the greater number of the high energy like atom bonds, there will be a discontinuous change in internal energy and enthalpy across T_c , that is the transformation is of the first order type.

Now turning to the reverse transformation, that is, from disorder \rightarrow order. There are two possible mechanisms for creating an ordered superlattice from a disordered solution. (1) There can be a continuous increase in short-range order by local rearrangements occurring homogeneously throughout the crystal which finally leads to long-range order. (2) There could be an energy barrier to the formation of ordered domains, and in such a situation the transformation process must take place by a process of nucleation and growth. The first mechanism corresponds to spinodal decomposition type of reactions, whereas, the the second mechanism is similar to precipitation as the mode of formation of coherent zones in some alloys. The second mechanism is believed to be more common.

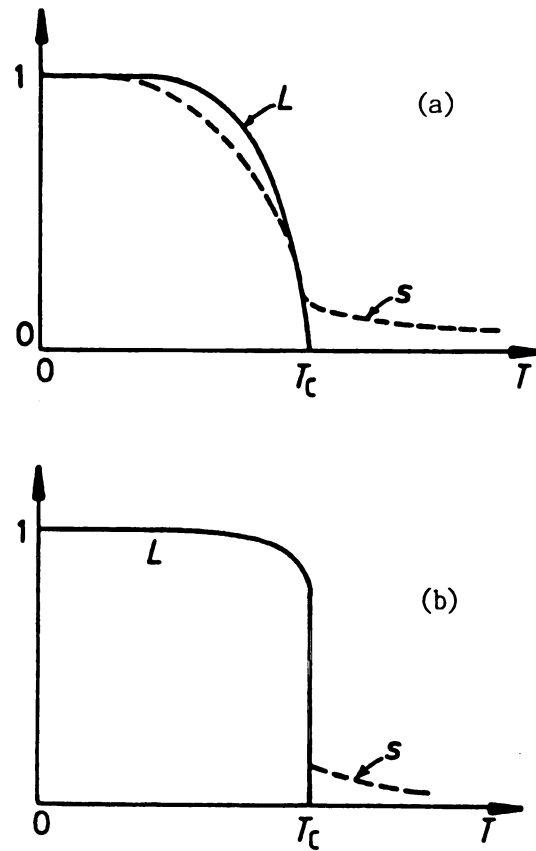


Figure 16. The variation of long range order parameter with temperature for (a) CuZn type and (b) Cu_3Au type transformations. (Schematic)

The nucleation and growth process (which is the second mechanism mentioned) is illustrated in the next Figure (Figure 17). The disordered lattice is represented by cross-grid of lines. Within this lattice, two sublattices are marked by heavy and faint lines. Atoms are located at each intersection by only atoms within the ordered regions, or domains, are marked; the unmarked sites are disordered. The diagram is schematic and could be considered to be the (100) plane of the Cu_3Au superlattice. Since the two types of lattices, I and II can grow independently, nucleated domains will often be 'out of phase' as shown in the Figure (Figure 17). When these domains grow together, a boundary will form, as shown in Figure 17, known as an antiphase domain boundary (or APB) across which the atoms will have the wrong kind of neighbors (like). APBs are therefore high energy regions of the lattice and are associated with an APB energy.

At rather low undercoolings below T_c , the activation energy barrier to the nucleation of ordered domains ΔG^* should be rather small because both the nucleus and matrix have essentially the same crystal structure and are therefore coherent with a low interfacial energy. Also it is conceivable that in the case of stoichiometric compositions, since, the composition of the matrix and the nucleus are the same, there should not be large strain energies to be overcome.

2.4.1 Ordered Domains

In a superlattice in which the long-range order is not perfect, many different atomic configurations are possible. One possibility is a single long range order scheme that has occasional atoms out of place on

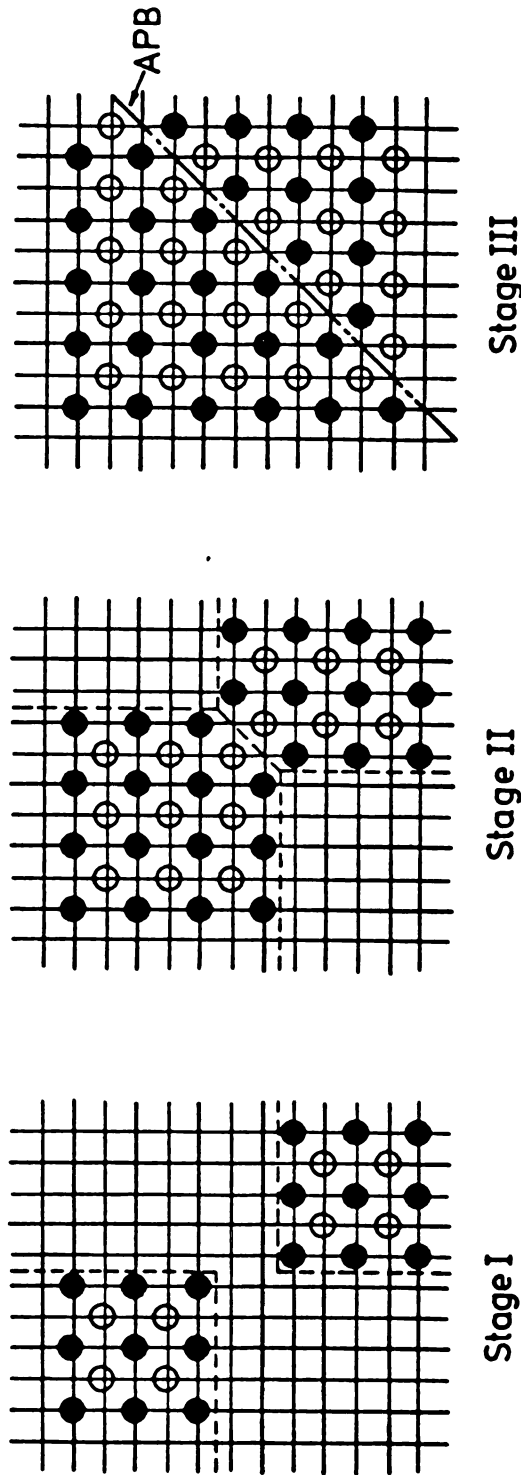


Figure 17. The formation of an antiphase boundary (APB) when out-of-phase ordered domains grow together. The diagram could represent a (100) plane in Cu₃Au in which case the black and white atoms could represent Cu and Au. (After P. Hansen, Physical Metallurgy, Cambridge University Press, Cambridge, 1978.)

the atom sites of the crystal. Another possibility is that of many domains each of which has a long-range scheme of perfect or partial order but an arrangement of atoms that is out of phase with the arrangements in each adjacent domain (Figure 17). Also, there may or may not be a two-phase arrangement, in which a partially ordered phase coexists with a disordered phase (or with a partially ordered phase of a different superlattice structure).

If the domains come in contact, the region of contact between them is a surface or domain wall. A certain amount of disorder exists there, since atoms in the vicinity of the wall will have some neighbors out of step with their other neighbors. Such atoms will find it easier to disorder than those inside the domains, causing the disordered band to widen as the temperature increases. A number of calculations of the surface energy of domain walls, and their dependence upon orientation and composition, have been made for a variety of structures. [Ref. 36, 37, 38].

X-ray investigations have not always been adequate to distinguish between various possible models of the scheme of ordering. Some x-ray results have been interpreted solely in terms of one scheme arbitrarily chosen. An important feature of incompletely ordered samples is the tendency for domain boundaries to lie along certain planes so as to minimize domain-boundary energies. The preference for one type of boundary over another influences the short-range-order parameters; likewise, the effective mean size of the domains and the effective thickness of the domain walls influence the parameters. Thus, although much can be deduced from x-ray data alone [Ref. 39], a full specification of the state of order in a partially ordered superlattice is a complex matter than cannot be readily deduced from x-ray studies alone.

A marked advance in the knowledge of partially ordered structures occurred when it was found that the boundaries could be seen in electron micrographs, and the crystallographic nature of each boundary could be interpreted by studying contrast effects in the pictures.

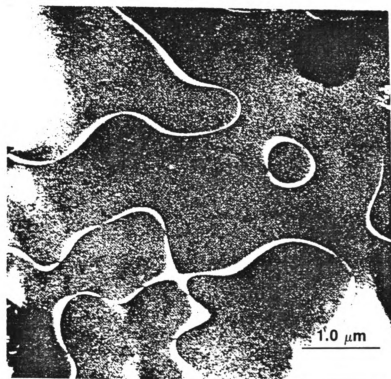
Antiphase domain boundaries can result not only from the growing together of different nuclei of order, but also from the passage of dislocations through an ordered crystal. A perfect dislocation having a unit Burgers vector in the disordered alloy is only a partial dislocation in the ordered alloys, since the unit cell for the ordered state is larger than for the disordered. A movement of such a dislocation across a slip plane in a superlattice therefore leaves a plane behind it that is an antiphase boundary. In order to avoid the extra energy involved in producing this boundary, dislocations in a superlattice tend to travel in pairs, with only a narrow ribbon of antiphase boundary extending from one to the other [Ref. 40]. The passage of the second dislocation of the pair restores the ordered structure.

When we are moving from a disordered structure towards ordering (by lowering the temperature of the disordered material), we know that at low $\Delta T (T \approx T_c)$, the nucleation rate would be low but the resulting mean domain size is large. However, at higher values of ΔT , the nucleation rate increases, but the mean domain size diminishes. The degree of long range order in a given domain would vary with temperature according to Figure 16, and by decreasing the temperature the degree of order will increase by homogeneous diffusive rearrangements among atoms within the domain. Within the crystal as a whole, the degree of long range order will initially be very small because there are likely to be equal numbers of domains ordered on both I (home of A(Cu) atoms) and II (home of

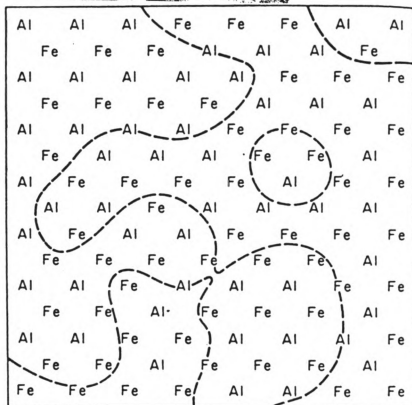
B(Zn) atoms) lattices. The only way for long range order to be established throughout the entire crystal is by the coarsening of the APB structure. The rate at which this occurs depends on the type of superlattice.

In CuZn-type superlattice ($L2_0$) there are only two sublattices on which Cu atoms, say, can order and therefore only two distinct types of ordered domains are possible. A consequence of this is that it is very difficult for a metastable APB structure to form. It is therefore relatively easy for the APB structure to coarsen in this type of ordered alloy. Figure 18a shows an electron micrograph of APB's in AlFe ($L2_0$ superlattice) along with a schematic diagram (Figure 18b) to illustrate the two different types of domain. This type of domain structure is known as "swirl" type of domain structure, as has been referred to by various authors [Ref. 25, 41]. The Cu_3Au ($L1_2$) superlattice is different to the above in that there are four different ways in which ordered domains can be formed from the disordered f.c.c. lattice. The Cu_3Au APB are therefore more complex than the CuZn type, and a consequence of this is that it is possible for the APB's to develop a metastable, so-called foam or "maze" structure, Fig. 19(a). A schematic representation of the maze pattern formed by domains in Cu_3Au is shown in Figure 19(b).

The subject of study dealing with the domain shapes in extremely interesting and considerable amount of work has been done by various authors [Ref. 25, 37, 41, 42] in order to understand the underlying reasons which can be attributed to the different types of domains and APB's.



(a)



(b)

Figure 18. (a) A thin foil electron micrograph showing APB's in an ordered AlFe alloy. (b) A schematic representation of the atomic configurations comprising structure in (a). (After M. J. Marcinkowski in Metals Handbook, 8th. Edition, Vol. 8, ASM, 1973, p. 205.)

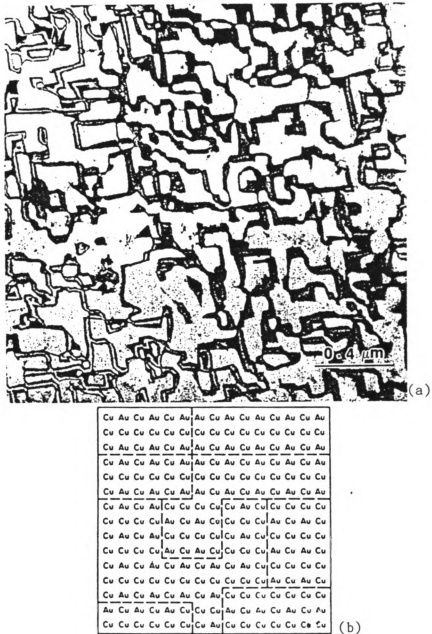


Figure 19. (a) A thin foil electron micrograph showing APB's in ordered Cu_3Au alloy. (After M. J. Marcinkowski, Metals Handbook, 8th. Edition, Vol. 8, ASM, 1973, p. 205). (b) A schematic representation of atomic configurations comprising structure in (a). [Ref. 25]

The antiphase boundary energy in $L1_2$ alloys has been calculated to be anisotropic, with the lowest energy on (001) planes, taking into account first nearest neighbor interactions only [Ref. 37]. Accordingly, there is a driving force for an APB to lie on cube planes in these alloys. When this occurs, the electron microscope shows a "maze" pattern (as in Cu_3Au and Cu_3Pt) rather than the "swirl" pattern that is associated with superlattices having isotropic domain networks and APB energy (Ni_3Fe , Ni_3Mn , Fe_3Al).

It is hypothesized [Ref. 25] that associated with the anisotropy of APB energy the nucleation density of the ordered domains plays an important role in the determination of either the "maze" or the "swirl" type ordered domain patterns. Electron micrographs of the very early stages of the ordering transformation indicate that the density of nuclei is extremely high. Eventually these nuclei will grow into small domains which eventually impinge upon one another. When two like domains come in contact with one another, they will unite to become a larger domain, whereas two unlike domains which come into contact with each other will have one APB formed between them. If the nuclei are considered as small cubes with their faces parallel to (100) planes, then it is apparent that during growth, one fourth of the encounters between nuclei across any of the cube faces will result in the contact of like domains and thus no boundary will be formed between them. On the other hand, three fourths of the encounters across these phases will result in APB's. The encounters across cube faces between like domains will result in the formation of a maze pattern. As domain growth proceeds, the chances of domains of similar kind encountering one another increases proportionately and so does the complexity of the maze

pattern associated with each individual domain, in accordance with the observations in Figure 19(a). It can also be seen from this same figure that as a result of the encounter between domains during growth, many small isolated islands are formed which are entirely surrounded by a single domain of another type. Because of the tension (energy/length) associated with the APB's which delineate these small islands, they eventually disappear.

The morphology of an APB in Cu_3Au can be changed from a maze to a swirl pattern by adding 5 at %Ni [Ref. 41]. This is perhaps due to a reduction in the electron/atom ratio, hence, in the relative phase stability of L1_2 versus long-period superlattices in which periodic (001) APB's are characteristic.

In a work by Sastry and Lipsitt [Ref. 43] phase transformations and the kinetics of domain growth was studied using TEM in near stoichiometric Ti_3Al . Samples of the Ti_3Al alloy was quenched from the β and from the $\alpha+\beta$ fields and were subsequently annealed for various times at various temperatures in the α_2 phase field to study the kinetics of domain growth. Figures 20 and 21 show the relationship of the various aging times and temperatures on the Ti_3Al samples as a function of the domain-size. They noted that upon quenching the alloy (Ti_3Al) from above the critical temperature of ordering T_c , the microstructure consisted massive martensite with small antiphase domains of average size $8 \times 10^{-3} \mu\text{m}$. On annealing the quenched structures between 700 and 1000°C, domain coalescence occurred, the average domain size growing approximately as the square root of the annealing time.

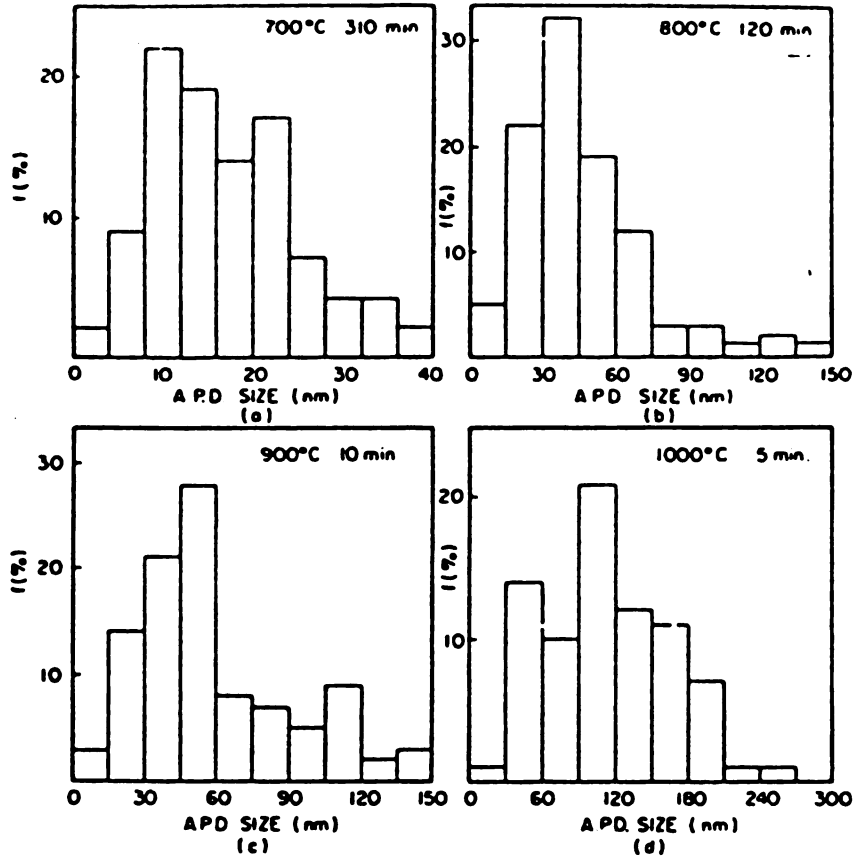


Figure 20. Log-log plot of average domain size vs. time of annealing at different temperatures. [Ref. 43]

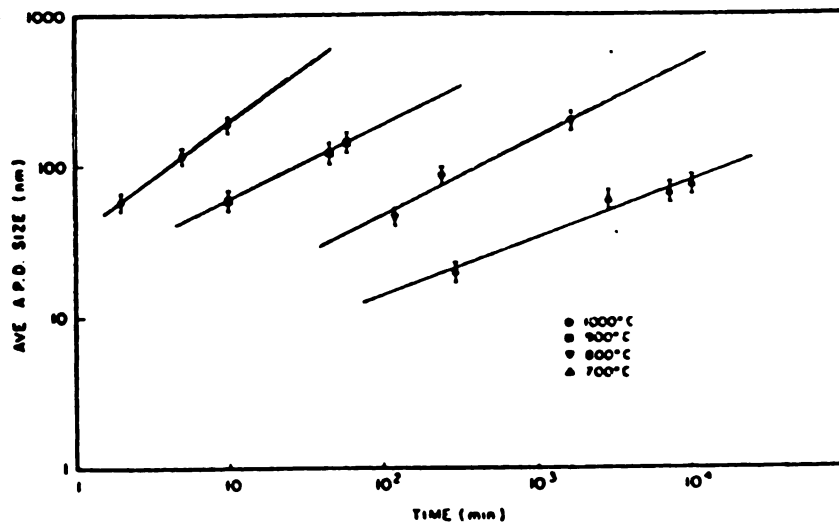


Figure 21. Histograms of APD sizes observed at different temperatures and times for Ti₃Al alloy. [Ref. 43]

The activation energy for the domain growth process was found to be 64.6 ± 6 Kcal/mole ($2.68 \pm 0.25 \times 10^5$ J/mole).

2.5 ORDERED ALLOYS FOR HIGH TEMPERATURE APPLICATIONS

During the mid 60's, intermetallic compounds were the subject of a lot of studies because of the very high strength of these alloys. Since the early 1970's, the pace of work on ordered alloys and intermetallic compounds slackened, as a result of lack of progress in improving either ductility or creep resistance of these otherwise very intriguing alloys.

Interest in utilizing ordered alloys for structural applications was reawakened in this country when researchers at Wright Patterson Air Force Base [Ref. 44] discovered that ductility and strength improvements could be achieved in TiAl and Ti₃Al base alloys using a combination of powder metallurgy and alloying techniques. Finally, several exciting discoveries were reported that permitted substantial ductility to be achieved in cast and wrought ordered alloys previously known to be extremely brittle. The first of these accomplishments involved replacing cobalt in CO₃V with Ni [Ref. 45] and then Iron [Ref. 46], leading to a series of face centered cubic Ll₂-typed superlattices with extensive ductility at ambient temperatures. Shortly after the first reports of this achievement at Oak Ridge National Laboratory (ORNL), it was reported in Japan that polycrystalline Ni₃Al could be made ductile by

adding small quantities of boron [Ref. 47]. Later, this work was confirmed at ORNL [Ref. 48] and General Electric [Ref. 49] and the critical composition range for which boron was effective was identified.

2.5.1 Characteristics of Ordered Alloys

The formation of long range order in alloy system frequently produces a significant effect on mechanical properties, including elastic constants, yield and tensile strengths, strain-hardening rates, ductility and resistance to cyclic or static (creep) deformation [Ref. 50,51,52,53].

At this point it is important to understand why we need these materials and what are these materials expected to stand up to. In designing and operating turbine engines today and in the future, there are two primary problems - both of which demand solutions from the field of materials science. These are the need to operate certain portions of the engine at higher gas and metal temperatures to improve operating efficiency and save fuel. There is also need for lighter-weight materials to decrease engine weight, engine operating stresses due to heavy rotating components, and to increase the operating life of disks, shafts and bearing support structure. These latter materials should not only be less dense than the nickel-base superalloys they are intended to replace, but they are also required to possess roughly the same mechanical properties and oxidation resistance as those materials in current usage. These materials should also be good candidates for primary processing like casting, ingot forging, sheet rolling etc. and for secondary processing like machining, grinding, cutting, welding, superplastic forming, diffusion bonding etc.

Intermetallic compounds are particularly suited to these needs because of two properties which derive from the fact that they possess ordered structures. Modulus retention with temperature in these materials is particularly high because of the strong A-B bonding. In addition, a number of high temperature properties which depend on diffusive mechanisms are improved because of the generally high activation energy required for diffusion in ordered alloy. These properties are static strength retention, creep and fatigue resistance. Finally, in the case of aluminides, the oxidation resistance is particularly good because all of these materials contain a large aluminum reservoir. In many intermetallics the strong A-B bonding also results in low temperature brittleness although the exact mechanism of ductile brittle transition seems to be different in every case. Hence the present challenge is to obtain a mean path whereby the high temperature strength is retained and the low temperature brittleness is greatly reduced.

2.5.2 Dislocations in Ordered Structures

Since an ordinary dislocation moving in a superlattice cannot recreate the crystal structure, disorder in the form of an antiphase boundary (APB) will result from the motion of such dislocation. The additional energy of the APB can be eliminated, however, by motion of dislocations in groups, such that no net change in order occurs behind the dislocations. These groups which consists of two or more dislocations, connected by a strip of APB or other planar fault are known as superlattice dislocations. Within the superlattice dislocation, each unit dislocation may further dissociate into its constituent partial

dislocation (as listed for various superlattices in Table III) [Ref. 53].

It is the motion of the superlattice dislocations and their interaction with each other and with obstacles, such as grain boundaries, precipitate particles or grown-in-antiphase boundaries that control the mechanical behavior of most ordered alloys. Notable exceptions to this behavior are Ni_4Mo [Ref.54], which rarely exhibits superlattice dislocations at room temperature and hypostoichiometric Fe_3Al , which has been suggested to deform by unit dislocations [Ref. 55].

Various workers in the past have dealt with the interesting problem relating strength of ordered alloys with the degree of the order [Ref. 56,57,58,59,60]. These authors however, arrived at different conclusion due to the fact that there is a subtle distinction between two somewhat similar phenomenons, the increase in domain size on prolonged holding below T_c and the increase in the ordering parameter W due to the same heat treatment. This was first pointed out by Ardley [Ref. 61], where the effect of ordering parameter W and the antiphase domain size on the strength of Cu_3Au has been discussed. Firstly as the degree of order within the antiphase domains increases, the room temperature strength decreases. Secondly, as the antiphase domains grow larger, the room temperature strength first increases and then decreases. At the ordering temperature there is appreciable drop in strength as the alloy passes from the ordered to the disordered state. Above the ordering temperature the strength increases with increasing temperature to a maximum value and then decreases again. The temperature at which this maximum occurs depends upon the applied strain rate.

TABLE III
DISLOCATION CONFIGURATIONS IN VARIOUS ORDER ALLOYS

Superlattice type (<i>Strukturbericht</i> designation)	Chemical designation	Unit cell dimensions	Alloy types	Superlattice dislocation type	Burgers vector of each dislocation	Antiphase boundary type
B2	CsCl	a_0	NiAl, AgMg AuZn CuZn, FeCo FeAl, FeRh NiAl, AgMg AuZn		$a_0 \langle 100 \rangle$	None
DO ₃	Fe ₃ Al	a_0	Fe ₃ Al, Fe ₃ Si Fe ₃ B Cu ₃ Au, Ni ₃ Mn Ni ₃ Al, Ni ₃ Fe Cu ₃ Pd, Ni ₃ Ti Ag ₃ Mg, Ni ₃ Ta Ni ₃ Si, Cu ₃ Pt Ni ₃ Ga		$\frac{1}{2}a_0 \langle 111 \rangle$	
L1 ₂	Cu ₃ Au	a_0			$\frac{1}{2}a_0 \langle 112 \rangle$	
DO ₁₉	Mg ₃ Cd	a_0 c_0	Mg ₃ Cd		$\frac{1}{2}a_0 \langle 10\bar{1}0 \rangle$	
L1 ₀	CuAu	a_0 c_0	CuAu, CoPt FePt		$\frac{1}{2}a_0 \langle 112 \rangle$	

2.6 TITANIUM ALUMINIDES

The next table (Table IV) compares the properties of some titanium aluminides with those of conventional titanium and nickel base alloys. The higher aluminum content makes the aluminides somewhat less dense than titanium alloys and appreciably less dense than nickel base superalloys. These compounds are also of potential value because they have high elastic modulus. The most important thing about high modulus is the fact that great many static parts of an engine are sized mainly by the need to minimize elastic deflection under load at the high operating temperatures. Conventional titanium alloys are not stiff enough to be used for many of these applications. Commercial titanium alloys show a modulus that drops rapidly with temperature to a value of 10×10^6 psi at 540°C . TiAl ($L1_0$), on the other hand, shows a higher modulus at 1000°C than titanium does at room temperature [Ref. 62]. Ti_3Al (DO_{19}) shows a higher modulus at 815°C than titanium does at room temperature [Ref. 62].

2.6.1 Deformation Studies on Titanium Aluminides

Early investigations [Ref. 63] showed that many of the super dislocations in TiAl were pinned by an unknown agent. A later study [Ref. 64] showed that the pinning agent became ineffective at about 700°C and the ductility of the compound increased very rapidly above the temperature. An early investigation on Ti_3Al [Ref. 65] showed that the ductility of this compound increased slowly with temperature to 1000°C and electron microscopic examination indicated that the slow increase of

Table IV Properties of High Temperature Alloys

	<u>Ti Base</u>	<u>Ti₃Al</u>	<u>TiAl</u>	<u>Superalloys</u>
Density (g/cm ³)	4.5	4.15-4.7	3.76	8.3
Young's Modulus (GN/m ²)	110-96	145-110	176	206
Max. Temp. - Creep (°C)	538	815	1038	1093
Max. Temp. - Oxidation (°C)	593	649	1038	1093
Ductility - R.T. (%)	~ 20	2-5	1-2	3-5
Ductility - Operating (%)	High	5-8	7-12	10-20

the ductility was due to the appearance of an increasing density of "c + a" dislocations instead of only the "c" dislocations present earlier.

The deformation substructure of TiAl contains two types of dislocations [Ref. 63,66]. One type, the $a/2[110]$, does not disorder the lattice and is free to move as a unit dislocation. The other two types, the $a/2[011]$ and $a/2[101]$, disorder the superlattice and is therefore expected to move in pairs as super dislocations. Shechtman, Blackburn and Lipsitt [Ref. 63] observed these dislocations. However there was an unexpectedly small proportion of super dislocations were observed. A ductile brittle transition was observed to be 700°C. The dominant mode of fracture beyond this temperature was mostly ductile in nature.

Lipsitt, Shechtman and Schafrik [Ref. 65] also studied the relationship between the mechanical behavior, the dislocation activity, and the fracture mode of Ti_3Al as a function of temperature to 900°C. The major mode of deformation in this material was shown to be the motion of $a'\langle 11\bar{2}0 \rangle$ dislocations on the prism, basal and pyramidal planes. The highest density of dislocations was on the prism planes because such movement produced no wrong first nearest neighbors. The incidence of $a'/3\langle 11\bar{2}3 \rangle$ dislocations remained low upto 900°C, the limit of this study. Twinning was not observed, although microtwins formed at 900°C. Intergranular cracking began above 600°C and increased with increasing temperature giving rise to an apparent ductile brittle transition. Some dislocation cross-slipping began above 600°C. Fractographic analysis indicated that below 600°C failure occurred entirely by cleavage. Above 600°C, increasing amounts of ductile rupture occurred, but even at 900°C

substantial cleavage existed. No evidence of disordering was observed upto 900°C in the Ti_3Al used in this study.

Yang [Ref. 67] reported that both "c" and "c+a" dislocations could be identified in Ti_3Al deformed under specific conditions. The "c + a" dislocations were of two varieties, " $c + 1/2 \langle a' \rangle$ " and " $2c + \langle a' \rangle$ ", the presence of which depended on the temperature and strain rate at which the specimen had been deformed.

Sastry and Lipsitt [Ref. 68] studied the influence of a small amount of Nb addition on the microstructure and properties of Ti_3Al . The results indicated that the ordering transformation in Ti_3Al proceeds by the nucleation and growth of small ordered domains and the subsequent growth of those domains with an activation energy of about 269 KJ/mole. The addition of Nb slowed the domain growth kinetics. The small Nb addition also increased the strength and ductility of a recrystallized martensitic structure. This result was due to the Nb increasing the non-basal slip activity. A few years later, Martin, Lipsitt, Nuhfer, and Williams [Ref. 69] reported on a similar study in some slightly more complex alloys. In a $Ti_3Al + Nb + W$ alloy it was seen that the size of the martensite platelets was reduced by the alloying additions and that the concomitant result was a precipitation of a fine b.c.c beta phase which may have added slip dispersal in these alloys. The addition of W to $TiAl$ resulted in a marked strength increase, although there was no accompanying ductility increase. The W addition was shown to refine the microstructure, reduce the slip length, and provide a small degree of solid solution strengthening. Again some b.c.c beta phase precipitation was also observed.

Schafrik [Ref. 62] measured the elastic moduli of TiAl, Ti₃Al and Ti₃Al-Nb to 940°C. He showed that the moduli of all the materials decreased slowly and linearly with temperature. The effect of the Nb addition to Ti₃Al was to decrease the room temperature modulus of the alloy by about 10%, but also to slow the rate of modulus decrease with temperature such that the moduli of the two materials was nearly the same at the maximum temperature of the study.

2.7 THE QUASI CHEMICAL MODEL OF SOLID SOLUTIONS

The quasi chemical model of solutions is applied to solutions of components which are considered to have equal molar volumes in the pure state and which have zero volume change on mixing. Furthermore, the interatomic forces are only significant over short distances, such that only nearest neighbor interactions need be considered. The energy of the solution is thus calculated by summing the atom-atom bond energies.

Let us consider one mole of a crystal containing N_A atoms of A and N_B atoms of B such that :

$$X_A = \frac{N_A}{N_A + N_B} = \frac{N_A}{A} \quad \text{and} \quad X_B = \frac{N_B}{A} \quad \dots \dots (2.1)$$

where A is the Avogadro number, X_A is the mole fraction of A atoms and X_B is the mole fraction of B atoms. This solution would contain three types of atomic bonds:

1. A-A bonds, the energy of which is V_{AA}
2. B-B bonds, the energy of which is V_{BB}

3. A-B bonds, the energy of which is V_{AB} .

By considering the zero of energy as being that when the atoms are infinitely far apart, V_{AA} , V_{BB} and V_{AB} are negative quantities. Let Z be the coordination number of an atom in the crystal, i.e., each atom has Z nearest neighbors. If, in the solution, there are N_{AA} A-A bonds, N_{BB} B-B bonds and N_{AB} A-B bonds, then the energy of the solution, E , is obtained as a sum of these bond energies:

$$E = N_{AA}V_{AA} + N_{BB}V_{BB} + N_{AB}V_{AB} \dots \dots \dots (2.2)$$

(The number of A atoms) \times (the number of bonds per atom)

= (the number of A-B bonds) + (the number of A-A bonds \times 2)

The factor 2 in the above equation arises from the fact that each A-A bond involves 2A atoms).

$$\text{Thus, } N_A Z = N_{AB} + 2N_{AA}$$

$$\text{i.e., } N_{AA} = (N_A Z)/2 - (N_{AB})/2 \dots \dots \dots (2.3)$$

Similarly,

$$N_B Z = (N_B Z)/2 - (N_{AB})/2 \dots \dots \dots (2.4)$$

Substituting equations (2.3) and (2.4) in equation (2.2), we have,

$$E = \{(N_A Z)/2 - (N_{AB})/2\}V_{AA} + \{(N_B Z)/2 - (N_{AB})/2\}V_{BB} + N_{AB}V_{AB}$$

$$= (ZN_A V_{AA})/2 + (ZN_B V_{BB})/2 + N_{AB}\{V_{AB} - (V_{AA} + V_{BB})/2\} \dots \dots \dots (2.5)$$

Let us now consider the situation when the components are not mixed.

The number of A-A bonds $\times 2$ = the number of A atoms \times the number of bonds per atom.

$$\text{i.e., } N_{AA} = (N_A Z)/2$$

$$\text{Similarly, } N_{BB} = (N_B Z)/2$$

ΔE^M = change of internal energy on mixing

= (the energy of the solution) - (the energy of the unmixed components)

$$= [(Z N_A V_{AA})/2 + (Z N_B V_{BB})/2 + N_{AB}(V_{AB} - (V_{AA} + V_{BB})/2)] -$$

$$[(Z N_A V_{AA})/2 + (Z N_B V_{BB})/2]$$

$$= N_{AB}(V_{AB} - (V_{AA} + V_{BB})/2)$$

$$= (1/2)N_{AB}\{2V_{AB} - (V_{AA} + V_{BB})\} = (1/2)N_{AB}V^*$$

$$\text{where } V^* = \{2V_{AB} - (V_{AA} + V_{BB})\}$$

We know from thermodynamic formulation that:

$$\Delta H^M = \Delta E^M - P\Delta\bar{V}^M,$$

where $\Delta\bar{V}^M$ = volume change on mixing and ΔH^M = enthalpy change on mixing.

For a quasi chemical process the stipulation is $\Delta\bar{V}^M = 0$, hence, $\Delta H^M = \Delta E^M$,

Therefore, $\Delta H^M = \Delta E^M = N_{AB}V^*/2$

This equation indicates that for known values of V_{AA} , V_{BB} and V_{AB} ; ΔH^M is very much dependent on the number of A-B bonds.

We also know that under ideal conditions, $\Delta H^M = 0$. This means that it is not necessary for $V_{AA} = V_{BB} = V_{AB}$ for ideal solutions, but it is sufficient if $2V_{AB} = V_{AA} + V_{BB}$, that is $V^* = 0$.

If $|2V_{AB}| > |(V_{AA} + V_{BB})|$, then ΔH^M is a negative quantity, corresponding to negative deviation from Raoultian ideal behavior.

The inequality on the previous paragraph means that the V_{AB} bonds are very strong compared to V_{AA} and V_{BB} and thus unlike nearest neighbor are preferred when ΔH^M (enthalpy of mixing) is negative.

CHAPTER 3

EXPERIMENTAL PROCEDURES AND TECHNIQUES

3.1 SELECTION OF HEAT TREATMENT CONDITIONS

Preliminary heat treatment and testing indicated that for the sample sizes involved (for DSC/DTA, electron microscopy and x-ray diffraction) a holding time of 30 minutes was adequate to homogenize the samples at 1200°C in the β single phase region. However, longer annealing times were chosen to ensure equilibrium at lower temperatures of holding also. Since titanium aluminum samples are extremely reactive, they were always heat treated in vacuum encapsulated quartz tubes.

3.2 HEAT TREATMENT PROCEDURE

Samples for this study were obtained by vacuum arc melting (courtesy of RMI company) in the form of buttons. Chemical composition of samples used in the experiments are as follows: (1) Ti-6Al (≈ 10 at.% Al), (2) Ti-8Al (≈ 13 at.% Al), (3) Ti-10Al (≈ 16.5 at.% Al), (4) Ti-12Al (≈ 19 at.% Al), (5) Ti-14Al (≈ 22.5 at.% Al), (6) Ti-16Al (≈ 25 at.% Al). Samples were initially cut to different sizes depending on the experiment to be used for and then vacuum-encapsulated in quartz tubes. Then the samples were annealed at different temperatures and times depending on the nature of investigation.

Vacuum encapsulated samples were annealed at 1200°C for one hour and then quenched in water at room temperature. Some of these quenched samples were then used to perform DSC/DTA studies, x-ray diffraction and electron microscopic studies. Some of these quenched samples were then aged at various temperatures ranging from 500°C to 1000°C (i.e., in the α_2 phase field, Ref. 19) for various lengths of time. These aged samples of various compositions were then used for different types of studies depending on the design of the experiments. The heat treatment schedule followed for the Ti-Al alloys is shown schematically in Figure 22.

3.3 ANALYSIS OF HEAT TREATED SAMPLES

3.3.1 Differential Thermal Analysis

In a broad sense, DTA is the measurement of changes in thermochemical properties of materials as a function of temperature. It provides the observation of a change in energy of the sample materials associated with the phase transformation which is temperature-dependent. The sample reacts endothermically (heat-absorption) or exothermically (heat-release) during phase transition. This energy release is then compared to the null response of a reference sample (usually platinum or alumina, which does not have a phase change in the temperature range of the experimentation, but whose thermal mass is comparable to the sample being tested). The difference in heat liberated between the sample and reference is then plotted with respect to the testing temperature.

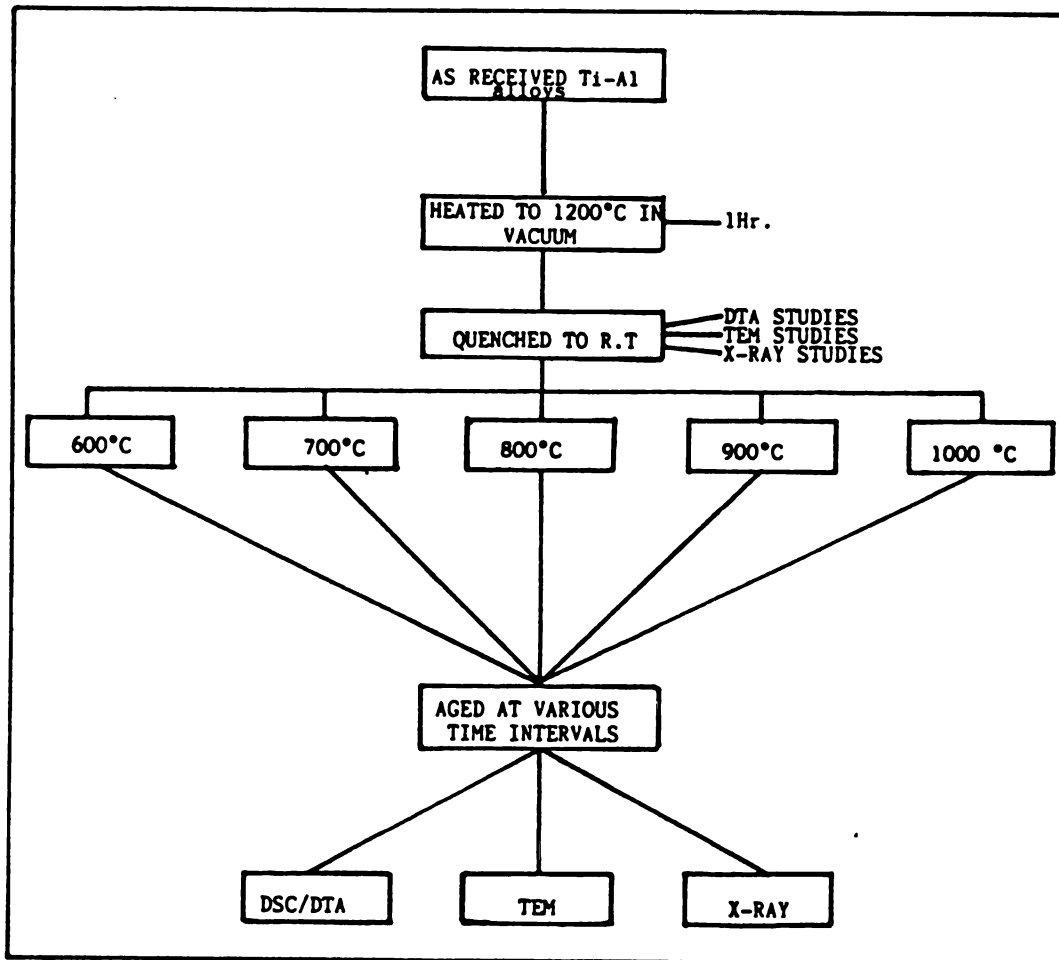


Figure 22. Heat treatment schedule for Ti-Al alloys.

The differential thermal analyzer used in the study is a DuPont Model 990 High Temperature DTA analyzer. Basic features in this instrument include a 1200°C furnace for heating the samples and a derivative function for determining the rate of temperature change with respect to time, $d(\Delta T)/dt$. An X-Y recorder plots the heat output versus the testing temperature. The instrument's differential mode provides the nature of the transition temperature region, and the derivative function gives the temperature at which the transition is completed by indicating a peak at the point of inflection of the differential curve. In order to clearly obtain the accurate transition point from the derivative trace, the heating rate was determined to be 20°C/minute.

Major elements included in the differential thermal analyzer for DTA experiments performed in this investigation are: 1200°C furnace, sample holders for the titanium sample and the thermal reference (platinum wire), heating sources for the holders, a precision thermocouple for each holder, argon atmosphere into the holders, and a controller-programmer for controlling the heating and the cooling as well as processing the thermocouple voltage and the input heat data into a meaningful form. The voltage difference between the sample thermocouple and the reference is presented on the X-Y recorder as the dependent variable against temperature.

Instrument setup and sample analysis procedures were as follows: The instrument was warmed up for 10-15 minutes. The proper thermocouple heights and the appropriate position of the ceramic tubes were set. The starting temperature was then set to about 500°C and the limit temperature was set to 1200°C. The recorder paper was then set at the correct position and then both the sample and the reference were put in the respective cups carefully. Dry argon gas was then passed through

the ceramic tube for some time at about 80 ml./minute. Then the sample (size about 70-100 mg.) was heated at the programmed rate of 20°C/minute and the data recorded.

Other procedures that were required to ensure the accurate measurement of the transition temperatures were: changing the platinum foil liners when they appear to be oxidized or coated, calibrating the thermocouples regularly and periodically applying a small amount of "Anti Seize compound" to the joint of the bell-jar and the furnace tube and cap to prevent seizing.

3.3.2 X-Ray Diffractometry

The heat treated samples were cut to a proper size to fit the specimen holder. Since the grain sizes of the samples used in this study were very large (and since it is intended to detect the presence of extremely weak superlattice spots) a method was adopted to expose more grains to the x-ray beam. The sample was rotated about a horizontal axis such that the sample plane remained tangent to the focussing circle and the center of the sample remained at the center of the diffractometer circle. Before obtaining x-ray diffraction patterns, the samples were polished with a 600 grit abrasive paper and then lightly etched to remove any distorted layer on the surface of the specimen. A General Electric XRD-5 x-ray diffractometer was used with a copper tube and nickel filter so that the ensuing x-ray beam was mainly CuK_{α} .

3.3.3 Electron Microscopy

A Hitachi H-800 200KV electron microscope along with a double tilt specimen holding stage (+40° to -40°) was used. The heat treated samples were initially cut into thin wafers by a diamond wafering machine. Then the samples were mechanically polished to a thickness of 0.15 mm by abrasive papers. The samples were then cut into small 3mm. discs using metal shears. A Struers Tenupol Twin Jet polisher was used to thin down the samples prior to examination under the electron microscope. The twin jet polisher is equipped with a light sensing circuitry so as to cut off the thinning process as soon as the hole is formed. The polishing conditions are given below:

Starting thickness 0.15mm.

600 mls. Methyl Alcohol

60 mls. Perchloric Acid

360 mls. Ethylene Glycol Monobutyl Ether

V = 30V ; Temperature = -10 to -15°C.

CHAPTER 4

RESULTS AND DISCUSSION

4.1 SCOPE OF THE PRESENT STUDY

The question "What role does the α_2 phase (ordered) play in Ti-Al alloys?", is of technological importance. This ordered phase also occurs in many complex titanium alloys containing aluminum. For example, α_2 phase was detected in a special alloy, Ti-6Al-2Nb-1Ta-0.8Mo (Ti-6211), developed by the Naval Ship Systems Research Laboratory. It was felt that this α_2 phase had a significant influence on mechanical properties such as ductility etc. in this new alloy. Thus, a set of experiments were conducted at Michigan State University [Ref. 70, 71] in order to answer some of the questions. Concurrently, some work by Shull et. al. [Ref. 24, 30] led to the belief that $\alpha \rightarrow \alpha_2$ transformation was detectable by DTA measurements in this system. Hence some DTA work was performed on a series of binary Ti-Al alloys to obtain some qualitative and quantitative data on this order-disorder transformation. As a further result of the present study a new equilibrium phase diagram of the Ti-rich end of the Ti-Al system is proposed. This diagram is compared with the ones proposed by other workers in this field [Ref. 18, 19].

X-ray diffraction study, although useful for phase identification, poses a difficulty in resolving superlattice reflection

in this system, specially for a polycrystalline large grain sample. Thus much of the structural information must be obtained by electron diffraction.

Transmission electron microscopy has also been done in order to further characterize this transformation. A detailed domain growth study has been conducted in order to understand the domain growth kinetics. The domain growth rate has been correlated to the microhardness response in this system. Careful, detailed electron microscopy was also done in order to illustrate the anisotropic nature of the Anti Phase Boundary (APB) energy.

Finally, an attempt has been made to examine the disordering kinetics of this transformation by utilizing Bragg William approximation of order-disorder reaction.

4.2 DTA RESULTS

Fig. 23 shows a typical DTA trace for a Ti-16Al(≈25 at% Al) alloy which was heated to 1200°C and water quenched. In this figure we observe one exothermic and two endothermic events during the heating cycle. There is nothing in the existing phase diagram of the Ti-Al system, which suggests such an exothermic reaction in the observed temperature range of 600 to 800°C for this alloy composition. This event (which starts at about 617°C) is due to the formation of α_2 back to the disordered α (hcp) and the second endothermic peak corresponds to the transformation of α to β (bcc). The next figure (Figure 24) shows the effect of heating rate on Ti-16 wt.% Al(≈25at% Al) on these

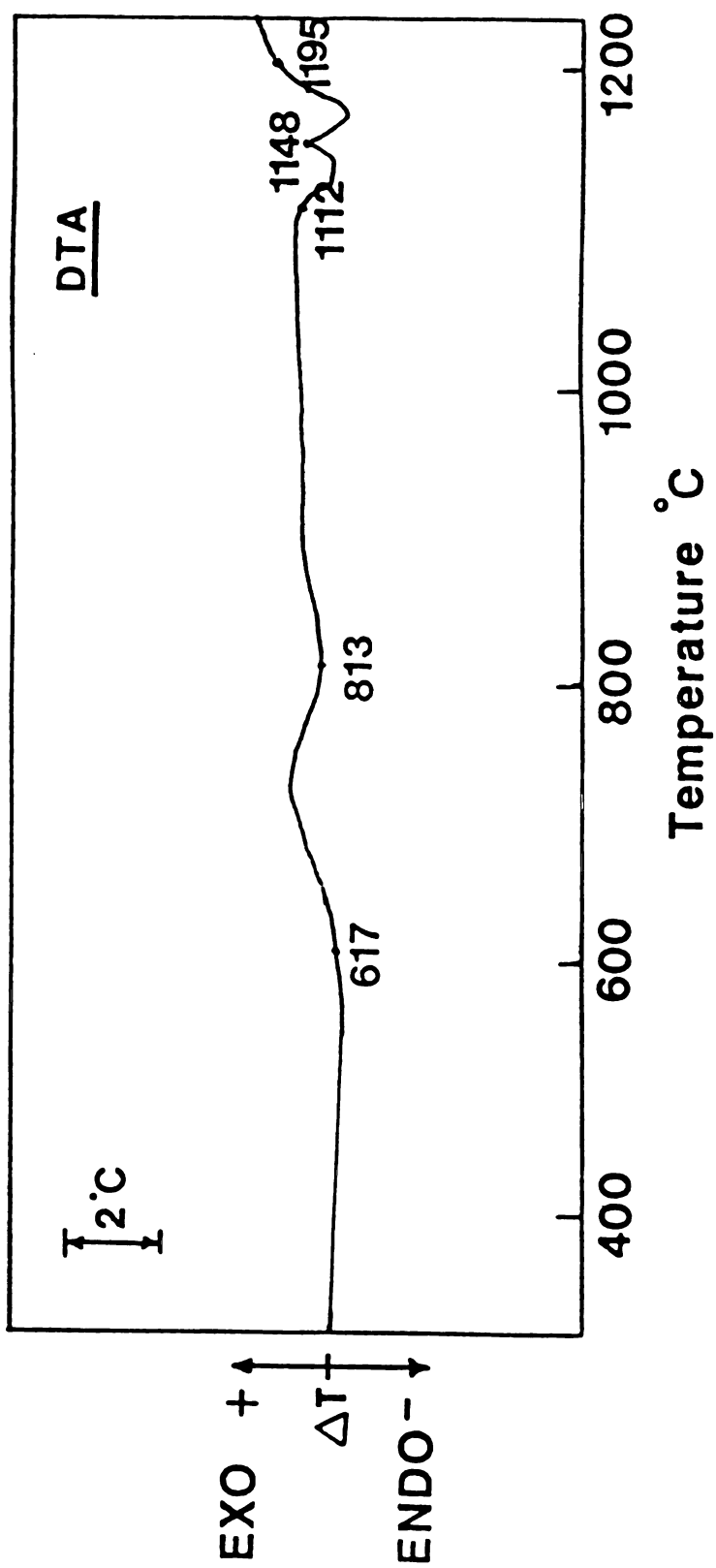


Figure 23. DTA data determined from Ti-16Al (≈ 25 at.% Al) alloy sample quenched from 1200°C. Heating rate was 20°C/min.

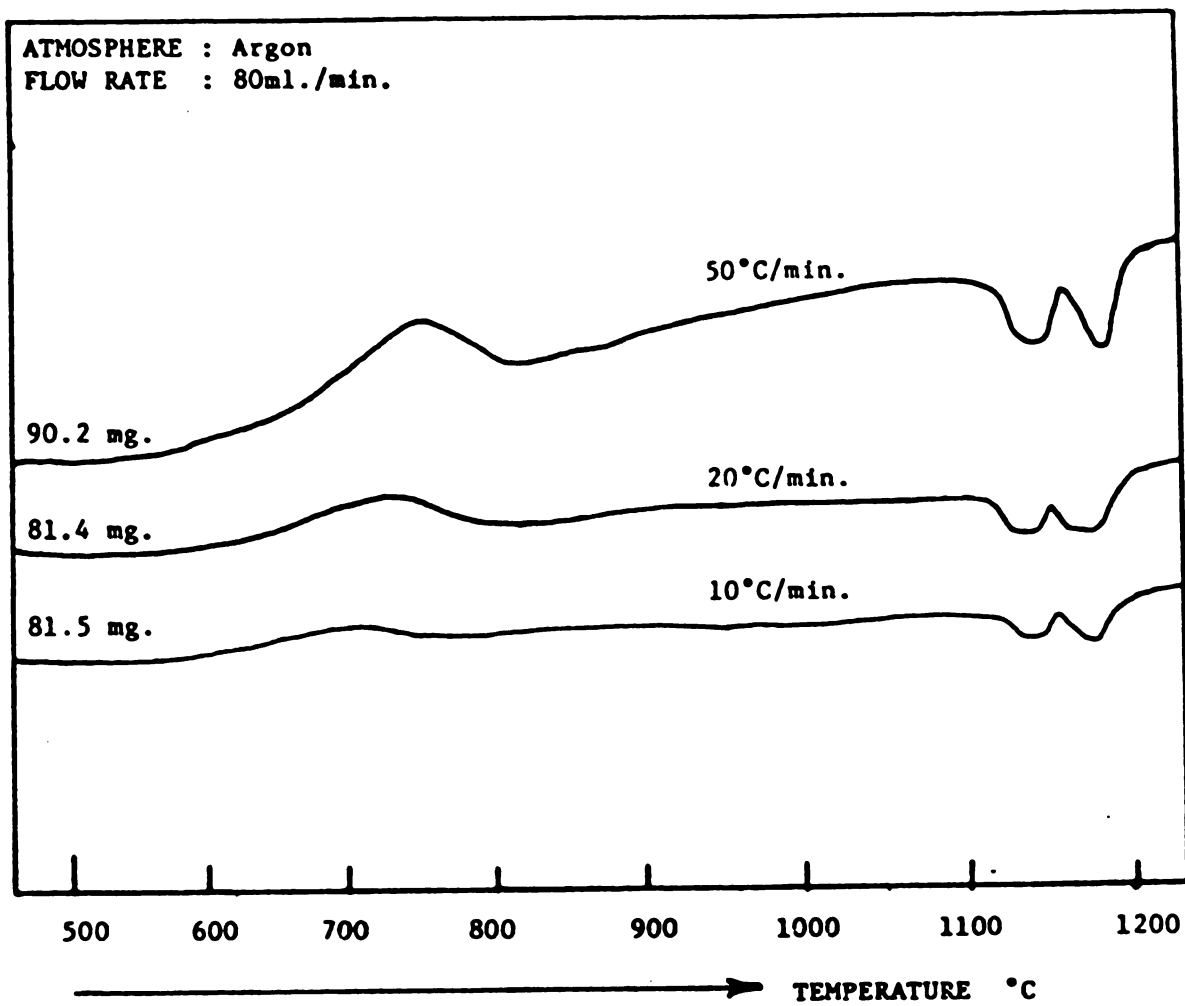


Figure 24. Heating rate dependence of the order-disorder phenomenon in Ti-Al system.

transformations. The transformation peaks are more pronounced at higher heating rates. Similar behavior has also been observed in Ti-14Al(≈ 22.5 at% Al) and Ti-12Al(≈ 19 at% Al) samples. This pattern can be seen in Figure 25, which is a composite DTA pattern of a series of alloys starting from Ti-6Al(≈ 10 at% Al) through Ti-16Al(≈ 25 at% Al). All of these samples (Figure 25) were initially annealed at 1200°C for 1 hour and water quenched to room temperature. Figure 25 shows that there is still a shift of the $\alpha \rightarrow \alpha_2$ transformation temperature to higher values with increasing aluminum content. Similarly, the temperature for $\alpha \rightarrow \alpha_2$ transformation increases with increasing aluminum content. These reactions are not observed for alloys with lower aluminum contents i.e. Ti-6Al (≈ 10 at% Al), Ti-8Al (≈ 13 at% Al) and Ti-10Al (≈ 16.5 at% Al). Fig. 26 illustrates the effect of aging on the Ti-16Al(≈ 25 at% Al) alloy. Samples were initially quenched from 1200°C and then aged at various temperatures for a fixed time and cooled to the ambient temperature. Subsequently DTA measurements were conducted. A sample, aged at 800°C and then subjected to a DTA analysis, did not reveal the initial exothermic peak. It is believed that aging at 800°C completed the $\alpha \rightarrow \alpha_2$ transformation and thus no further calorimetric effects are observed. However, 500°C is not high enough an aging temperature for reordering of the metastable α -phase quenched in from 1200°C i.e: this reaction kinetics is extremely sluggish at about 500°C .

Based on the above mentioned experimentation, and prior work by other authors, a Ti-Al phase diagram up to 25 at% Al can be plotted as shown in Figure 27. Phase boundaries as determined from DTA experiments are indicated by full circles on this diagram. The dotted lines (marked 1 and 2) in this diagram delineate the region within which the quenched

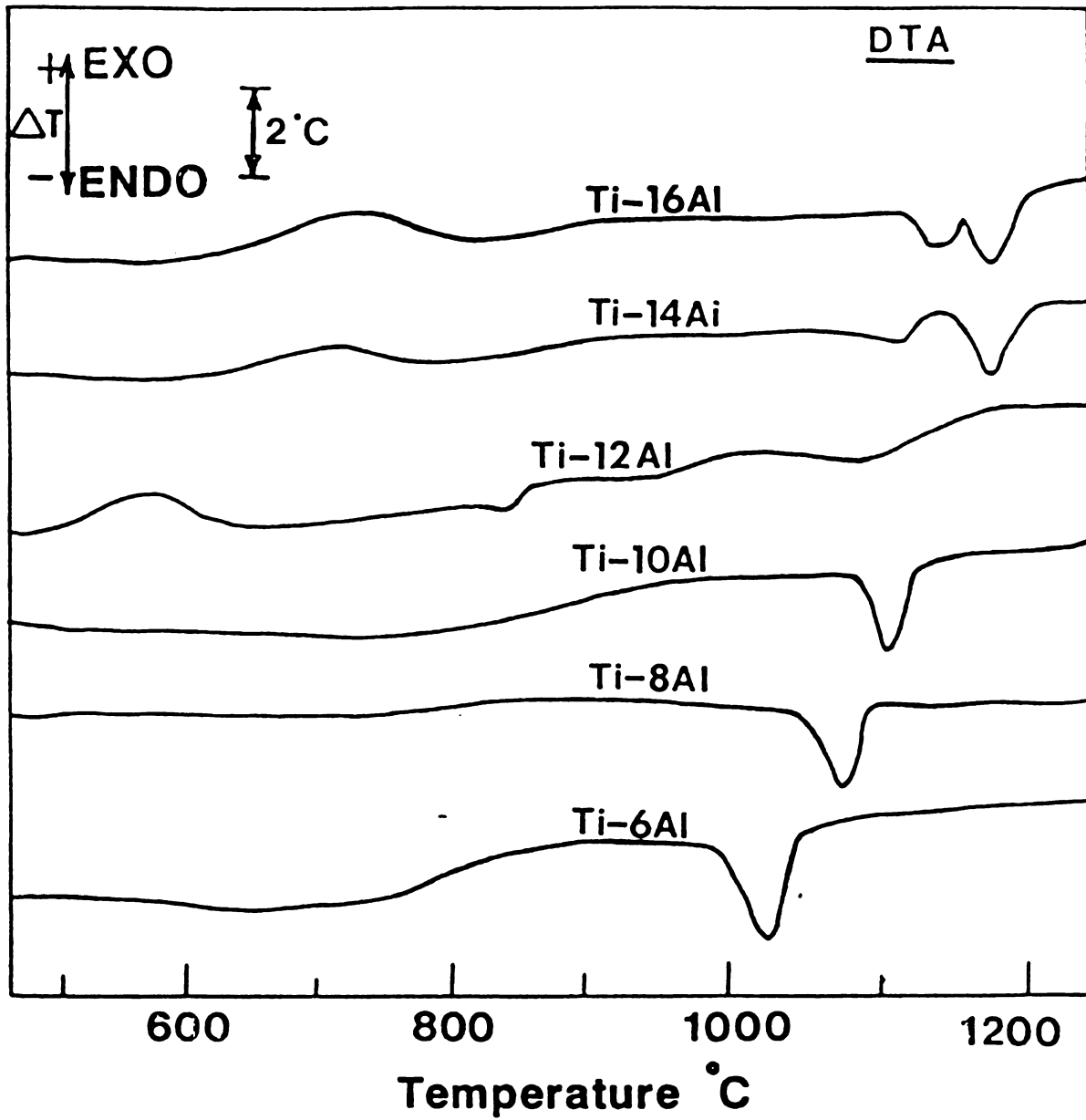


Figure 25. Series of DTA data obtained from as quenched (from 1200°C) samples starting from Ti-16 Al (≈ 25 at.% Al) to Ti-6Al (≈ 10 at.% Al). Heating rate was 20°C/minute.

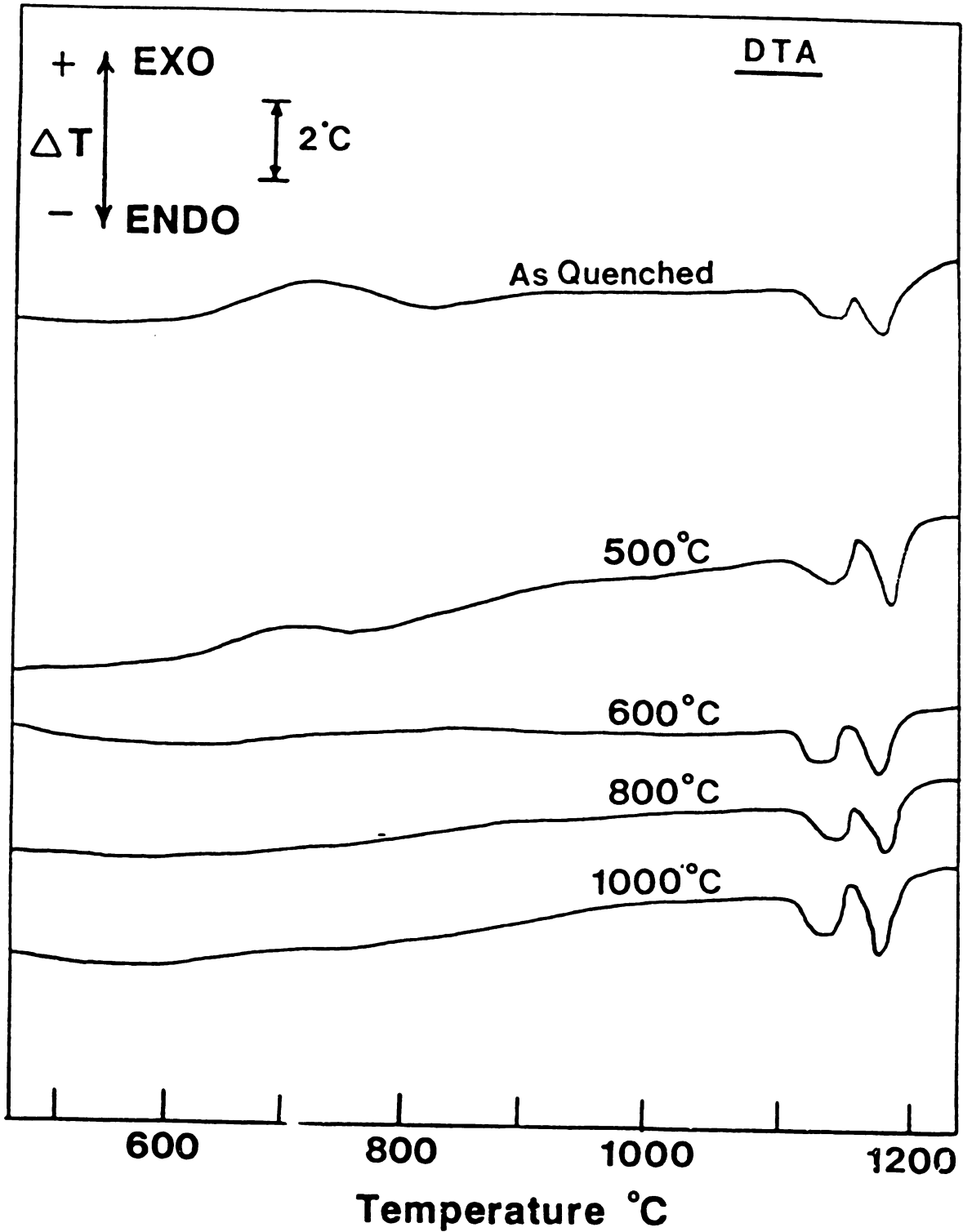


Figure 26. Series of DTA data obtained from Ti-16Al (≈ 25 at.% Al) alloy samples which were either quenched or quenched and aged at the various temperatures that are indicated in the diagram.

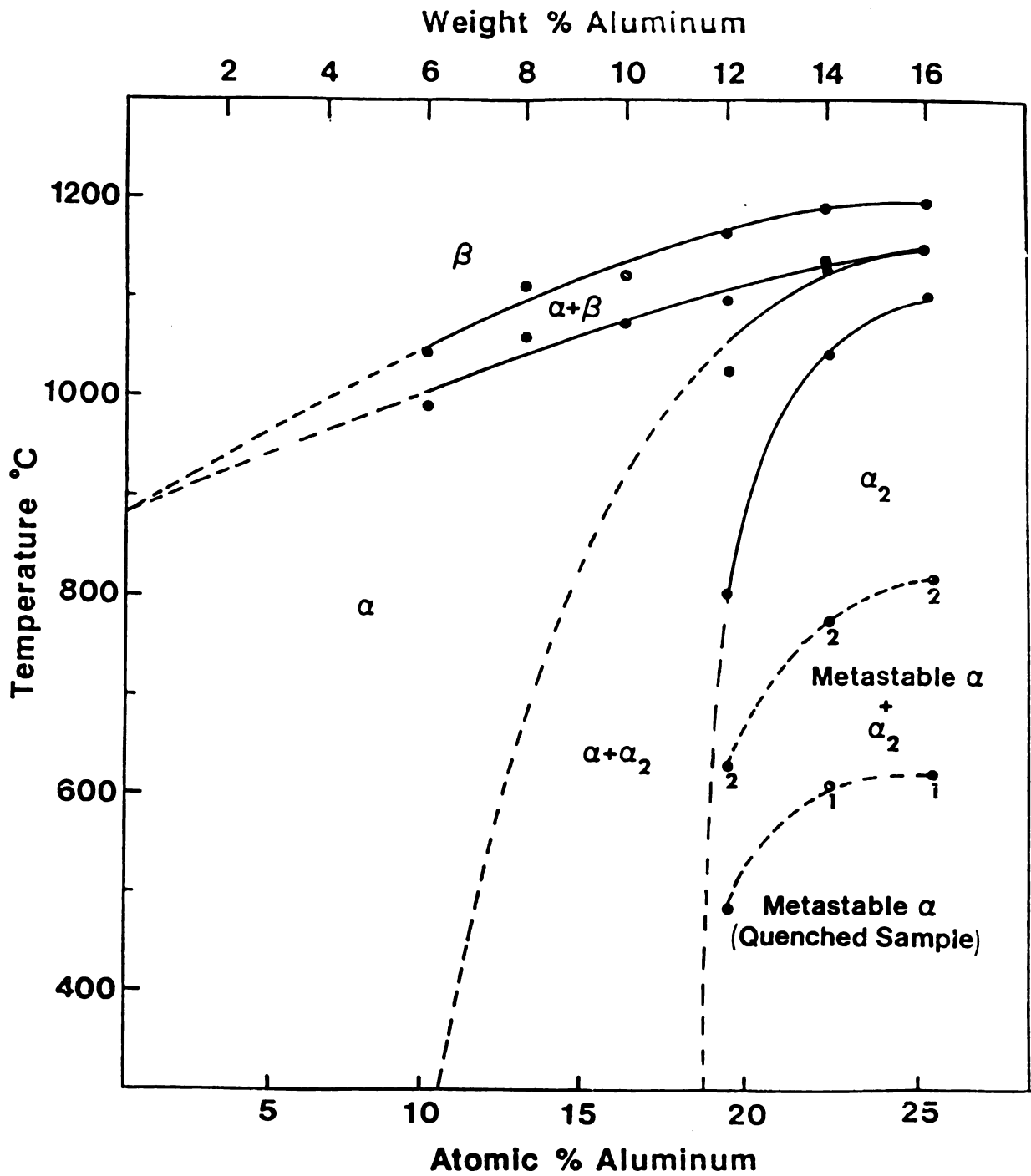


Figure 27. Proposed phase diagram (Mukherjee and Sircar) of the titanium rich end of the Ti-Al system. The full circles indicate the experimentally obtained phase boundaries.

in α -phase is converted to the equilibrium ordered α_2 phase. When compared with the other phase diagrams available, it can be seen that this phase diagram is seen to resemble the one proposed by Blackburn [Ref. 19] but is in sharp contrast to the one proposed by Crossley [Ref. 18]. However, this proposed phase diagram is shifted to higher temperatures and higher aluminum contents as compared with that of Blackburn's.

From the proposed phase diagram, it can be seen that in quenched samples, one can have various amounts of metastable α phase depending on the quenching rate and alloy composition. The amount of α_2 phase formed during quenching from 1200°C will also depend on the alloy composition and cooling rate. It appears that the kinetics of reordering of the quenched phase is faster in Ti-12Al (≈ 19 at% Al) alloy than in Ti-16Al (≈ 25 at% Al) alloy. In the absence of detailed morphological and microscopic (TEM) analysis, an explanation for this observed relative stability of the quenched α phase cannot be provided. However, some conjectures could be made, aimed at understanding this behavior.

There are two possible types of defect structures leading to an ordered sublattice in non-stoichiometric compositions: either preferential sublattice vacancies or antistructure defects. Therefore, the ordering kinetics is influenced by a correlated atomic diffusion. The atomic diffusion, on the other hand, is facilitated by the presence of equilibrium or non-equilibrium number of vacancies. Further, the atomic mobility is also related to the migration energy, E_m , of vacancies.

It can be argued that, compared with dilute solid solutions, it is more difficult to form vacancies in concentrated solid solutions

because the number of Ti-Al bonds increases with increasing concentration of aluminum and since it is known (from the tendency to order) that the Ti-Al bond is stronger. Thus, on the average, the energy required for the formation (E_f) increases with increasing concentration of this alloy. The migration energy, E_m , is also higher for more concentrated solid solutions. This behavior is because the diffusing atom encounters a steeper energy barrier between the neighboring saddle points. In dilute solutions, however, the formation and migration of vacancies require less energy because of the lesser number of available Ti-Al bonds. If vacancies are present, then the diffusional process, which is the mode of ordering in Ti-Al system, can become faster by vacancy migration. Hence, the kinetics of ordering in off-stoichiometric composition is faster than for stoichiometric ones and the ordering could proceed at lower temperatures as indicated by DTA experiments.

Preliminary X-ray diffraction studies on Ti-16Al(≈25 at% Al) samples, support the results obtained by DSC/DTA studies. For example, a Ti-16Al(≈25 at% Al) sample upon quenching from 1200°C, does not show any superlattice reflection. But when this quenched sample is aged at 1000°C for 4 hours, superlattice reflections corresponding to the DO_{19} structure are observed as shown in the next figure (Figure 28). The aged sample shows very weak superlattice reflections from $(10\bar{1}1)\alpha_2$ and $(10\bar{2}0)\alpha_2$. It must be pointed out that except for these two superlattice reflections, all others are extremely weak. Aside from the fact that in Ti-Al system the ratio of intensity of superlattice to fundamental reflection is very small, this problem could also be attributed to large

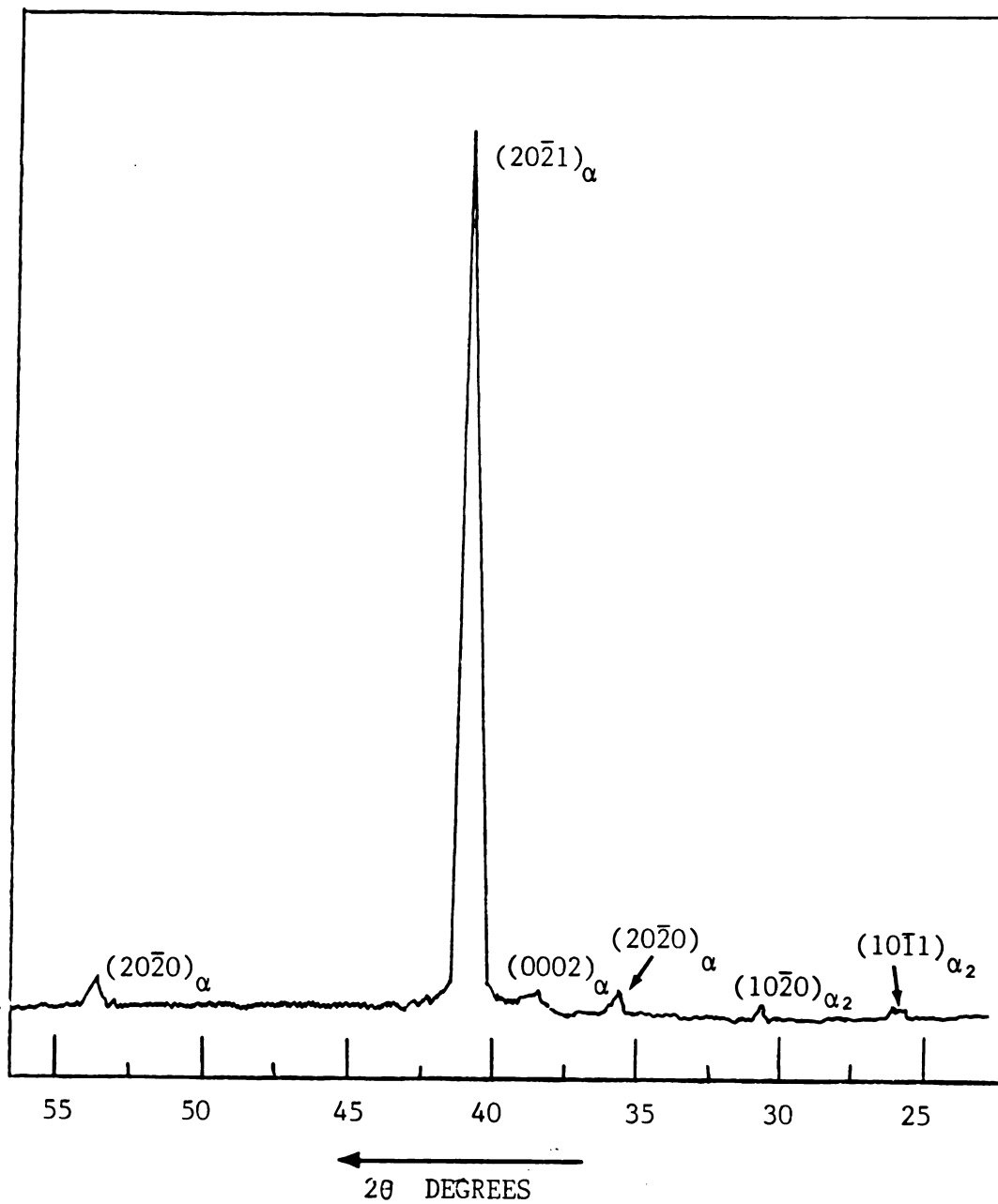


Figure 28. X-ray diffraction pattern obtained from an ordered sample of Ti-16Al (≈ 25 at.% Al). (Please note that the superlattice reflections, indicated by the α_2 symbol, are very weak.)

grain size and texture of the sample. The superlattice reflections could only be observed after the sample was rotated as explained in the "experimental techniques" part of this thesis.

4.3 TEM RESULTS

In order to understand the TEM results and also to image the ordered domains in this system, structure factor and extinction rules for DO_{19} crystal structural have been undertaken.

4.3.1 Structure Factor Determination for the DO_{19} Crystal Structure

Consider the unit cell of the DO_{19} crystal structure as shown in Figure 1. The atomic positions of Al and Ti atoms in the unit cell are listed below.

Al $(0,0,0)$, $(1/3,2/3,1/2)$

Ti $(1/2,0,0)$, $(0,1/2,0)$, $(1/2,1/2,0)$

$(1/3,1/6,1/2)$, $(5/6,1/6,1/2)$, $(5/6,2/3,1/2)$

The crystal structure of DO_{19} can also be looked upon as an ABABAB type of stacking, where A corresponds to layer 1 and B corresponds to layer 2. Layer B is displaced by vector $(1/3,2/3,1/2)$ with respect to layer A. The third layer occupies the same position as the that of layer 1. There are four atoms / layer. Hence, to describe the DO_{19} unit cell we need 8 atoms.

According to the diffraction theory, the structure factor of the crystal is expressed as,

$$F_g = \sum f_i \exp(2\pi i \mathbf{g} \cdot \mathbf{r}_i),$$

where f_i is the atomic scattering factor of the i -th atom in the real lattice unit cell. The vector \mathbf{r}_i is expressed by,

$$\mathbf{r}_i = u_i \mathbf{a} + v_i \mathbf{b} + w_i \mathbf{c}$$

where, u_i , v_i and w_i are the fractional coordinates of the i -th atom, and \mathbf{a} , \mathbf{b} and \mathbf{c} are the translations of the real lattice unit cell.

If \mathbf{a}^* , \mathbf{b}^* and \mathbf{c}^* are the translations of the reciprocal lattice unit cell, every reciprocal lattice point can be expressed by the form

$$\mathbf{g} = h\mathbf{a}^* + k\mathbf{b}^* + l\mathbf{c}^*$$

where, h , k and l are integers. \mathbf{g} is the normal to the crystal plane with Miller indices h k l . Thus, $\mathbf{g} \cdot \mathbf{r}_i$ is obtained as,

$$\mathbf{g} \cdot \mathbf{r}_i = hu_i + kv_i + lw_i$$

The structure factor for layered structures like DO_{19} can be obtained by the simple sum of the structure factor related with each layer.

$$F_g = F_1 + F_2$$

$$F_1 = f_{Al} e^0 + f_{Ti} \left\{ e^{-2\pi i(h/2)} + e^{-2\pi i(k/2)} + e^{-2\pi i((h+k)/2)} \right\}$$

$$F_2 = f_{Al} + f_{Ti} \left\{ e^{-\pi i h} + e^{-\pi i k} + e^{-\pi i(h+k)} \right\}$$

$$F_2 = F_1 e^{-2\pi i(h/3 + 2k/3 + 1/2)}$$

where F_1 - structure factor of the first (001) plane in the unit cell shown in Figure 1.

F_2 - structure factor on the second (parallel) (001) plane.

Multiplication by the complex conjugate of F_g will give the square of the absolute value of the resultant wave amplitude F , that is,

$$\begin{aligned} |F|^2 &= 4 \cos^2 \pi((h+2k)/3 + 1/2) \\ &\times \left\{ f_{Al} + f_{Ti} (e^{-\pi i h} + e^{-\pi i k} + e^{-\pi i (h+k)}) \right\} \\ &\times \left\{ f_{Al} + f_{Ti} (e^{\pi i h} + e^{\pi i k} + e^{\pi i (h+k)}) \right\} \end{aligned}$$

According to the diffraction theory, $|F|^2$ is proportional to the intensity I_g of the reciprocal lattice points, that is,

$$I_g \propto |F_g|^2$$

$|F|^2$ obtained from the above equation are summarized in Table V, and the resulting reciprocal lattice planes are illustrated in Figures 30 and 31.

We know, in the case of a h.c.p crystal structure

$$\mathbf{a}_1^* = ((\mathbf{a}_2 \times \mathbf{c}) / V_c)$$

$$\mathbf{a}_2^* = (\mathbf{c} \times \mathbf{a}_1) / V_c$$

76
TABLE V

Condition I	Condition II	Condition III	Structure Factor	symbol used in figures 30, 31
1 = 2g	h + 2k = 3p	h - even k - even	$I \propto 4 (f_{Al} + 3f_{Ti})^2$	● F
		h - even k - odd	$I \propto 4 (f_{Al} - f_{Ti})^2$	○ S
		h - odd k - even		
		h - odd k - odd		
	h + 2k = 3p	h' - even k - even	$I \propto (f_{Al} + 3f_{Ti})^2$	● F
		h - even k - odd	$I \propto (f_{Al} - f_{Ti})^2$	○ S
		h - odd k - even		
		h - odd k - odd		
1 ≠ 2g	h + 2k = 3p	h, k = any value	I = 0	×
	h + 2k ≠ 3p	h - even k - even	$I \propto 3 (f_{Al} + 3f_{Ti})^2$	● F
		h - even k - odd	$I \propto 3 (f_{Al} - f_{Ti})^2$	○ S
		h - odd k - even		
		h - odd k - odd		

F - fundamental reflection; S - superlattice reflection and h, k, l, p, g are integers.

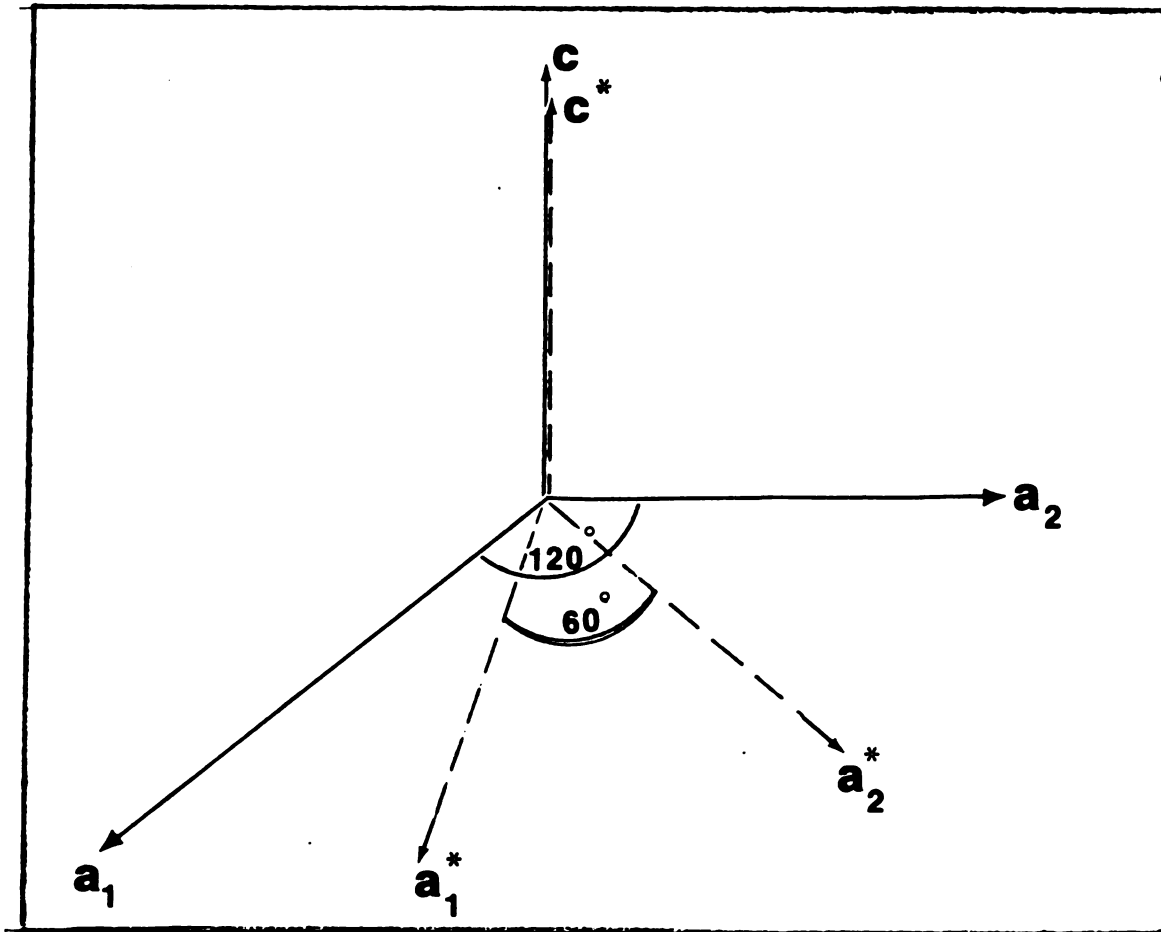


Figure 29. Geometrical relationship between the real lattice vector and the reciprocal lattice vector for a DO_{19} type crystal structure.

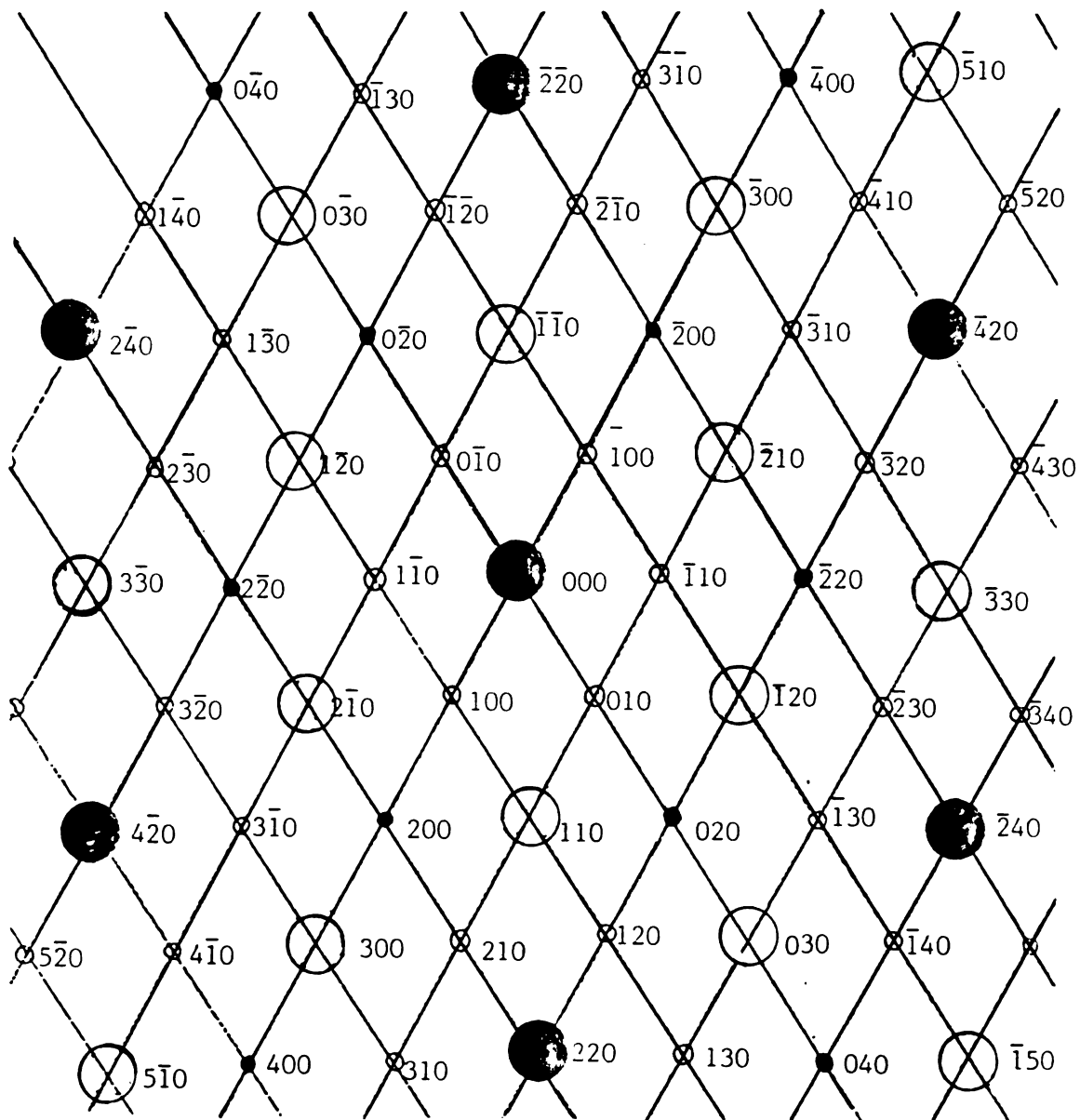


Figure 30. The reciprocal lattice plane of DO_{19} type crystal structure for $l = 0$.

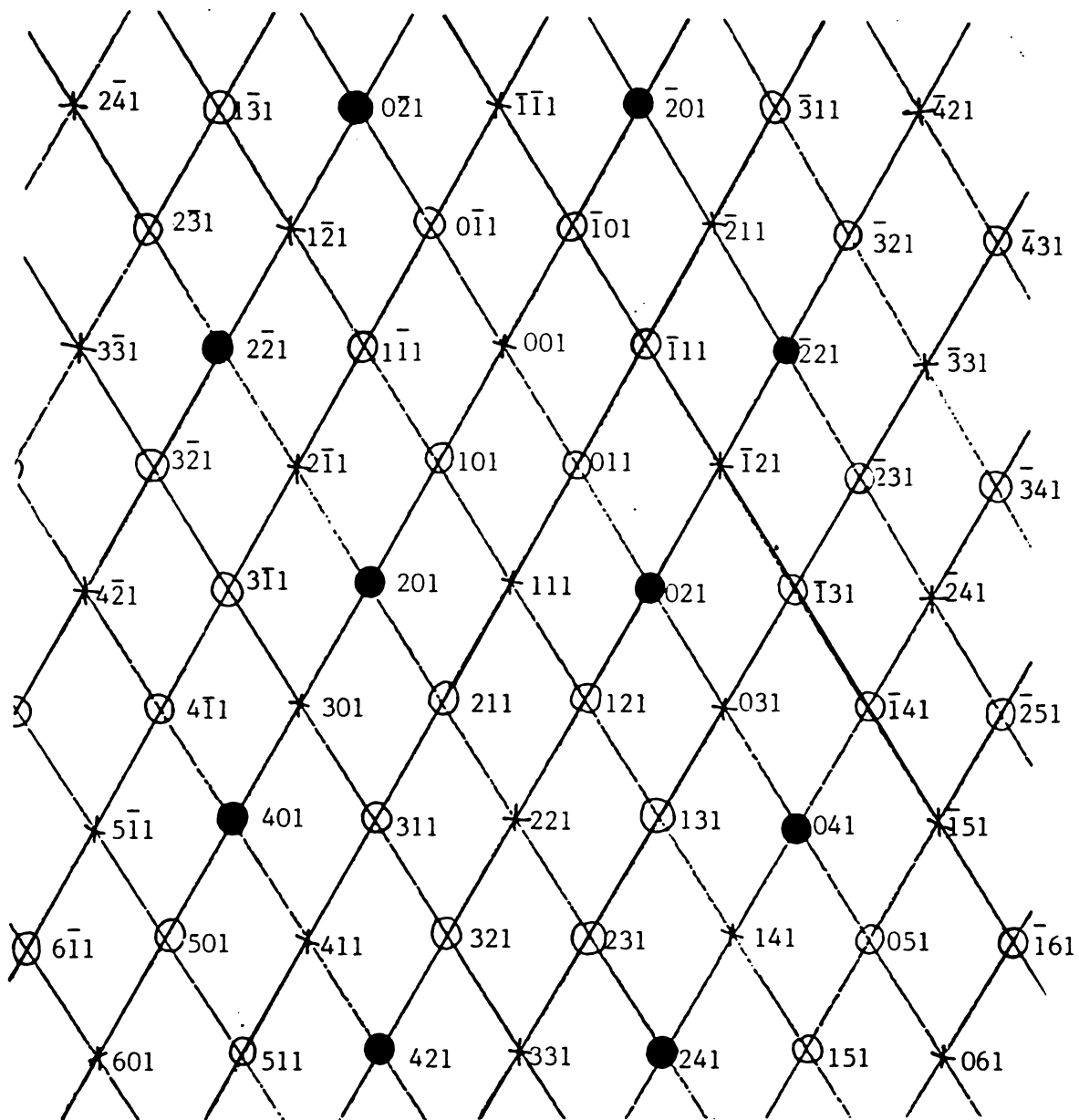


Figure 31. The reciprocal lattice plane of DO_{19} type crystal structure for $l = 0$.

where \mathbf{a}_1 , \mathbf{a}_2 and \mathbf{c} are the real lattice translations and \mathbf{a}_1^* , \mathbf{a}_2^* and \mathbf{c}^* are the reciprocal lattice vectors. V_c is the volume of the unit cell. Figure 29 explains the geometry of the vectors \mathbf{a}_1 , \mathbf{a}_2 , \mathbf{c} and \mathbf{a}_1^* , \mathbf{a}_2^* , \mathbf{c}^* . Using this geometry of the reciprocal lattice translations and the structure factor calculations (Table V) as shown previously, two reciprocal nets are drawn for $l = 0$ and $l = 1$. These two nets along with the relative intensities of the reflections are shown in Figures 30 and 31.

4.3.2 Domain Growth Studies

Ti-16Al (Ti-16Al(\approx 25 at%Al) specimens quenched from 1150°C were subsequently annealed at temperatures from 600°C to 800°C for varying times to study the antiphase domain (APD) growth kinetics. The APB structure in the annealed specimens was studied in both bright field and dark field modes in the electron microscope. Antiphase boundary contrast occurs when α , the phase angle given by $\alpha = 2\pi\mathbf{g}\cdot\mathbf{R}$, where \mathbf{g} is the operating reflection and \mathbf{R} is the boundary displacement vector, takes a non-zero value. The displacement vectors of the thermal APD boundaries were found to be of the type $\mathbf{a}/2 \langle 11\bar{2}0 \rangle$. The antiphase domain structure was studied with $(10\bar{1}0)_{\alpha_2}$, $(10\bar{1}1)_{\alpha_2}$ and $(11\bar{2}0)_{\alpha_2}$ operation reflections. All the measurements of domain sizes were measured from dark field micrographs taken with either $(10\bar{1}0)_{\alpha_2}$,

$(11\bar{2}0)_{\alpha_2}$ or $(10\bar{1}1)_{\alpha_2}$ reflection. TEM micrographs 32(a) to (f) show APD configurations in specimens annealed at 700°C for varying times (1hr, 2hrs, 5hrs, 10hrs, 20hrs and 40hrs). The APD structure in Ti_3Al forms a swirl pattern at low times of aging at 700°C but at longer times it produces a mixture of swirl and maze patterns. At longer aging times the sharp faceted features of the domain boundaries become very obvious since the domains are of a much larger size. Under certain imaging conditions a mixture of both swirl and maze patterns are visible in this system. This is understood even better from the next micrograph (Figure 33(a)) and the corresponding Selected Area Diffraction (SAD) (Figure 33(b)). The central part of this micrograph is the maze pattern and the corners show swirl pattern. This experimental observations can be attributed to crystallographic anisotropy of the APB energy in this system. Examples of systems with highly anisotropic APB energy are $L1_2$ alloys (Cu_3Pt , Cu_3Au). The APB energy has been calculated to be anisotropic, with the lowest energy on {100} planes, taking into account first nearest neighbor (NN) interactions only [Ref. 37]. Accordingly, the driving force for an APB to lie on a cube plane is extremely high in these alloys. However, there are systems where the APB energy is extremely isotropic (example Ni_3Fe , Ni_3Mn , Fe_3Al). In these alloys the domain network is of the swirl type. In the Ti-Al system, it is obvious that the anisotropy (or isotropy) of the APB energy is not as high as that of the examples given above. Higher anisotropy would result in much sharper crystallographic domain structure than that shown in the micrographs mentioned above. From Figure 33(a) and (b) it is also

Figure 32. Dark field TEM micrographs of Ti-16Al (≈ 25 at.% Al) alloy sample quenched (from 1200°C) and aged at 700°C for varying lengths of time. (a) 1 hr. (b) 2hrs. (c) 5 hrs. (d) 10 hrs. (e) 20 hrs. and (f) 40 hrs. Operating reflection was $\mathbf{g} = (10\bar{1}0)_{\alpha_2}$ and the zone normal $[\bar{1}213]$.

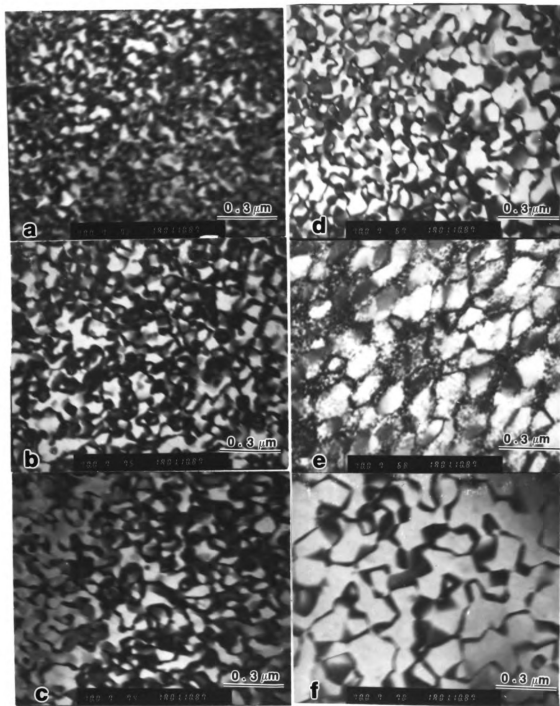


FIGURE 32

at 10000x
for 10
hrs.
ing
(10000x)

Figure 33. (a) Dark field TEM micrograph of Ti-16Al (≈ 25 at.% Al) alloy sample quenched (from 1200°C) and aged at 700°C for 20 hours. (b) SAD of the region shown in (a), showing a $[\bar{1}\bar{2}13]$ zone normal.

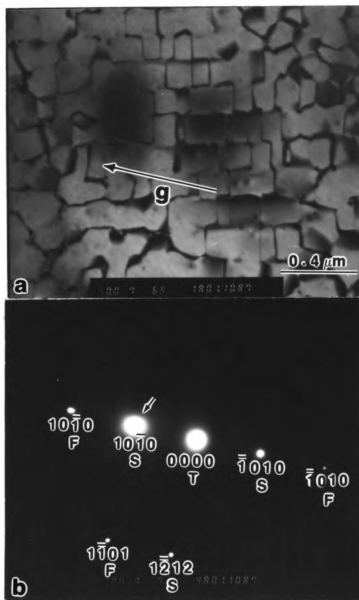


FIGURE 33

possible to say that this anisotropy of the APB energy, in Ti-Al system, is along irrational crystallographic planes.

The next set of micrographs (Figure 34(a)-(c)) shows APD's at 800°C aging temperature at various times. Here also at higher aging times the sharp crystallographic facets of the domains become very obvious because of the relatively larger size of the domains. However, this anisotropy is not as high as some of the systems mentioned above and therefore, a mixture of sharp and rounded featured domains are visible most of the time.

The next set of micrographs (Figure 35) shows the bright field and dark field images of the domains in Ti-16Al(≈25 at.%Al) aged at 800°C for 40 hrs. The arrow in the micrograph indicates the superlattice spot chosen for the dark field. Marcinkowski [Ref. 25] has calculated the values of the phase angle α for various reflections for the APB vectors $\mathbf{a}_s/2 \langle 11\bar{2}0 \rangle$ and $\mathbf{a}_s/6 \langle 10\bar{1}0 \rangle$ in the DO_{19} lattice. It is not proposed to give a complete analysis of the APB vectors here but an example will be given to demonstrate the $\mathbf{a}_s/2 \langle 11\bar{2}0 \rangle$ vector occurs almost exclusively. It is found that π contrast is observed with all superlattice reflections as illustrated by the symmetrical contrast reversal in the light and dark field micrographs, [Figure 35(a) and (c)]. Further, in these micrographs the operating reflection is $(10\bar{1}0)_{\alpha_2}$ and the π contrast is consistent with the $\mathbf{a}_s/2 \langle 11\bar{2}0 \rangle$ and not the $\mathbf{a}_s/6 \langle 10\bar{1}0 \rangle$ vector. Similar results were shown by Blackburn for different operating reflections [Ref. 19].

Figure 34. Dark field TEM micrograph of Ti-16Al (≈ 25 at. % Al) alloy sample quenched (from 1200°C) and aged at 800°C for varying lengths of time. (a) 2 hours, (b) 20 hrs. and (c) 40 hrs.. Operating reflection was $\mathbf{g} = (10\bar{1}0)_{\alpha_2}$ and the zone normal $[\bar{1}\bar{2}13]$.

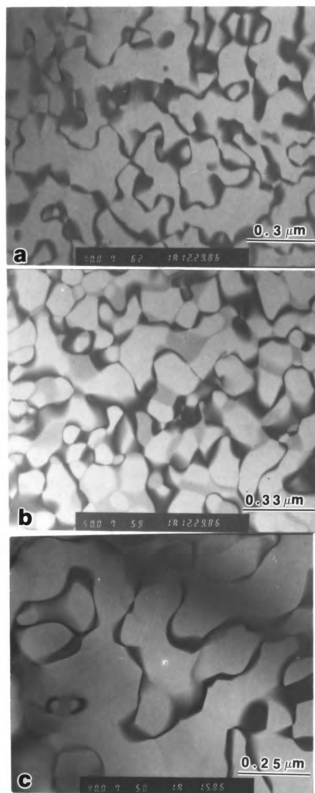


FIGURE 34

Figure 35. (a) Bright field (b) SAD (c) dark field micrograph of Ti-16Al (≈ 25 at.% Al) sample quenched (from 1200°C) and aged for 40 hrs. at 800°C . Please note the symmetrical contrast reversal in the bright and the dark field. $\mathbf{g} = (10\bar{1}0)_{\alpha_2}$. APB vector $\mathbf{a}_S/2\langle 11\bar{2}0 \rangle$.

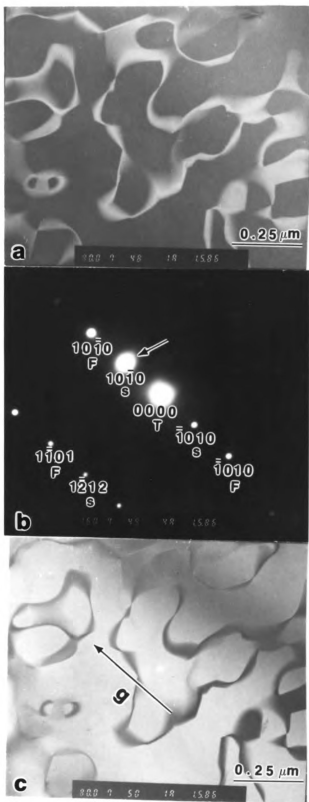


FIGURE 35

The domain growth as a function of time was studied at 600, 700 and 800°C for Ti-16Al(≈25 at.%Al). The average domain size as a function of time and temperature of annealing was determined by linear intersection analysis from several electron micrographs for each condition of heat treatment. Histograms drawn in Figure 36(a), (b), (c) show some typical size distributions observed at different temperatures. It can be seen from these histograms that at higher aging temperatures and longer aging times the average domain sizes becomes larger. It can also be seen from Figure 36 (a), (b) and (c) that different domain sizes are present at different heat treatments. However, it is expected that higher aging temperatures and longer aging times would reduce this scattering. Figure 37 shows a logarithmic plot of average domain size as a function of annealing time at different temperatures. The slope of the $\log D$ Vs $\log t$ varies from ≈ 0.4 to 0.6 . Thus, the domain growth can be approximated by a $D \propto t^n$ relationship where $n \approx 1/2$. This shows that the average domain size has a parabolic relationship with aging time which is indicative of a thermally activated process. Hence, as indicated before, the process of ordering and domain growth is diffusion assisted. However, the exact mechanics of this process needs further investigation.

Before concluding this discussion on TEM results it is important to mention that (1) no superlattice reflection or APD's were observed in samples quenched from 1200°C (which is contrary to the observations made by other workers [Ref. 19,68]) and (2) that the transformation from disorder \rightarrow order proceeds by a nucleation and growth mechanism which is diffusion assisted.

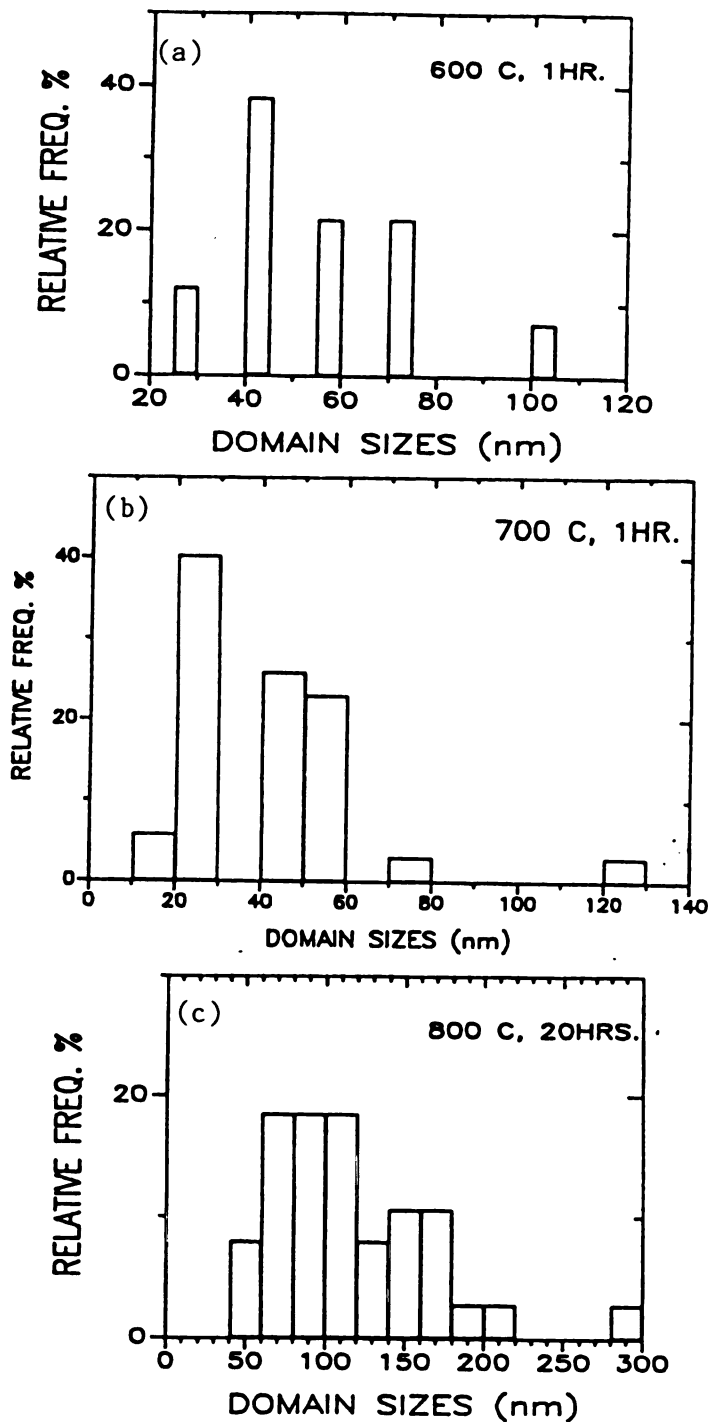


Figure 36. Histograms showing the distribution of domain sizes for different aging treatments. (a) 600°C 1 hour, (b) 700°C 1 hour and (c) 800°C 20 hours.

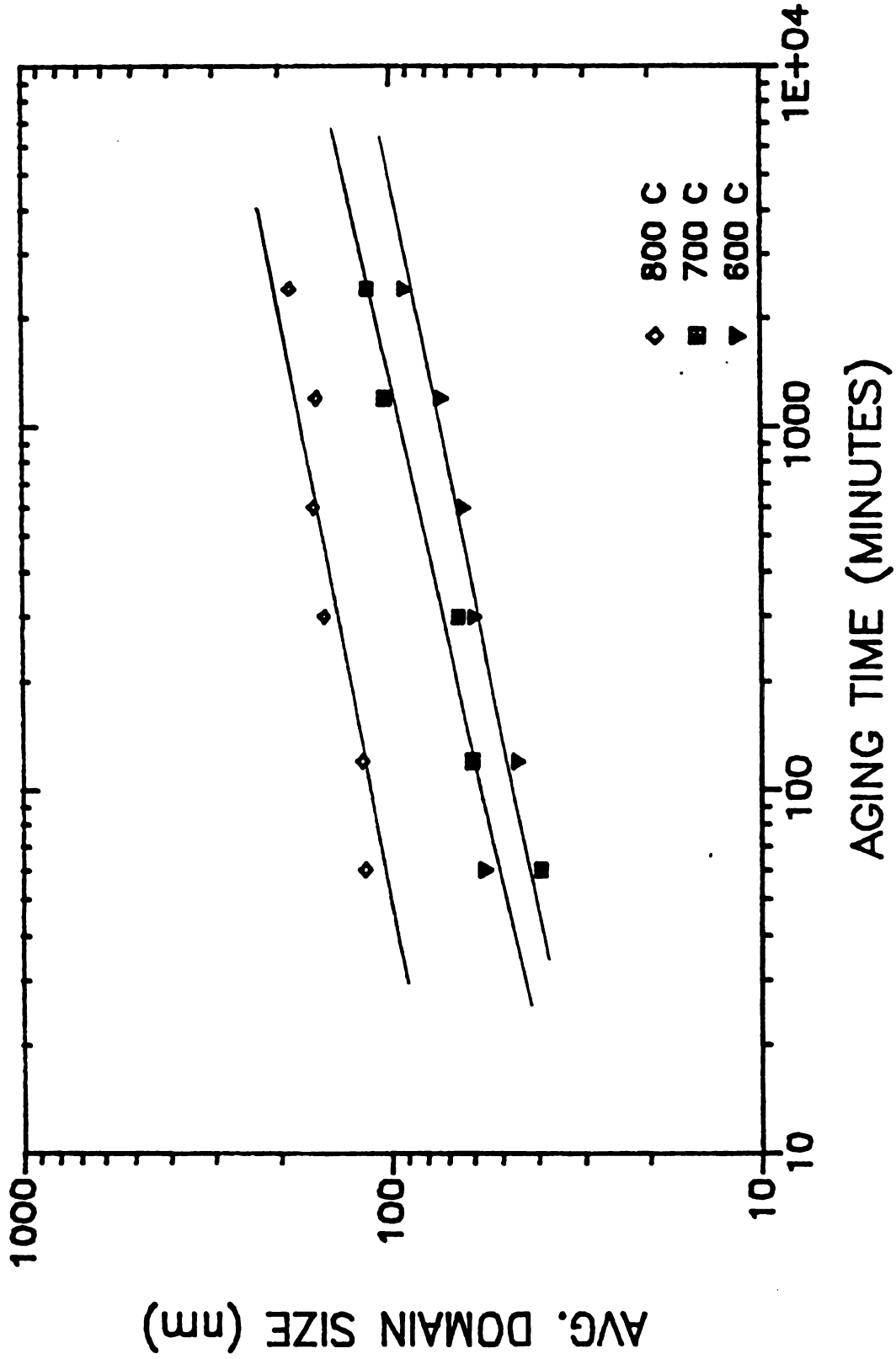


Figure 37. Logarithmic plot of average domain size versus aging time in minutes for Ti-16Al (~25 at. % Al) at different temperatures indicated.

4.4 MICROHARDNESS RESPONSE

The microhardness response of Ti-16Al (~25 at% Al) alloy with respect to the aging time at different temperatures (600, 700 and 800°C) has been investigated. Figure 38 shows a plot of Vicker's hardness number as a function of the aging time in hours at different temperatures. From the figure, it can be seen that on aging the samples after quenching from 1200°C there is an immediate increase in the hardness values. However, further aging leads to higher hardness values after which there is a decrease of the hardness of the material. This behavior is analogous to that of systems which show precipitation hardening effects when a supersaturated solid solution is aged. The hardness response for the samples between 0 and 1 hour and between 2 to 5 hours of aging is not known due to the present design of the experiments. However, it can be safely argued that higher hardness values (as compared to quenched hardness values) are reached between 0 and 5 hours of aging depending on the aging temperature. This aging time corresponds to a domain size of approximately 60 to 120 nm as can be seen from Figure 37. This means that the increase in hardness in this system, produced by aging, is due to the process of ordering and also because of the very small domain sizes during the initial stages of aging. Longer aging times (say, 40 hours) causes an increase of the domain sizes and hence leads to a decrease in the hardness value below the higher hardness values obtained due to aging for shorter times. However, as can be seen from above, a more rigorous experimental design is necessary in order to observe this effect better.

As mentioned before, in order to have an understanding of the disordering kinetics of this transformation, a theoretical approach

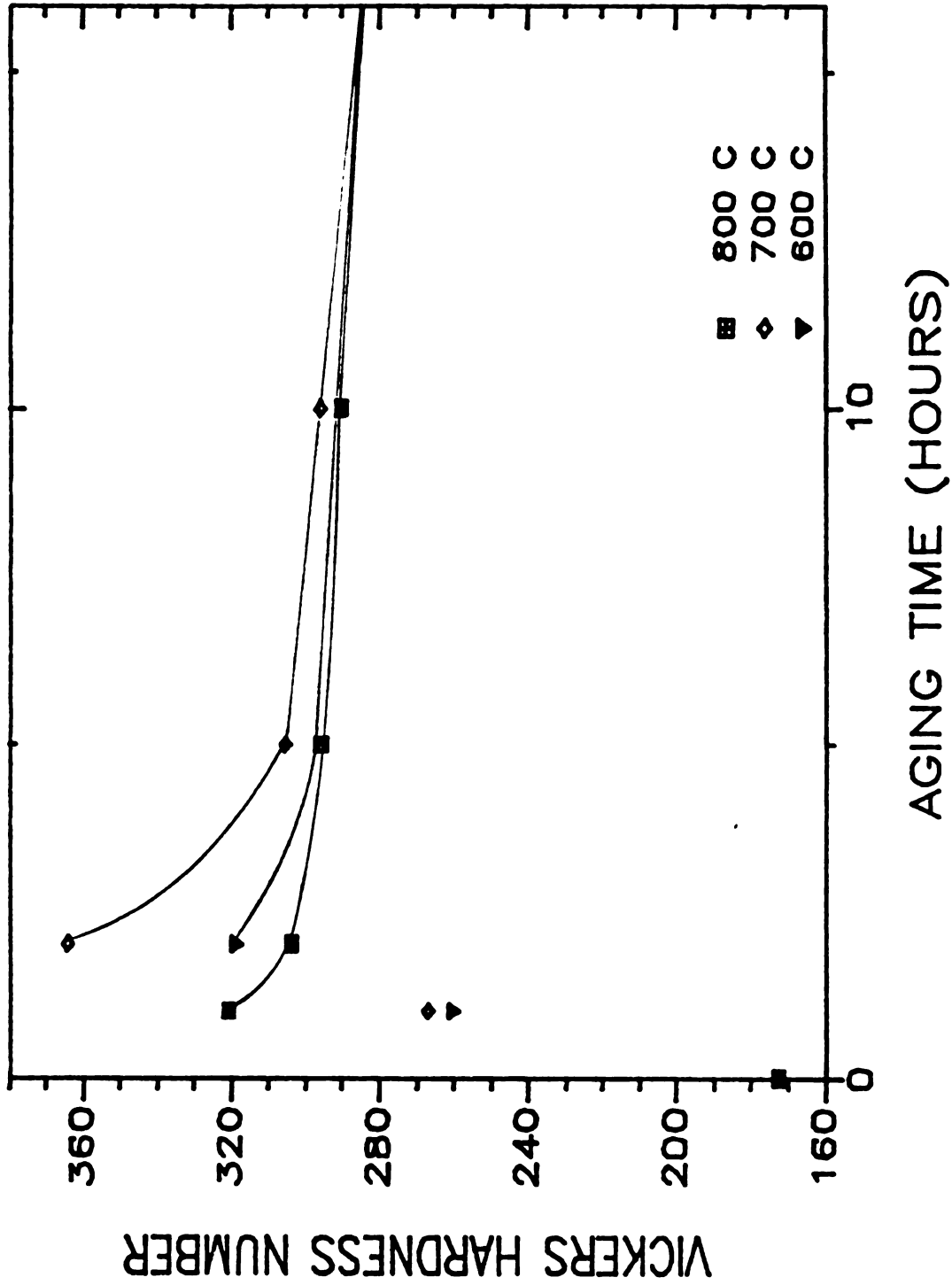


Figure 38. Plot of Vicker's hardness number as a function of aging time in hours for Ti-16Al (~25 at.% Al) at the different temperatures indicated.

using the Bragg William mean field (quasi chemical) nearest neighbor (atoms) in DO_{19} structure is applied.

4.5 BRAGG-WILLIAM APPROXIMATION OF THE ORDER DISORDER TRANSFORMATION TEMPERATURE FOR DO_{19} STRUCTURE IN TITANIUM ALUMINUM SYSTEM.

Consider Figure 39, in which three unit cells of the DO_{19} structure are drawn together. In this figure, the aluminum atoms are indicated by full circles (●) and titanium atoms are indicated by open circles (○).

The three unit cells joined together allow us to envision two distinct interpenetrating sublattices which make up the DO_{19} crystal structure. Sublattice I which is the preferred sites of the titanium atoms only and sublattice II which is the preferred site of the aluminum atoms only are indicated by ABCDEFGH and A'B'C'D'E'F'G'H' respectively. There are 6 atoms/unit cell in sublattice I and 2 atoms/unit cell in sublattice II.

For the sole purpose of simplifying the notation system, the titanium and the aluminum atoms are designated as A and B atoms respectively.

The ratio of A atoms to B atoms in the DO_{19} crystal structure is 3:1, which is consistent with the formula A_3B . Let N be the total number of atoms. Hence, $(3/4)N$ atoms are in sublattice I and $(1/4)N$ are in sublattice II. Let us define a long range order parameter W, such that $W = 1$ when the system is ordered and $W = 0$ when the system is fully

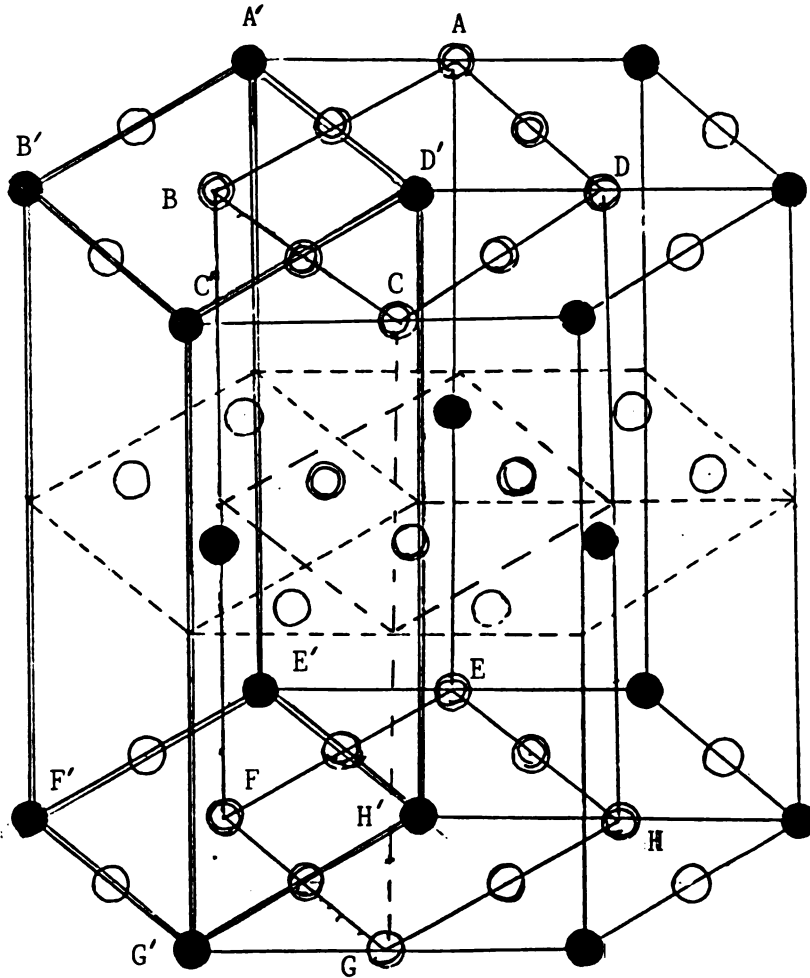


Figure 39. Three unit cells of the DO_{19} crystal structure. ABCDEFGH indicates sublattice I (Ti atoms) and A'B'C'D'E'F'G'H' indicates sublattice II (Al atoms). Please note that these two sublattices are interpenetrating.

disordered. When $W = 0$, $1/4$ of the sublattice sites are statistically occupied by B atoms and $3/4$ by A atoms

When $W = 0$, the number of A atoms statistically in sublattice I
 $= (3/4)N \times 3/4 = (9/16)N$.

Similarly, when $W = 0$, the number of B atoms statistically in
 sublattice I $= (3/4)N \times 1/4 = (3/16)N$.

Number of A atoms in sublattice II when $W = 0$ is given by $(1/4)N$
 $\times 3/4 = (3/16)N$.

Similarly, the number of B atoms in sublattice II when $W = 0$ is
 $(1/4)N \times 1/4 = (1/16)N$.

In terms of the ordering parameter W , then:

$$\text{Number of A atoms in sublattice I} = (3 + W)(3/16)N$$

$$\text{Number of B atoms in sublattice I} = (1 - W)(3/16)N$$

$$\text{Number of B atoms in sublattice II} = (1 + 3W)(1/16)N$$

$$\text{Number of A atoms in sublattice II} = (1 - 3W)(3/16)N$$

Let us define the probability of finding an A atom in sublattice
 I as $p_{A,I}$ such that,

$$p_{A,I} = \frac{\text{Number of A atoms in sublattice I}}{\text{Number of atoms in sublattice I}} = \frac{(3 + W)(3/16)N}{(3/4)N} = (3 + W)/4$$

Similarly,

$$p_{B,I} = \frac{(1 - W)(3/16)N}{(3/4)N} = (1 - W)/4$$

$$p_{B,II} = \frac{(1 + 3W)(1/16)N}{(1/4)N} = (1 + 3W)/4$$

$$P_{A,II} = \frac{(1 - W)(3/16)N}{(1/4)N} = 3(1 - W)/4$$

Let, $Z_{I,I}$ - number of atoms of sublattice I around each atom of sublattice I = 8

$Z_{I,II}$ - number of atoms of sublattice II around each atom of sublattice I = 4

$Z_{II,I}$ - number of atoms of sublattice I around each atom of sublattice II = 12

$Z_{II,II}$ - number of atoms of sublattice II around each atom of sublattice II = 0

The above definitions are on the basis of first nearest neighbor interactions only. Let E be the total energy of the system. When defined by the bond energy of nearest neighbors,

$$E = [E_I + E_{II}]/2$$

where, E_I = energy of sublattice I and E_{II} = energy of sublattice II.

The factor 1/2 comes in because the bonds are counted twice when individual sublattice energies are considered.

In terms of the above definitions, we can write,

$$E_I = N_I [P_{A,I} \{ (P_{A,II} \cdot V_{AA} + P_{B,II} \cdot V_{AB}) Z_{I,II} + (P_{A,I} \cdot V_{AA} + P_{B,I} \cdot V_{AB}) Z_{I,I} \} + P_{B,I} \{ (P_{A,II} \cdot V_{BA} + P_{B,II} \cdot V_{BB}) Z_{I,II} + (P_{A,I} \cdot V_{BA} + P_{B,I} \cdot V_{BB}) Z_{I,I} \}]$$

$$E_{II} = N_{II} [P_{B,II} (P_{B,I} \cdot V_{BB} + P_{A,I} \cdot V_{BA}) Z_{II,I} + P_{A,II} (P_{B,I} \cdot V_{AB} + P_{A,I} \cdot V_{AA}) Z_{II,I}]$$

where N_I = number of atoms in sublattice I,

N_{II} = number of atoms in sublattice II

Putting the values of probabilities(P) and co-ordination number (Z), we have,

$$E_I = 3N/16[27V_{AA} + 6WV_{AA} - W^2V_{AA} + 18V_{AB} - 4WV_{AB} + 2W^2V_{AB} + 3V_{BB} - 2WV_{BB} - W^2V_{BB}]$$

$$E_{II} = 3N/16[9V_{AA} - 6WV_{AA} - 3W^2V_{AA} + 6V_{AB} + 4WV_{AB} + 6W^2V_{AB} + V_{BB} + 2WV_{BB} - 3W^2V_{BB}]$$

Therefore,

$$E = 3N/16[18V_{AA} - 2W^2V_{AA} + 12V_{AB} + 4W^2V_{AB} + 2V_{BB} - 2W^2V_{BB}]$$

Derivative of E(W) with respect to W gives,

$$\begin{aligned} dE(W)/dW &= 3N/16[-4WV_{AA} + 8WV_{AB} - 4WV_{BB}] \\ &= 3NW/4[2V_{AB} - V_{AA} - V_{BB}] = 3NW^*/4. \end{aligned}$$

Entropy considerations give:

$S_{mix} = S_{mix,I} + S_{mix,II}$ where, $S_{mix,I}$ is the entropy of mixing for sublattice I, and $S_{mix,II}$ is the entropy of mixing for sublattice

II. Let K be the Boltzmann constant. Thus,

$$S_{mix} = [-KN_I(P_{A,I} \ln P_{A,I} + P_{B,I} \ln P_{B,I})] + [-KN_{II}(P_{A,II} \ln P_{A,II} + P_{B,II} \ln P_{B,II})]$$

which on simplification gives,

$$\begin{aligned} S_{mix} &= (-KN/16)[(9 + 3W)\ln(3 + W) - 9\ln 4 - 3W\ln 4 + (3 - 3W)\ln(1 - W) - \\ &3\ln 4 + 3W\ln 4 + 3\ln 3 - 3W\ln 3 + (3 - 3W)\ln(1-W) - 3\ln 4 + 3W\ln 4 + \\ &(1 + 3W)\ln(1 + 3W) - \ln 4 - 3W\ln 4]. \end{aligned}$$

Derivative of S_{mix} with respect to W gives,

$$dS_{\text{mix}}(W)/dW = (KN/16)[3\ln(3 + W) - 6\ln(1 - W) + 3\ln(1 + 3W) - 3\ln 3].$$

We know from the laws of thermodynamics,

$$E(W) - TS_{\text{mix}}(W) = F(W), \text{ where } F(W) \text{ is the free energy as a}$$

function of W . We know,

$$dE(W)/dW - TS_{\text{mix}}(W)/dW = dF(W)/dW = 0 \text{ for equilibrium.}$$

$$\text{Hence, } (3WV^*)/4 + (KT/16)[\ln(3 + W) - 2\ln(1-W) + \ln(1 + 3W) - \ln 3] = 0$$

As discussed earlier, V^* is a negative quantity. Thus,

$$|V^*|/(KT) = [\ln(3 + W) - 2\ln(1-W) + \ln(1 + 3W) - \ln 3]/(4W)$$

Similar calculations for β -brass (B2) type of alloys would yield,

$$(dE/dW)_{\text{B2}} = 2NWV^*$$

$$(dS_{\text{mix}}/dW)_{\text{B2}} = (-KN/2)[\ln((1 + W)/(1 - W))]$$

$$\text{and } |V^*|_{\text{B2}}/(KT) = [\ln((1 + W)/(1 - W))]/(4W)$$

Figure 40 and Figure 41 shows the plot of W vs. $(KT)/|V^*|$ for DO_{19} and B2 (β -brass) type of structures. For the B2 structure (Fig. 41) we see that with increasing values of $(KT)/|V^*|$, that is increasing temperature, the system gradually converts from an ordered structure $W = 1$, to a disordered structure. This response is of the second order type.

However, there is a marked difference in the response for the DO_{19} type of structure (Fig. 40). When compared to the B2 structure we see that with increasing temperature the system disorders continuously until a value of $W = 0.3$ and $(KT)/|V^*| = 0.83$ (approx.) is reached.

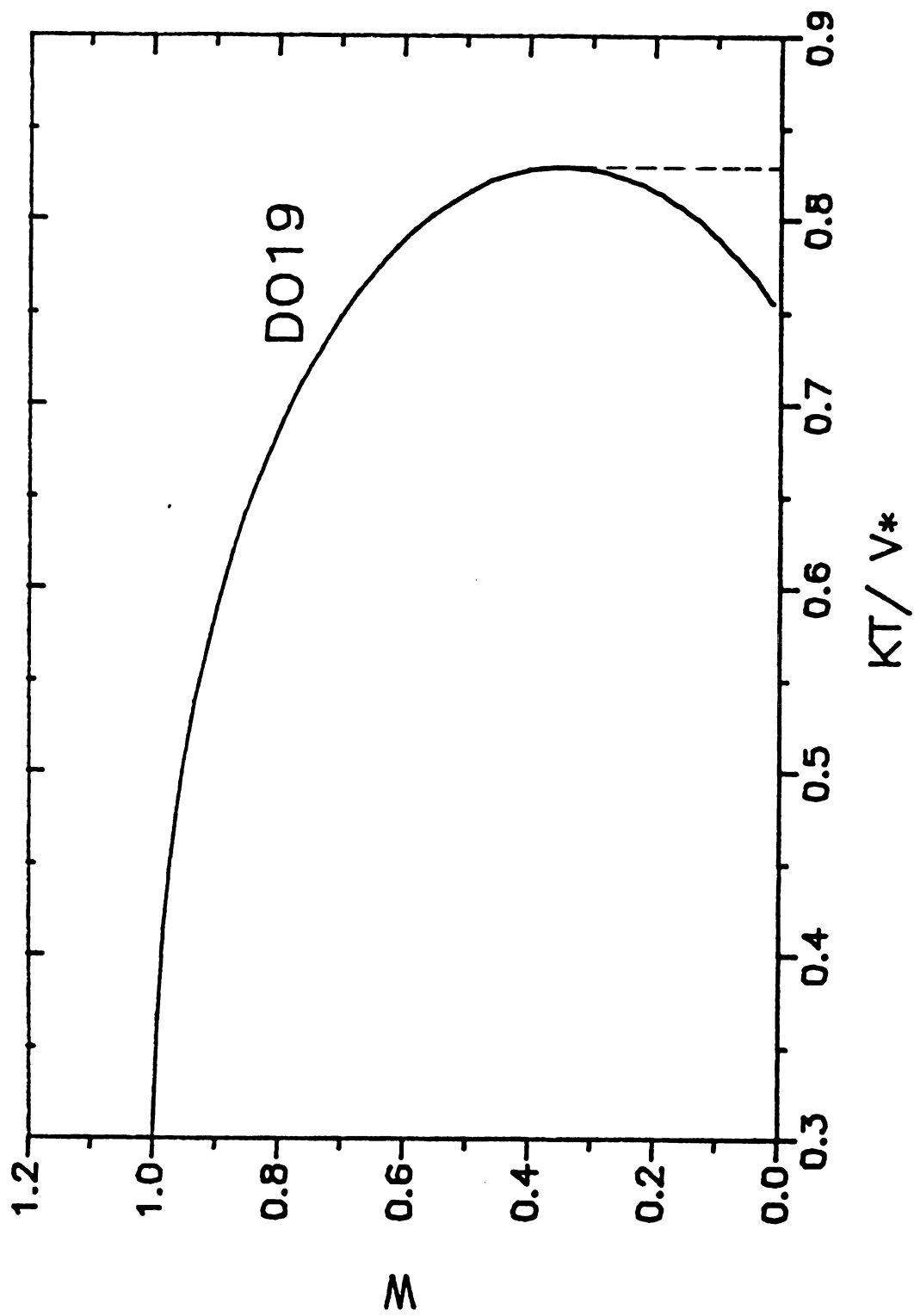


Figure 40. Plot of ordering parameter W versus $(KT)/|V^*|$ for the DO₁₉ type crystal structure.

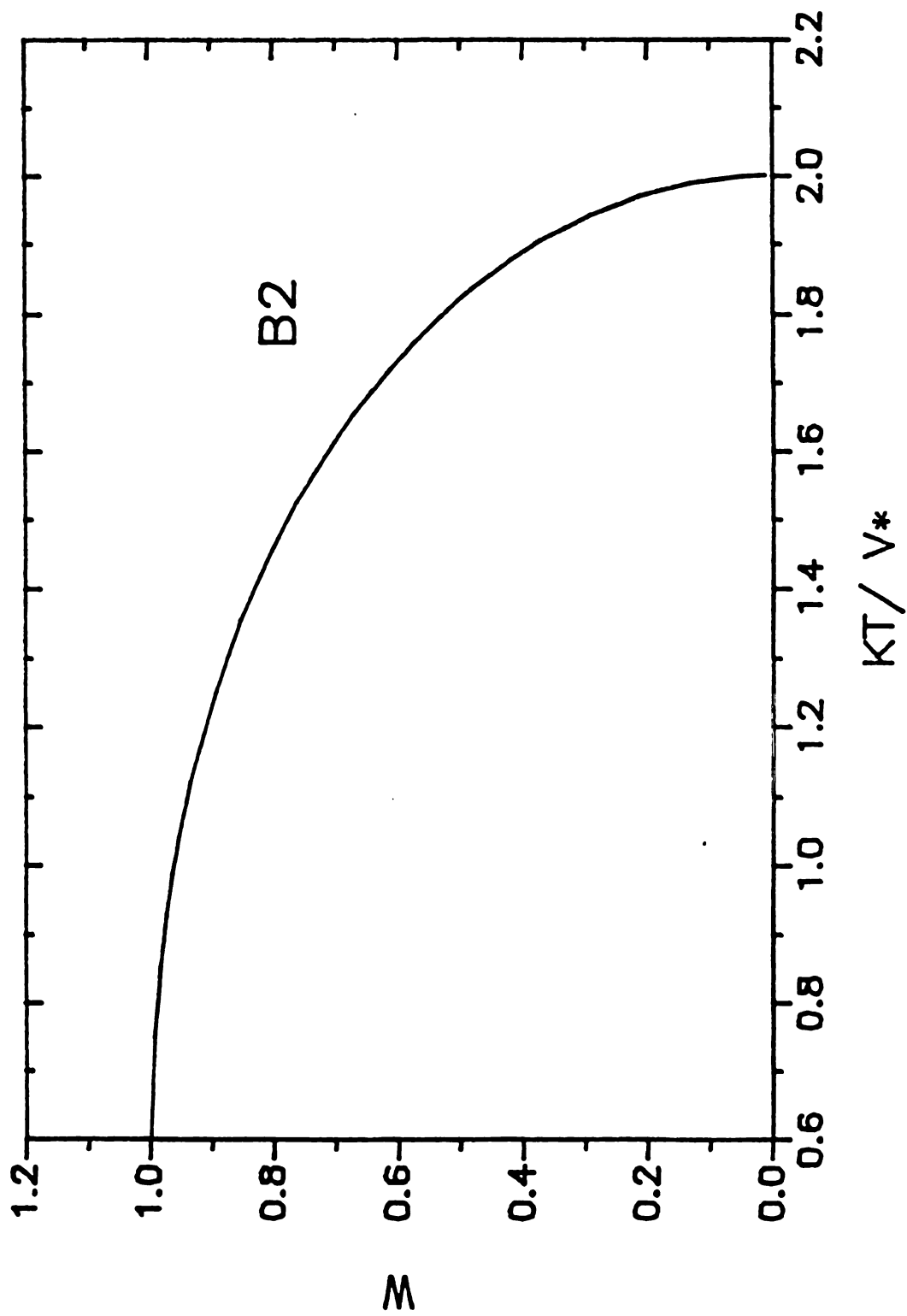


Figure 41. Plot of ordering parameter W versus $(KT)/|V^*|$ for the B2 type of crystal structure.

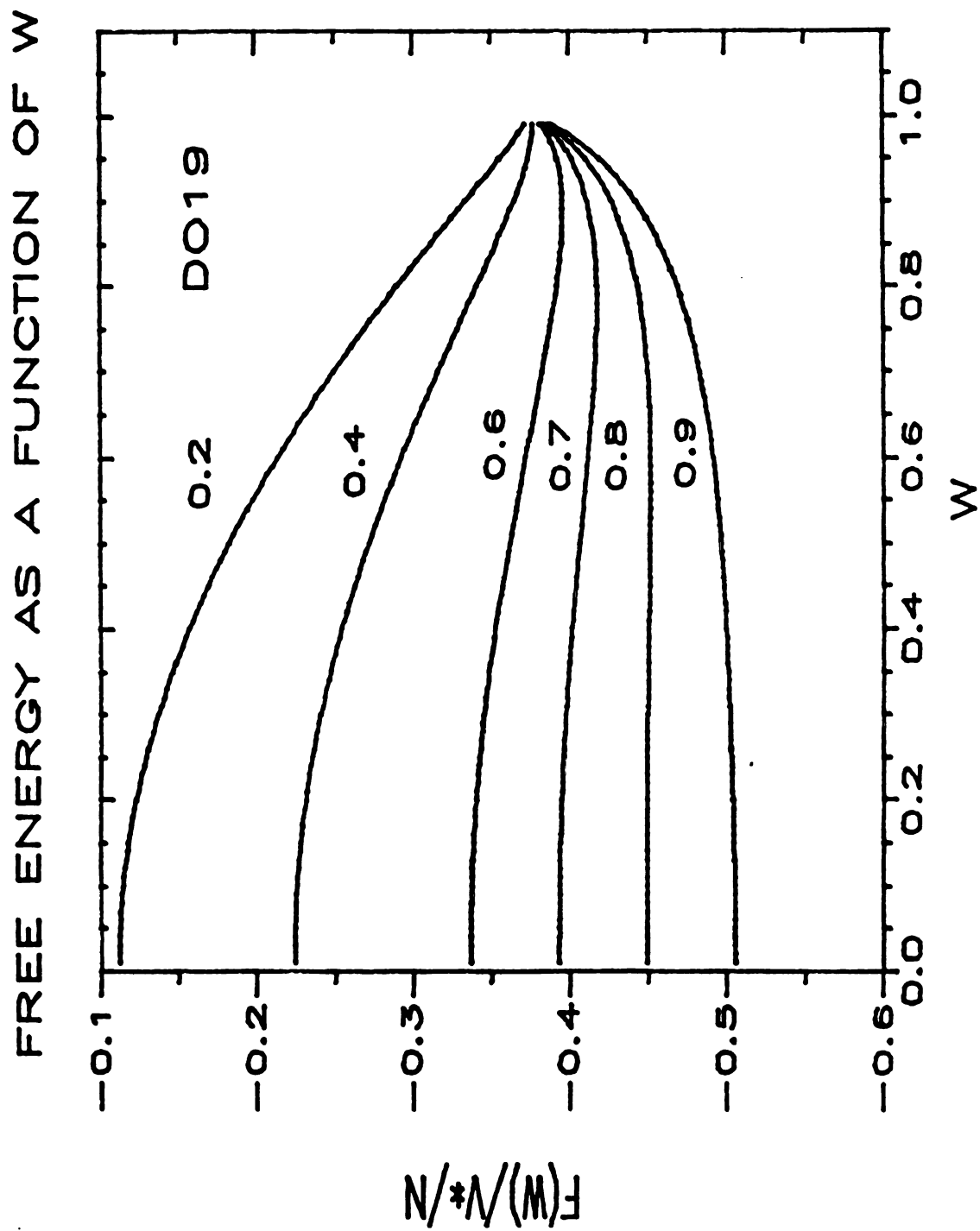


Figure 42. Free energy as a function of W with increasing $(KT)/|V^*|$ values for DO₁₉ crystal structure.

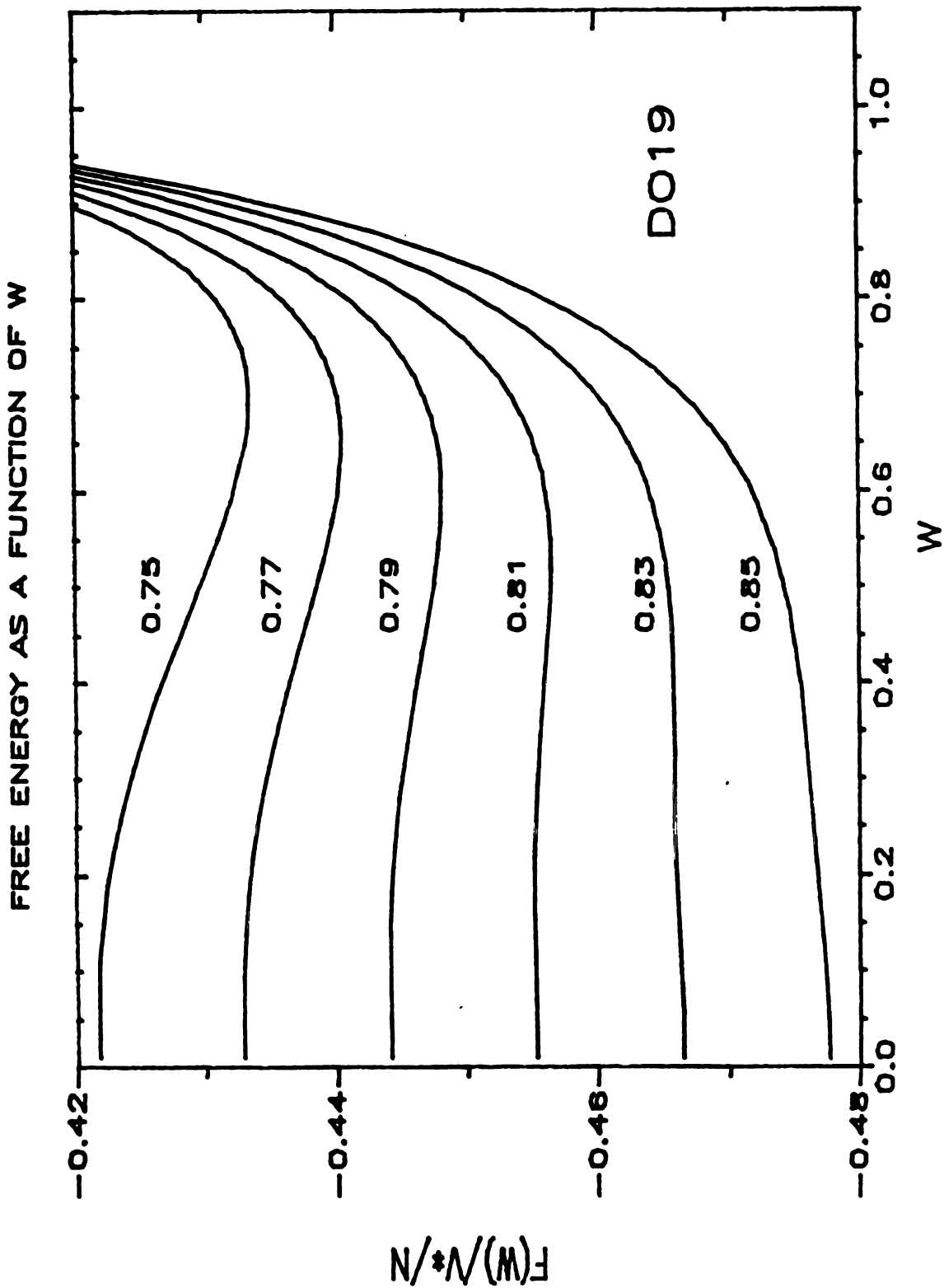


Figure 43. Free energy as a function of W with increasing $(KT)/|V^*|$ values for DO₁₉ crystal structure.

Beyond this point however, the behavior of the curve does not have any physical significance. A straight forward interpretation of of the graph would mean that beyond $W = 0.3$, the system disorders further with the decrease of temperature. In order to understand the problem further, a plot of free energy as a function of W is made (Fig. 42) with increasing temperature.

As can be seen from this figure, with increasing temperature the free energy minima shifts steadily from $W = 1$ to $W = 0$. However, this shift is gradual upto a $(KT)/|V^*|$ value of 0.8 approximately. Beyond this value however, the minimum free energy is attained only at $W = 0$. This fact is further exemplified in Figure 43 where a plot similar to that of Figure 42 is made; but the $(KT)/|V^*|$ values chosen are on the higher and lower sides of 0.8. This plot further explains the above logic explicitly.

Thus after $(KT)/|V^*| = 0.83$ and $W = 0.3$ values are reached, on further heating, the free energy of the system is instantly minimised by disordering. This transformation is therefore of the first order type, unlike that of the B2 type structure.

Let T_c define the critical temperature at which the system abruptly transforms to a disordered structure. Thus,

$(KT_c)/|V^*| = 0.83$ approximately for the DO_{19} structure. This result differs by a factor of two from the result obtained by Yang and Li [Ref. 72, 73, 74], which indicates $(KT_c)/|V^*| = 0.41$ for both $L1_2$ and DO_{19} crystal structures. Further experimental work needs to be

performed to verify this result. From above it can be written for the DO₁₉ structure,

$$|V^*|/(KT_c) = 1.205, \text{ that is, } |V^*| = 1.205KT_c.$$

From previous calculations we know,

$$4|V^*|/(KT) = (1/W)[\ln\{(3+W)(1+3W)/(3-6W+3W^2)\}], \text{ that is,}$$

$$(4 \times 1.205KT_c)/(KT) = (1/W)[\ln\{(3+W)(1+3W)/(3-6W+3W^2)\}]$$

$$\text{Thus, } (T/T_c) = 4.82W/[\ln\{\ln(3+W)(1+3W)/(3+3W^2-6W)\}]$$

Similar calculations for B2 structure yields,

$$(T/T_c)_{B2} = 2W/(\ln(1+W)/(1-W)), \text{ where } T \text{ is the test}$$

temperature. The next figure [Fig. 44] shows the plot of W as a function of (T/T_c) for both DO₁₉ and B2 crystal structures. This plot shows that DO₁₉ disorders more gradually than B2 initially, but beyond $W = 0.3$ it disorders abruptly.

The above calculations have been concerned primarily with a Ti-alloy of a stoichiometric composition, namely, A₃B. However, as has been shown previously, ordering in this system is also associated with non-stoichiometric composition alloys. In the case of first-order transformations there is always a two-phase region at non-stoichiometric compositions wherein the transformation can be expressed as: disordered phase → ordered precipitates + disordered matrix. In the Ti-Al system, referring to the phase diagram in Figure 27, for non-stoichiometric compositions we have $\alpha \rightarrow \alpha_2 + \alpha$. This result, coupled with the fact that the disorder → order transformation in this system is of the first order type leads one to suggest that the phase diagram proposed by

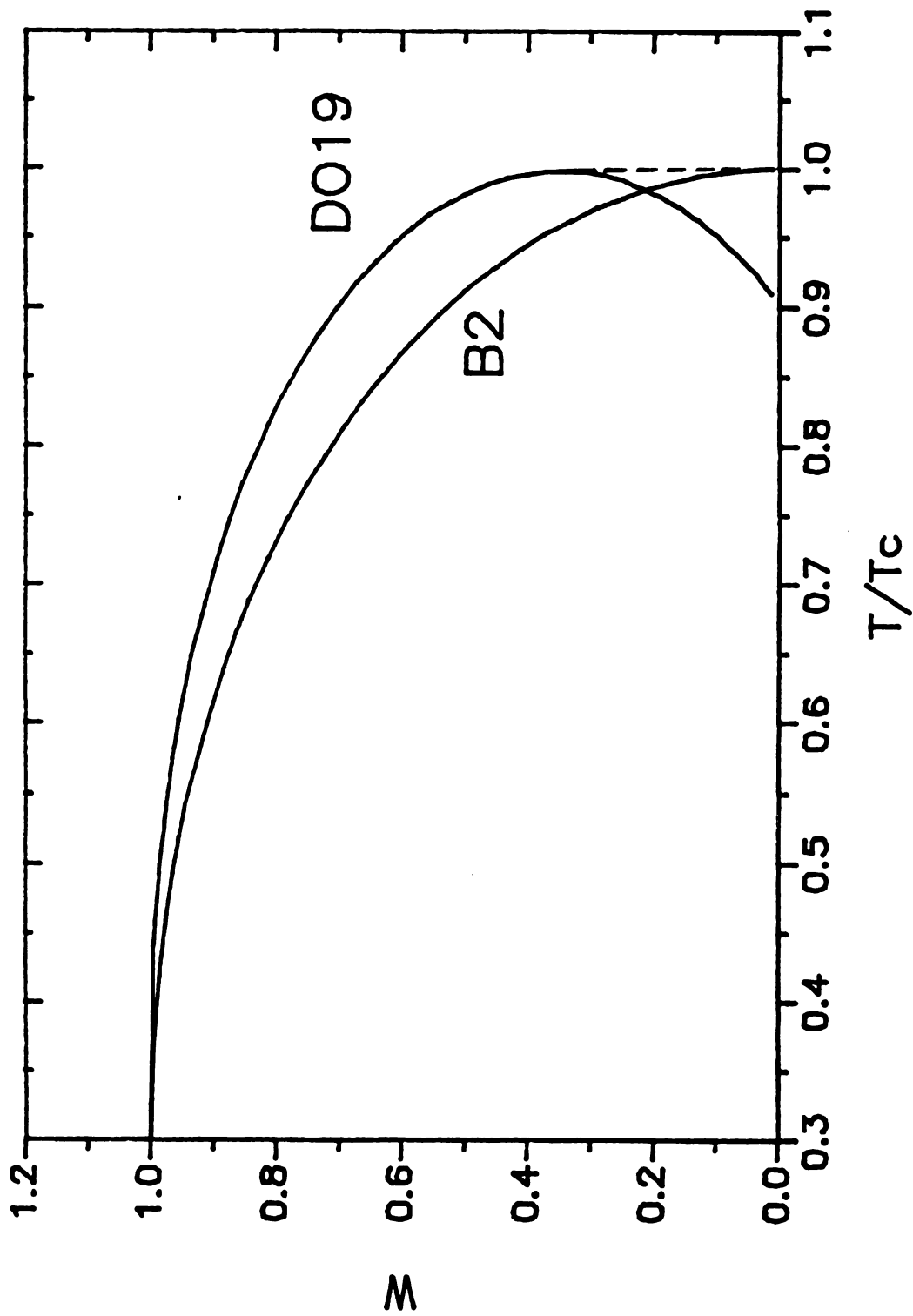


Figure 44. Plot of W as a function of (T/T_c) for both DO19 and B2 type crystal structures.

Crossley [Ref. 18] is incorrect. There is a change of composition involved on ordering and hence, long range diffusion is involved. Second order transformations on the other hand do not involve a two phase region even at non-stoichiometric compositions (Fig. 11).

CHAPTER 5

CONCLUSIONS

From the results obtained a number of important conclusions can be drawn which can be summarized as follows:

1. Through DSC/DTA, X-ray diffraction, electron microscopy and theoretical calculations, a phase diagram (Fig. 27) for the Ti-rich end of the Ti-Al system is proposed.

2. The diagram proposed matches well with the phase diagram proposed by Blackburn (Fig. 5), although the phase boundaries are shifted to higher temperatures and higher aluminum concentration as compared with it.

3. The kinetics of the ordering process is composition dependent and is sluggish at higher aluminum contents.

4. The ordering transformation in Ti_3Al proceeds by nucleation of small ordered domains and the subsequent growth of these domains.

5. The domain growth in this system can be approximated by a $D \propto t^n$ relationship, where $n \approx 1/2$. D is the average domain size, and t is the aging time. This relationship is indicative of a thermally activated process.

6. The hardness response on aging, in this system, is related to the domain growth kinetics and the size of the domains.

7. Theoretical predictions show that the disorder \rightarrow order transition in Ti-Al system is of the first order type.

8. The $\langle \mathbf{a}_s/2 \langle 11\bar{2}0 \rangle$ vector occurs almost exclusively in the Ti-Al system as exemplified by the symmetrical contrast reversal in light and dark-field micrographs (Fig. 35).

REFERENCES

1. H. R. Ogden, D. J. Maykuth, W. L. Finlay, and R. I. Jaffee: AIME Trans., vol. 191, pp. 1150-55, 1951.
2. E. S. Bumps, H. D. Kessler, and M. Hansen: AIME Trans., vol. 194, pp. 609-14, 1952.
3. I. I. Kornilov, E. N. Pylaeva, and M. A. Volkova: Izv. Akad. Nauk sssr, Otd. Khim. Nauk, pp. 771-78, 1956.
4. K. Sagel, E. Schulz, and U. Zwicker: Z. Metallk., vol. 46, pp. 529-34, 1956.
5. D. Clark, and J. C. Terry: Bull. Inst. Metals., vol. 3, pp. 116, 1956.
6. F. A. Crossley and W. F. Carew: AIME Trans., vol. 209, pp. 43-46, 1957.
7. K. Anderko, K. Sagel, and U. Zwicker: Z. Metallk, vol. 48, pp. 57-58, 1957.
8. E. Ence and H. Margolin: AIME Trans., vol. 209, pp. 484-85, 1957.
9. A. Saulnier and M. Croutzeilles: Compt. Rend., vol. 246, pp. 3622-25, 1958.
10. A. Saulnier and M. croutzeilles: Mem. Sci. Rev. Met., vol. LVI, pp. 378-87, 1959.
11. I. I. Kornilov and T. T. Nartove: Dokl. Akad. Nauk SSSR, vol. 131, pp. 837-39, 1960.
12. T. Sato and Y. Huang: Trans. Japan Inst. Metals, vol. 1, pp. 22-27, 1960.
13. A. J. Goldak, and J. Gordon Parr: Trans. Met. Soc. AIME, vol. 221, pp. 639-40, 1961.
14. E. Ence and H. Margolin: Trans. Met. Soc. AIME, vol. 221, pp. 151-57, 1961.
15. N. V. Grum-Gvzhimailo, I. I. Kornilov, E. N. Pylaeva, and M. A. Volkova: Dokl. Akad. Nauk SSSR, vol. 137, pp. 599-602, 1961.
16. D. Clark, K. S. Jepson, and G. I. Lewis: J. Inst. Metals, vol. 91, pp. 197-202, 1962-63.
17. I. I. Kornilov, E. N. Pylaeva, M. A. Volkova, P. I. Kripyakevich, and V. Ya. Markiv: Dokl. Akad. Nauk SSSR, vol. 161, pp. 843-46, 1965.
18. F. A. Crossley: Trans. TMS-AIME, vol. 263, pp. 1174, 1966.
19. M. J. Blackburn, Trans. TMS-AIME, vol. 269, pp. 1200, 1967.

20. T. Sugimoto, S. Komatsu, and K. Kamei: Titanium 80 Science and Technology, Proc. of the Fourth Int. Conf. on Titanium; H. Kimura, O. Izumi, Eds., vol. 4, pp. 2949, 1980.
21. T. K. G. Namboodhiri, C. J. McMahon, Jr., and H. Herman: Met. Trans., vol. 4 (May), pp. 1323, 1973.
22. Y. L. Yao: Trans. Am. Soc. Metals, vol. 54, pp. 241, 1961.
23. E. E. Kornelov, E. N. Pilayeva, and M. A. Volkora: Academy of Science, USSR, vol. 10, pp. 74, 1963.
24. R. D. Shull, A. J. McAlister, and R. C. Reno: National Bureau of Standards, unpublished work.
25. M. J. Marcinkowski: Electron Microscopy and Strength of Crystals, G. Thomas and J. Washburn, Eds., pp. 333, Interscience, New York, 1963.
26. M. J. Kaufman, D. G. Konitzer, R. D. Shull, and H. L. Fraser: Scripta Metallurgica, vol. 20, pp. 103-108, 1986.
27. D. G. Konitzer, I. P. Jones, and H. L. Fraser: Scripta Metallurgica, vol. 20, pp. 265-268, 1986.
28. T. K. G. Namboodhiri: Materials Science and Engineering, vol. 57, 21-22, 1983.
29. C. C. Chen and R. B. Sparks: Titanium '80, Science and Technology, Edited by H. Kimura, O. Izumi, vol. 4, pp. 2929, 1980.
30. R. D. Shull et. al., Proc. of Ti-6211 Basic Research Program, Office of Research, Eds. B. A. MacDonald, O. P. Aurora, B. B. Rath; pp. 1.
31. E. C. Bain : Chem. Met. Eng., vol. 28, pp. 21, 65, 1923.
32. C. H. Johansson and J. O. Linde: Ann. Physik. vol.78, pp. 439, 1925.
33. G. Tammann: Z. Anorg. Chem., vol. 107, pp. 1, 1919.
34. F. W. Jones and C. Sykes: Proc. Roy. Soc. (London), vol. A161, pp. 440, 1937.
35. J. W. Christian: "The Theory of Transformation of Metals and Alloys", Part 1, 2nd Eds., Pergamon Press, 1975.
36. N. Brown: Phil. Mag., vol. 4, pp. 693, 1959.
37. P. A. Flinn: Trans. AIME, vol. 218, pp. 145, 1960.
38. J. W. Cahn and R. Kikuchi: J. Chem. Phys. Solids, vol. 20, pp. 94, 1961.
39. A. J. C. Wilson: "X-Ray Optics; the Diffraction of X-rays from Finite and Imperfect Crystals", Methuen, London, 1960.
40. J. S. Koehler and F. Seitz: J. Appl. Mech., A 217, pp. 14, 1947.

41. M. Yodogawa, et al.: *Scripta Metallurgica*, vol. 14, pp. 849-854, 1980.
42. A. Inoue, H. Tomioku and T. Masumoto: *Met. Trans. A.*, vol. 14 a, pp. 1367, 1983.
43. S. M. L. Sastry, and H. A. Lipsit: *Met. Trans. A.*, vol. 8A, pp. 1543-1552, 1977.
44. H. Lipsitt: *Aviation Week*, vol. 81 (Jan), pp. 26, 1976.
45. C. T. Liu: *Met. Trans.*, vol. 4, pp. 1743, 1973.
46. C. T. Liu: *J. Nucl. Mat.*, vol. 85-86, pp. 907, 1979.
47. K. Aoki and O. Izumi: *Nippon Kinzoku Gakkaishi*, vol. 43, pp. 1190, 1979.
48. C. T. Liu, C. L. White, C. C. Koch, and E. H. Lee: Preparation of Ductile Nickel Aluminides for High Temperature Use, in *Proc. of the Conf. on high Temp. Materials Chemistry*, Princeton, New Jersey: Electrochemical Society, (1984).
49. A. I. Taub, S. C. Huang: *Met. Trans. A.*, vol. 15A, pp. 399, 1984.
50. A. Lawley: In *Intermetallic Compounds*, Eds. by J. H. Westbrook, New York: (John Wiley and Sons, New York, 1967), pp. 464-490.
51. N. S. Stoloff and R. G. Davies: *The Mechanical Properties of Ordered Alloys*, *Prog. in Mat. Science*, vol. 13, 1966.
52. N. S. Stolof: In *Strengthening Methods in Crystals*, Eds. A. Kelley and R. B. Nicholson, (Elsevier, New York, 1971), pp. 193-259.
53. M. J. Marcinkowski: In *Treatise on Materials Science and Technology*, Eds. H. Herman, (Academic Press, New York; 1974), pp
54. L. A. Nesbit and D. E. Laughlin: *Acta Met.*, vol. 29, pp. 989, 1980.
55. P. Morgand, P. Mouturat, and G. Sainfort: *Acta Met.*, vol. 16, pp. 867, 1968.
56. L. Nowac: *Z. Metallk.*, vol. 22, pp. 94, 1930.
57. O. Dahl: *Z. Metallk.*, vol. 24, pp. 107, 1932.
58. O. Dahl: *Z. Metallk.*, vol. 28, pp. 133, 1936.
59. W. Koster: *Z. Metallk.*, vol. 32, pp. 277, 1940.
60. D. Harker: *Trans. A. S. M.*, vol. 32, pp. 210, 1944.
61. G. W. Ardley: *Acta Met.*, vol. 3 (Nov.), pp. 525, 1955.
62. R. E. Schafrik: *Met. Trans.*, vol. 8A, pp. 1003, 1980.
63. M. J. Blackburn, and H. A. Lipsit: *Met. Trans.*, vol. 5, pp. 1373, 1974.

64. H. A. Lipsitt, D. Shectmen, and R. E. Schafrik: *Met. Trans.*, vol. 6A, pp. 1991, 1975.
65. H. A. Lipsitt, D. Shectman, and R. E. Schafrik: *Met. Trans.*, vol. 11A, pp. 1369, 1980.
66. S. M. L. Sastry and H. A. Lipsitt: In *Proc. of the 4th Int. Conf. on Titanium, Japan*, pp. 1231, Nov. 1980.
67. W. J. S. Yang: *J. Mats. Sci. Letts.*, vol. 1, pp. 199, 1982.
68. S. M. L. Sastry and H. A. Lipsitt: *Met. Trans.*, vol. 8A, 1543, 1977.
69. P. L. Martin, H. A. Lipsitt, N. T. Nuhfer and J. C. Williams: In *Proc. of the 4th Int. Conf. on Titanium, Japan*, pp. 1245, Nov. 1980.
70. S. Sircar, MS Thesis, Michigan State University, 1983.
71. K. Narasimhan, MS Thesis, Michigan State University, 1984.
72. Y. Y. Li, *Phys. Rev.* 76, 972 (1949); 77, 300 (1950).
73. C. N. Yang and Y. Y. Li, *Chinese J. Phys.* 7, 59 (1947).
74. Y. Y. Li, *J. Chem. Phys.* 17, 1335 (1949).